OPERA

Geochemical interactions and groundwater transport in the Rupel Clay. A generic model analysis.

OPERA-PU-TNO522

Radioactive substances and ionizing radiation are used in medicine, industry, agriculture, research, education and electricity production. This generates radioactive waste. In the Netherlands, this waste is collected, treated and stored by COVRA (Centrale Organisatie Voor Radioactief Afval). After interim storage for a period of at least 100 years, radioactive waste is intended for disposal. There is a world-wide scientific and technical consensus that geological disposal represents the safest long-term option for radioactive waste.

Geological disposal is emplacement of radioactive waste in deep underground formations. The goal of geological disposal is long-term isolation of radioactive waste from our living environment in order to avoid exposure of future generations to ionising radiation from the waste. OPERA (OnderzoeksProgramma Eindberging Radioactief Afval) is the Dutch research programme on geological disposal of radioactive waste.

Within OPERA, researchers of different organisations in different areas of expertise will cooperate on the initial, conditional Safety Cases for the host rocks Rupel Clay and Zechstein rock salt. As the radioactive waste disposal process in the Netherlands is at an early, conceptual phase and the previous research programme has ended more than a decade ago, in OPERA a first preliminary or initial safety case will be developed to structure the research necessary for the eventual development of a repository in the Netherlands. The safety case is conditional since only the long-term safety of a generic repository will be assessed. OPERA is financed by the Dutch Ministry of Economic Affairs and the public limited liability company Electriciteits-Produktiemaatschappij Zuid-Nederland (EPZ) and coordinated by COVRA. Further details on OPERA and its outcomes can be accessed at www.covra.nl.

OPERA-PU-TNO522
Title: Geochemical interactions and groundwater transport in the Rupel Clay. A generic model analysis
Authors: J. Griffioen (TNO), M. Koenen (TNO), H. Meeussen (NRG), P. Cornelissen (UU), L. Peters (TNO), S. Jansen (Deltares).
Date of publication: July 2017
Keywords: geochemistry, groundwater, clay, long-term evolution, disposal, radioactive waste

Contents

Summary

The Rupel Clay is assigned for potential future geological disposal of radioactive waste in the Netherlands. The suitability of this geological layer for disposal is influenced by the long-term behaviour of the Rupel Clay. In this study, this geochemical development was estimated on the basis of current knowledge of the properties of the Rupel Clay, literature data of processes affecting the clay over long, geological time scales, and geochemical and hydrogeological model calculations. On the basis of literature, no large geochemical changes of the Rupel Clay are expected at a time scale of 1 million years without natural or man-induced perturbations. Potentially relevant factors that were assessed are: clay weathering, organic matter degradation, microbially mediated conversions, cation-exchange and related clay swelling.

A major factor potentially causing changes of the Rupel Clay is formed by glacial events, and most specifically postglacial erosion. This might lead to exposure to oxygenated surface water, which induces geochemical reactions. Other, man-induced perturbations are establishment of mine galleries that induces inner oxidation of the clay and interaction between the engineered barrier system (EBS) and the clay across their interface. Geochemical modelling indicates that the reaction zones are small with a few dm and the reaction products may be transported several meters to tens of meters away from this zone depending on the diffusive and advective controls. This holds for the situation that the pore matrix remains water-saturated and flow of air does not play a role. Pyrite oxidation, cation exchange upon freshening/salinization and carbonate precipitation/dissolution exert the major controls.

The importance of advection and chemical osmosis as transport mechanisms in addition to diffusion was also considered. Few data exists about hydraulic heads under the Rupel Clay and this data indicates that head differences up to 10 m are present across the Rupel Clay in the southern Netherlands. Advective flow may thus be present, which size depends on the hydraulic conductivity of the clay layer. No field data exists on hydraulic conductivities of the Rupel Clay for the Netherlands, but advective flow rates up to about 1 mm/y seem realistic. Hydrogeological modelling shows that faults may have a limited impact as short circuit routes through juxtaposed fault blocks of the Rupel Clay: the enlargement in flow rate rapidly declines away from a fault. A newly developed model that includes chemical osmosis shows that this process may have a similar magnitude at the geological time scale as diffusion and advection for appropriate conditions. Such appropriate conditions are present as soon as a large contrast in salinity exists across the Rupel Clay.

Samenvatting

De Rupel Klei is een potentiële geologische eenheid voor de eindberging van radioactief afval in Nederland. De geschiktheid van deze geologische laag voor berging van dit afval wordt beïnvloed door het gedrag van de Rupel Klei op lange termijn. In deze studie is deze geochemische ontwikkeling ingeschat op basis van de huidige kennis over de eigenschappen van de Rupel Klei, literatuurgegevens van processen die de klei over lange termijn zouden kunnen beïnvloeden, en geochemische en hydrogeologische modelberekeningen. Op basis van de literatuur worden er geen grote geochemische veranderingen van de Rupel Klei verwacht op een tijdschaal van 1 miljoen jaar zonder natuurlijke of door de mens veroorzaakte verstoringen. Mogelijk relevante factoren die werden beoordeeld zijn: kleiverwering, afbraak van organisch materiaal, omzettingen door micro-organismen, kation-uitwisseling en kleizwelling.

De belangrijkste factor die zou kunnen leiden tot veranderingen van de Rupel Klei is de invloed van ijstijden, en meer specifiek postglaciale erosie. Dit zou kunnen leiden tot blootstelling aan zuurstofrijk oppervlaktewater, wat geochemische reacties oproept. De constructie van mijngallerijen en het contact van de klei met het afval in een engineered barrier systeem roept ook geochemische reacties op. Geochemische modelberekeningen geven hiervoor aan dat de reactiezones klein zijn met enkele dm en dat de reactieproducten over enkele meters tot tientallen verder getransporteerd kunnen worden afhankelijk van het optreden van advectie naast diffusie. Dit geldt zo lang de kleilaag waterverzadigd blijft en er via scheuren en spleten geen luchtstroming optreedt. Pyrietoxidatie, kation-uitwisseling bij verzoeting/verzilting en kalkchemie spelen de hoofdrol.

Het belang van advectie en chemische osmose als grondwater transportprocessen naast diffusie was ook verkend. Er zijn maar enkele putten in zuid-Nederland met stijghoogtegegevens van putten onder de Rupel Klei. Deze gegevens geven aan dat een stijghoogteverschil tot ongeveer 10 m bestaat. Advectieve stroming kan dus plaats vinden afhankelijk van de feitelijke doorlatendheid. Er zijn geen metingen van de doorlatendheid van de Rupel Klei in Nederland maar advectiesnelheden van ongeveer 1 mm/j lijken realistisch. Hydrogeologische modellering gaf ook aan dat het ruimtelijke effect van breuken als kortsluitstroming beperkt is: de extra advectie die kan optreden bij verplaatste doch overlappende kleilagen van ca. 100 m dik beperkt zich tot de eerste paar honderd meter vanaf de breuk. Een nieuw ontwikkeld model met chemische osmose geeft aan dat dit transportproces op de geologische tijdschaal van een vergelijkbare orde grootte kan zijn als diffusie en advectie bij de juiste randvoorwaarden. Deze randvoorwaarden bestaan uit een groot contrast in zoutgehalte onder en boven de Rupel Klei.

1. Introduction

1.1. Background

Clays are potential host rock for geological disposal of radioactive waste. Their low permeability and strong sorption capacity make them very suitable as a layer to prevent migration from radionuclides potentially escaping from the repository. The Rupel Clay in the Netherlands is assigned as a potential formation for future geological disposal of radioactive waste. Within the research program OPERA the feasibility and long-term safety of a repository in this formation is investigated.

An assessment of the geochemical integrity and evolution of the Rupel Clay is element for the Safety Case. An important aspect in this long-term safety assessment is the autonomous evolution of the Rupel Clay at geological time scale. Insight into the geochemical behaviour of the Rupel Clay is further needed to evaluate its short- and long-term integrity in case of the presence of a radioactive waste disposal. Besides radioactive waste and its matrix and packaging, such a repository consists of elements of engineered barrier system (EBS), made from cement and steel. Heat generation, gas generation and transport of (bio)geochemical reaction products could alter the geochemical properties of the Rupel Clay and thereby potentially induce mineral dissolution and precipitation reactions. One well known effect is the appearance of an alkaline plume as a result of cement degradation. Although limited in its extent, the effects of such reaction products need to be assessed.

1.2. Objectives

The central objective of this study is to determine what geochemical development of the Rupel Clay is expected over a prolonged time scale. The development of the Rupel Clay is considered for different scenarios:

- The long-term autonomous geochemical evolution of the Rupel Clay
- The geochemical evolution under the conditions of a gallery
- The geochemical evolution at the interface between an engineered barrier system (EBS) and the Rupel Clay
- The likelihood or not of reactive transport conditions in the Rupel Clay other than molecular diffusion, i.e., chemical osmosis or advective flow.

As input for this, the current geological and geochemical characteristics as well as hydrogeological conditions are used as input. Using these starting points, extensive attention is paid to both the conceptual geochemical modelling as well as quantitative geochemical and geohydrological prognosis modelling. The modelling approach as a whole is generic by nature and not site-specific.

The focus will be on the major geochemistry of the Rupel Clay and those corrosion/degradation products that affect the major geochemistry. Furthermore, the potential consequences of these physical and chemical alterations on the short term (<100 years) retrievability as well as the long term safety function '**transport and retention**' will be evaluated. With respect to the long term safety function '**transport and retention**', the impact of geochemical changes on major chemistry as boundary condition for transport of radionuclides and the variability of parameter values will be evaluated.

1.3.Realization

The research is partly performed in task 5.2.1 under the activity entitled "*Geochemical properties and long-term evolution of Rupel Clay*" and majorly in task 5.2.2 in which the activities are centred around the following two research questions:

1. What is the impact of the geochemical processes on the **retrievability of the waste** on the ''short term'' (about 100 years)
2. What is the impact of the geochemical processes on the **transport and retention safety function** of the Rupel Clay on the ''long term''.

The information from WP 5.1 (*Geochemical behaviour of EBS*) on total fluxes of alkalinity, salt, and oxidizing substances can be used as input in these two tasks under WP 5.2 to estimate the extent of the clay zone that will be affected by the EBS degradation products.

This research also builds upon results from WP 4.1 (*Geology and geohydrological behaviour of the geosphere*) as well as results from task 5.2.1 on the geochemical characterisation of the Rupel Clay and its surrounding groundwater. Results on the large-scale far-field geohydrological modelling (WP 6.2 *Radionuclide migration in the rock formation surrounding the host rock*) played a role as input and inspiration for the geohydrological activities performed in the present task, too. The results under WP 5.2 are useful as input in tasks under WP 6 and WP 7, which will investigate reactive transport of radionuclides.

The literature study and geochemical calculations on the evolution of the Rupel Clay were performed by TNO with support by Deltares. The geochemical calculations on the interactions between the host rock and EBS were performed by NRG. The geohydrological calculations on advective/diffusive transport at the fault block scale were performed by TNO and those on chemical osmosis on the clay layer scale by Utrecht University with support by TNO.

1.4.Explanation of contents

Chapter 2 presents an overview of the geochemical properties of the Rupel Clay. Long-term, future scenarios and autonomous developments expected for the Rupel Clay in the Netherlands are briefly depicted in chapter 3. In chapter 4, a literature study on potential autonomous developments in the Rupel Clay on the basis of these scenarios is described. Chapter 5 presents modelling results on the pore water composition within the Rupel Clay as it presumably occurs in large parts of the Netherlands. A modelling assessment of the geochemical development of the Rupel Clay impacted by postglacial erosion or following construction of mine galleries is presented in Chapter 6. The geochemical evolution at the interface between the Rupel Clay and the Engineered Barrier System is presented in Chapter 7. Chapter 8 discusses the potential role of advective flow and fault blocks on transport in the Rupel Clay and so does Chapter 9 for chemical osmosis. Finally, the relevance of all these outcomes for the safety case is discussed in Chapter 10.

2. Current geological and geochemical characteristics of the Dutch Rupel Clay

The Rupel Clay has been selected as a potential medium for disposal of radioactive waste. This clay layer is present in the subsurface of nearly the complete onshore part of the Netherlands. Furthermore, it is present in the shallow subsurface of Belgium where it crops out along the southern fringes of Flanders. In Belgium extensive research on the Boom Clay has been performed and an underground test facility is present in this layer near the town of Mol (Van de Vate, 2012). According to the present Dutch geological stratigraphy, the Rupel Clay is referred to as the Rupel Clay Member, being part of the Oligocene Rupel Formation. The Rupel Clay Member is more or less equivalent to the Boom Clay Formation in Belgium (Vis et al., 2016). We will follow the national conventions as closely as possible when referring to this geological entity.

The Rupel Clay is a marine clay, deposited between 33.9 and 28.1 million years ago. The thickness varies around a mean of 65 m. The Rupel Clay Member is not a homogeneous clay; both vertical and lateral grain-size trends are present. The calculated porosity and permeability of the clay are lowest in the Roer Valley Graben where the layer is buried deepest. Faults are known to cut through the clay layer, but their hydrological consequence is still poorly understood. In spite of the large amount of geoinformation available for the Netherlands, several issues are not known because attention was focused to either the more shallow Quaternary sediments or the deeper Cretaceous and older sediments which may contain natural gas and oil. Unknown issues refer in particular to the geohydrological properties of the Paleogene Formations such as permeability, fault locations and groundwater fluxes in the clay (cf. Vis & Verweij, 2014).

2.1. Sediment mineralogy and geochemistry

The mineralogy and geochemistry of the Dutch Rupel Clay and their geographical and depth-related heterogeneity were studied and reported within OPERA task 5-2-1 (Koenen and Griffioen, 2014). The mineralogy from whole rock and clay fraction XRD analyses was determined for 30 samples from 7 different boreholes spread across the Netherlands and is shown in Table 2.1. The bulk of the mineralogy is the same for all samples: quartz, feldspar, 2:1 clay minerals and kaolinite. Most samples contain calcite and/or aragonite with varying concentrations, gypsum and minor chlorite, pyrite and anatase. Few samples contain some clinoptilolite/heulandite, dolomite, siderite, ilmenite, sylvite, halite and jarosite. The latter three minerals (and most probably gypsum) are considered artefacts due to drilling and/or storage under oxidizing conditions. Hence, they are not taken into account in this task.

Geographically, three statistically different groups are recognized. The Rupel Clay in the southern part of the Netherlands has coarser, silty upper and lower parts. The central part is finer grained and more clay-rich with occasional silt layers. This is consistent with the cyclic alternation of clay- and silt-rich layers found in the Belgian Rupel Clay. In the southeast of the Netherlands, the Rupel Clay has a higher carbonate content than in the southwest. The Rupel Clay in the north of the Netherlands is significantly different from that in the southeast and southwest. The Rupel Clay is fine grained and clay- and carbonate-rich across the entire depth interval. Both the pyrite and organic carbon contents are important parameters due to their reactivity and potential impact on the safety function ‘delay and attenuation of releases’. The pyrite and organic carbon contents vary among the samples but they do not show geographic or depth-related variations (Koenen & Griffioen, 2014).

Table 2.1. XRD mineralogy in minimum, average and maximum wt% for the total of 30 samples and for the 8 samples in the northern Netherlands only.

	Total			North NL only		
	MIN	AVERAGE	MAX	MIN	AVERAGE	MAX
Whole rock XRD						
Quartz	16.3	41.5	86.3	16.3	25.3	71.7
Albite	0.0	2.4	5.6	1.0	2.0	4.8
K-feldspar	2.2	6.6	11.1	3.0	4.8	10.1
Clinoptilolite/Heulandite	0.0	0.5	2.9	0.0	0.5	2.1
Calcite	0.0	3.7	25.9	0.0	6.6	25.9
Aragonite	0.0	1.0	5.1	0.0	0.0	1.4
Total $CaCO_3$[#]	0.0	4.8	25.9	0.0	6.6	25.9
Ankerite/Dolomite	0.0	0.1	1.5	0.0	0.1	0.5
Siderite	0.0	0.2	3.9	0.0	0.0	0.0
Pyrite	0.0	0.8	6.9	0.0	0.5	1.1
Anatase	0.0	0.4	0.9	0.4	0.6	0.9
Ilmenite	0.0	0.0	0.4	0.0	0.0	0.4
Sylvite	0.0	0.2	2.2	0.0	0.7	2.2
Halite	0.0	0.2	1.4	0.0	0.6	1.4
Gypsum	0.0	0.8	2.4	0.0	0.6	2.4
Jarosite	0.0	0.4	2.8	0.0	0.4	2.8
Chlorite	0.0	1.1	3.7	0.0	1.7	3.1
2:1 clay	7.2	35.9	63.1	33.9	49.6	63.1
Kaolinite	0.8	4.0	12.1	2.4	6.0	12.1
Clay fraction XRD						
Kaolinite	2.0	6.1	12.0	3.0	5.3	11.0
Kaolinite-smectite*	2.0	7.2	14.0	2.0	8.3	14.0
Chlorite	1.0	1.3	2.0	1.0	1.1	2.0
Smectite	3.0	37.9	60.0	36.0	47.5	60.0
Illite-smectite*	6.0	24.6	45.0	9.0	18.9	37.0
Illite	5.0	13.2	26.0	7.0	10.9	16.0
Glauconite-smectite*	0.0	9.7	79.0	0.0	8.3	25.0

[#] Total $CaCO_3$ represents the sum of calcite and aragonite
*** Interstratified clay minerals**

The average mineral content was adapted with the following considerations taken into account. Clinoptilolite/heulandite was only found in the freshly taken samples and in two samples from a core in the north of the Netherlands. Concentrations are up to 3 wt%. The mineral clinoptilolite ($(Na,K,Ca)_{4-6}Al_6Si_{30}O_{72}\cdot 24H_2O$) forms a solid solution series with heulandite ($(Na,Ca)_{4-6}Al_6Si_{30}O_{72}\cdot 24H_2O$). They are both naturally occurring zeolites which generally form from weathering of volcanic rocks. Therefore, they are assumed to be detrital minerals in the Rupel Clay. The sodium and calcium in both zeolites, and potassium in clinoptilolite, are loosely held and can be exchanged for other cations. These minerals contribute to the cation exchange capacity and are thus important for the diffusion of radionuclides through the Rupel Clay.

Figure **2.1** (left graph) shows that samples contain either clinoptilolite/heulandite or gypsum. Since clinoptilolite/heulandite was particularly found in the freshly taken samples, this observation supports the hypothesis that gypsum is an artefact of oxidizing storage conditions. It is currently unclear why the two samples from the stored core from the North of the Netherlands do not show signs of oxidation even though this core was also stored under oxidizing conditions. We assume that gypsum is not present in undisturbed Rupel Clay although its presence cannot be completely excluded. In the Rupel Clay in Belgium, gypsum is not present in undisturbed core material (De Craen et al., 2011).

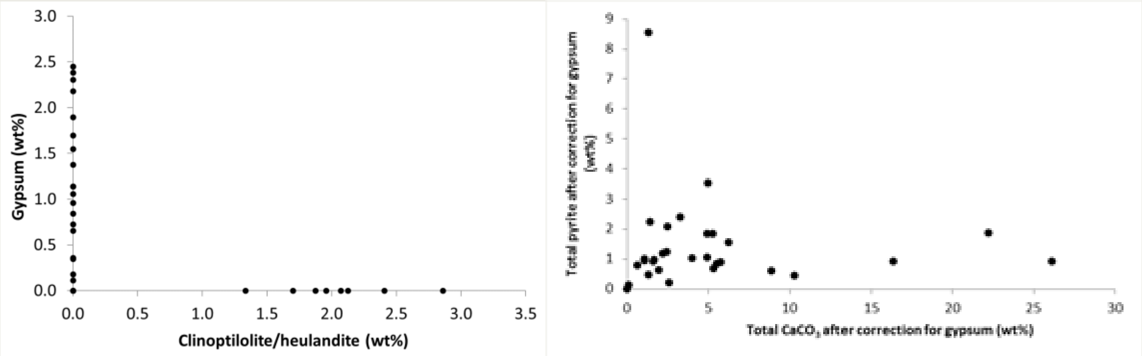

Figure 2.1. Results from whole rock XRD analyses (Koenen and Griffioen, 2014). Left: Clinoptilolite/heulandite versus gypsum. Right: Pyrite versus total $CaCO_3$ content.

The carbonate content of the Rupel Clay is an important parameter because it determines the pH buffering capacity upon proton production. In the context of pyrite oxidation and subsequent acidification (see next section), a high carbonate content can be advantageous for pH buffering. Since both dolomite and siderite are rarely present, only calcite and aragonite will be taken into consideration. The total $CaCO_3$ (calcite + aragonite) from XRD analysis was corrected for the presence of gypsum, assuming that the calcium in gypsum originated from $CaCO_3$. The total $CaCO_3$ concentration based on these calculated values are between 0 and 26 wt%. The pyrite content was also corrected for the presence of gypsum assuming that the sulphur originated from pyrite. Figure 2.1 (right graph) shows that the pyrite and total $CaCO_3$ contents are generally below 2 and 6 wt%, respectively. Higher values of pyrite up to 8.5 wt% occur at low total $CaCO_3$ content, and higher values of total $CaCO_3$ up to 25.9 wt% occur at low pyrite content.

Since XRD analysis was only performed on 30 out of 152 Rupel Clay samples, the CaO and Al_2O_3 contents from XRF analysis, reported in Koenen and Griffioen (2014), were used to calculate the total $CaCO_3$ content using the equation defined by Griffioen et al. (2012):

$$\text{Carb (wt\%)} = M_{CaCO3}/M_{CaO}*[CaO-(0.0448*Al_2O_3-0.1147)]$$

The results for the comparison between the measured and calculated $CaCO_3$ content is shown in Figure 2.2. Measured and calculated contents correlate well ($R^2 = 0.93$), implying that in the absence of XRD analyses the calcium and aluminium contents can be used to estimate the total carbonate content. The average calculated carbonate content from a total of 152 samples is 4.2 wt%, compared to an average value of 5.2 wt% as measured by XRD (and corrected for gypsum) on 30 samples.

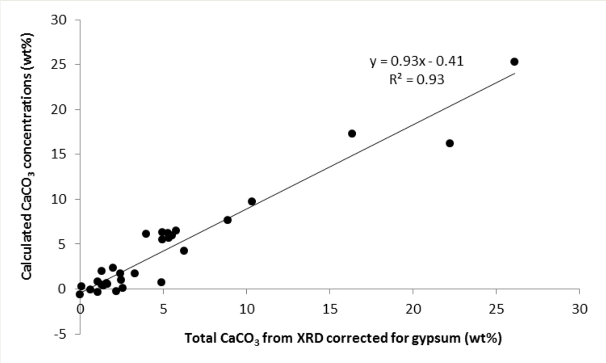

Figure 2.2. Total $CaCO_3$ from XRD analysis corrected for gypsum versus calculated concentrations from XRF analysis (Koenen and Griffioen, 2014).

The clay mineralogy analysed by clay fraction XRD analysis consists mainly of kaolinite, smectite, illite and interstratified clays for all samples analyzed (Table 2.1). In the databases used for geochemical modelling interstratified clays are not included. The clay minerals kaolinite, smectite and illite were considered in this study where the interstratified clays were attributed to one of their end-members.

2.2.Hydrochemistry

In Belgium, the influence of meteoric waters causes very low NaCl concentrations in the Boom Clay. The values for Cl measured for the Boom Clay in Mol and the Essen-1 borehole (respectively NNE- and N-Belgium) are 26 mg/l and 106-3100 mg/l, respectively. In the Essen-1 borehole, the Cl concentration clearly increases with depth (De Craen et al., 2006). In Zeeland, the Netherlands, the measured pore water NaCl concentrations are high (~8,000-20,000 mg/l) regardless of the shallow depth (Behrends et al., 2015). According to the authors, this is the result of a salinity front into the Rupel Clay. It is currently unclear whether this is a local phenomenon or a widely spread feature of the Rupel Clay in the Netherlands. Groundwater underneath the Rupel Clay in Zeeland varies in Cl concentration between 87 and 2600 mg/l (Griffioen et al., 2016). In the north of the Netherlands, accurate measurements on Rupel Clay formation water have not yet not been performed.

Griffioen (2015) reported on deep groundwater compositions above and below the Rupel Clay in the Netherlands. In the north, the groundwater above the Rupel Clay is highly variable, with Cl values between 10 and 10,000 mg/l at depths between 100 and 260 m below surface. No depth relation can be observed. The p25 and p75 values are 24.8 and 238 mg/l, respectively. In western Brabant, Cl concentrations are mostly low, but groundwater becomes brackish to saline with increasing depth. Cl concentrations are lowest in Middle Limburg. Below the Rupel Clay, the Cl content is about 73,000 mg/l at Nieuweschans, where the well is located not far away from a shallowly present salt diapir whereas the values range from 9,000 to 31,000 mg/l for a small number of measurements in North Brabant and Limburg (Griffioen et al., 2016). The highest concentrations are probably due to the presence of Zechstein salt and salt diapirs (Verweij, 2003; Griffioen et al., 2016). Based on these results, the Cl concentration in the Rupel Clay can be anywhere between 10 and 100,000 mg/l where the highest concentrations are expected in the north and the lowest in Brabant. It is probably saline for the largest part of the Netherlands as saline groundwater is frequently encountered both below and closely above the Rupel Clay.

3. Future scenarios

Various future scenarios have been worked out and described. Here, we mainly focus on the scenarios formulated for the storage case in Belgium in the ONDRAF/NIRAS program (ONDRAF/NIRAS, 2001) and as formulated in the COVRA program (Grupa et al., 2017). Two groups of scenarios are distinguished: the normal scenario, and the altered evolution scenarios.

3.1.Normal scenario

The normal scenario consists of the following steps (Fig. 3.1; Grupa et al., 2017):

1. Emplacement of the waste packages in the disposal gallery. The lining and plugs are intact, the inside of the gallery is initially dry. After some decades, the gallery internals become saturated with water. For Intermediary Level Waste (ILW) and Low Level Waste (LLW) there is no engineered containment and leaching may start soon after closure; for High Level Waste (HLW) the canister and overpack will fail after some thousands of years.
2. After some thousands of years, significant migration into the host rock can occur. For mobile nuclides this means several tens of meters; for immobile nuclides not more than 1 meter.
3. After a few tens of thousands of years, mobile nuclides may reach the adjacent aquifer system.
4. After longer time scales, further migration to the biosphere can occur. Due to radioactive decay, delay and dilution only a small fraction reaches the biosphere.

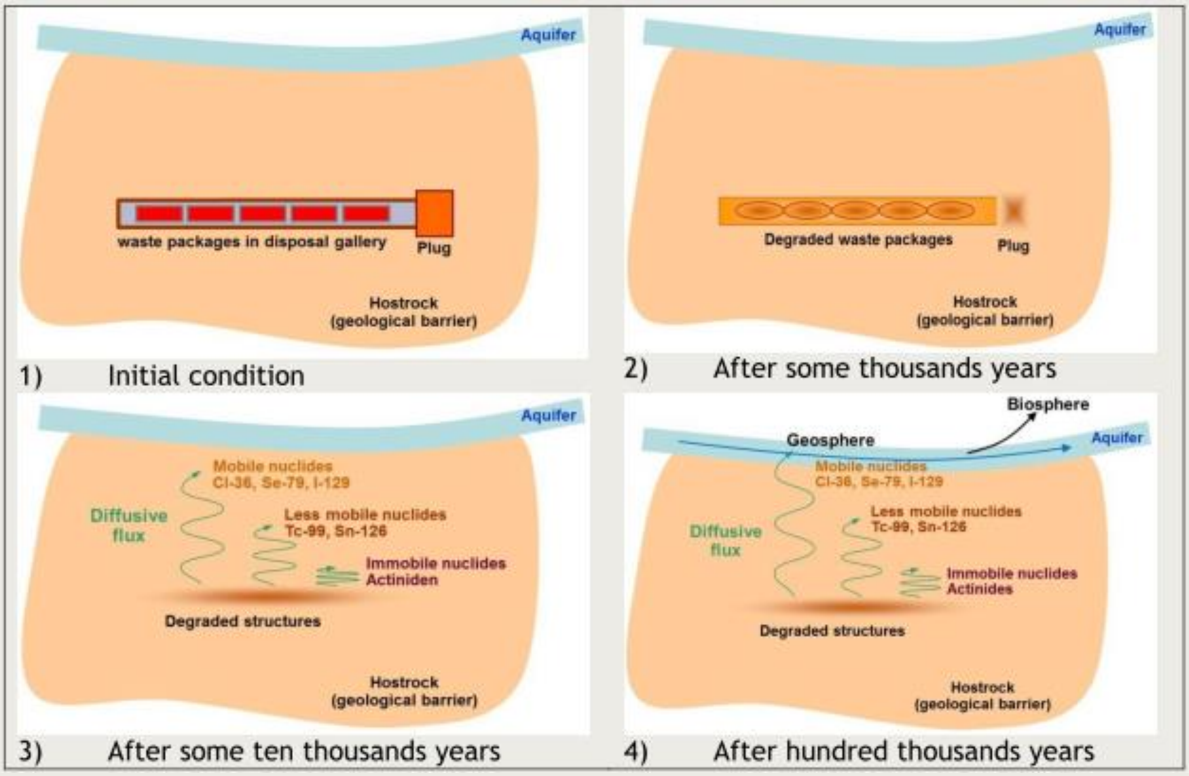

Fig. 3.1. Schematic illustration of the normal evolution scenario (from Grupa et al., 2017).

Within the far field, the following factors affect radionuclide migration. The clay host rock delays release of the radionuclides. Retardation takes place by sorption onto clay or organic matter or other geochemical processes. Hydraulic conductivity of the clays is very small, thus limiting transport: transport occurs mainly by diffusion. Climate change can be considered as a normal future scenario because of the cyclic nature of ice ages in the Quaternary geological period. Glacial events are expected to have a significant effect in the far field, which will be discussed in more detail later in this text.

3.2. Altered evolution scenarios

The following altered evolution scenarios were considered by Grupa et al. (2017):

- Abandonment Scenario
- Poor Sealing Scenario
- Anthropogenic greenhouse scenario
- Fault Scenario
- Intensified glaciation scenario
- Human Intrusion and Human Action Scenarios.

In the present study, only the intensified glaciation scenario will be discussed, because the other scenarios either have limited effect on geochemical parameters in the far field or mainly have effects on other aspects. Other natural processes that might be of influence include:

- Tectonics
- Subsidence
- Flooding
- Diagenesis.

These are either not predictable or of little influence for the Dutch settings and are thus left out of account in this study.

Climate evolution and intensified glaciation

Climate evolution is a process which is widely accepted to have an influence on the subsurface used for storage of radioactive waste (SAFIR-2, Gupta et al., 2017, Talbot, 1999). On the basis of historical climatic cycles, a moderate cooling is expected after 24,000 years, and more severe cooling can be expected after 56,000 years. In the scenarios described by the SAFIR-2 study (NIRAS-ONDRAF, 2001), two approaches were chosen:

1. the present hydrogeological system is a reference, and is applicable for the whole period considered;
2. the glacial period has effect.

The reference scenario for the Gorleben storage site (GRS, 2012) includes glacial periods effects over 1 million years. The effects of a glacial period are as follows:

- Changes in precipitation
- Lowering of temperature
- Formation of permafrost
- Expansion of ice sheet
- Subglacial erosion.

Wildenborg et al. (2003) described the importance of these factors for geomechanical parameters of the Rupel Clay. Further, Ten Veen et al. (2015) recently showed that permafrost in the Netherlands is not expected to reach the Rupel Clay when it lies several hunders meters below surface. The formation and removal of an ice sheet and subglacial erosion lead to pressure changes and thus to geomechanical effects. Especially postglacial erosion can have significant effects. On relatively small time scales, erosion down till 300 meter can take place resulting into so-called subglacial tunnel valleys (Fig. 3.2). These valleys are then filled up by relatively permeable material (Janszen, 2009; Beets & Beets, 2003). The erosion and subsequent filling up may happen at relatively small time scales (ca. 1000 years). These events will have high geomechanical impact: the underlying sediments will be exposed to highly variable pressures. Wildenborg et al. (2003) described the expected compaction and associated water movement, which was calculated to potentially amount to 1 mm/year during a disturbed situation.

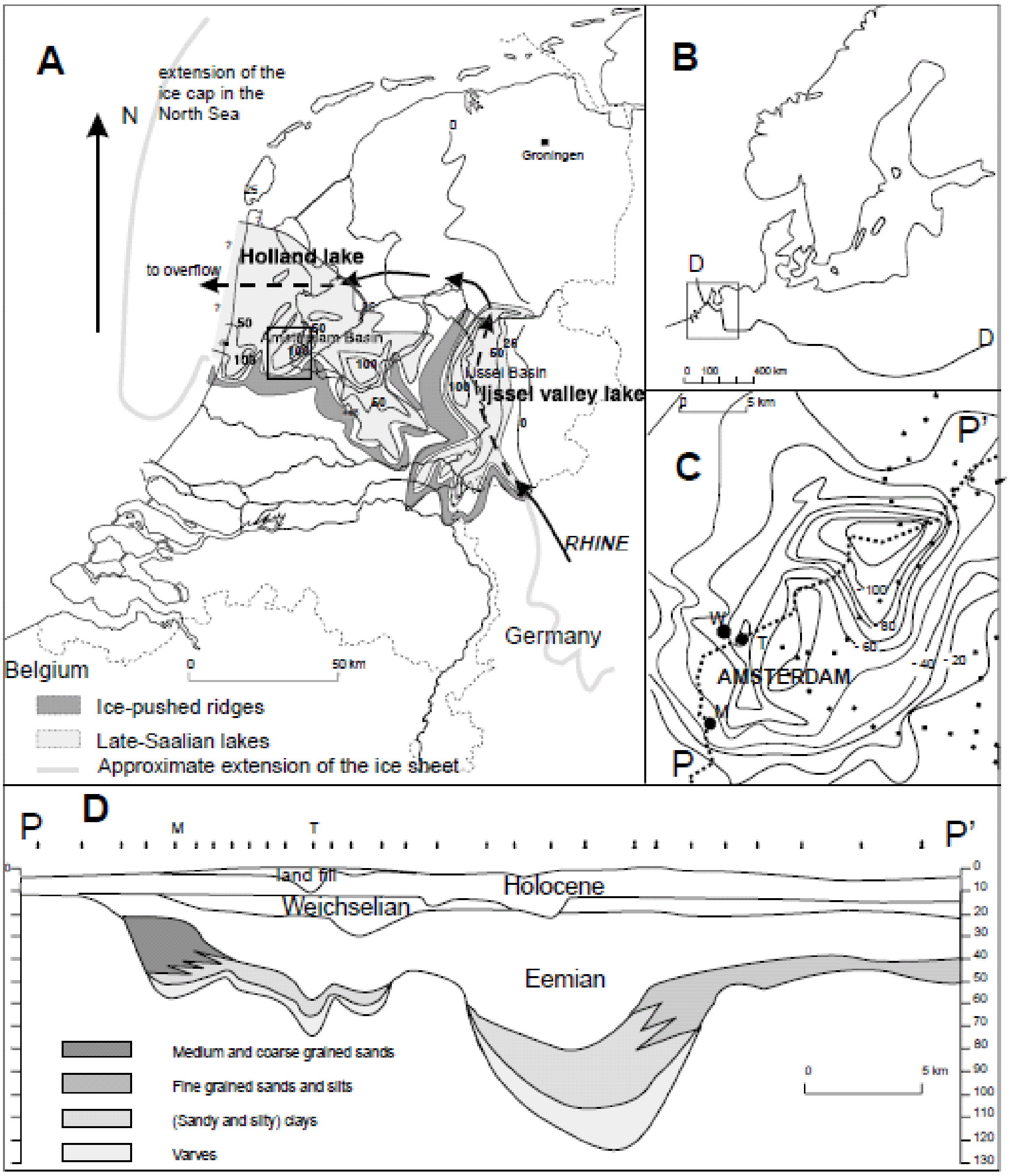

Fig. 1. (A) Map of the Netherlands with the position of the ice-pushed ridges on land, the approximate extension of the ice sheet in the North Sea and Germany, the glacially excavated basins, the lakes formed after melting of the ice sheet, and the course of the river Rhine. (B) The position of the Netherlands at the margin of the Saalian ice sheet during the Drenthe substage. (C) Depth contours of the glacial basin of Amsterdam (after De Gans et al., 2000); stippled line P–P′ gives the location of the cross-section of (D) and the position of the studied cores: T = core Terminal, W = core Willemshuizen, M = core De Mirandabad. For the position of C see the inset in A. 1D. Cross-section of the basin of Amsterdam with the main lithologic units of the Late Saalian fill of the basin; T and M are the positions of the cores Terminal and De Mirandabad; the position of the other cores used for the construction of the cross-section are indicated with a small signature (after De Gans et al., 2000); the "land fill" consists of material dumped below the city of Amsterdam.

Fig. 3.2. Example of geological effects of postglacial erosion (Beets & Beets, 2003).

Next to the compaction, fractures are probably the most intense perturbation. The extent to which fractures will occur depends on the plasticity of the clay. The in situ plasticity of Rupel Clay and heterogeneity, and thus the extent to which fractures are expected, is not exactly known.

Due to the removal of a thick layer of sediment during a postglacial erosion event, and the deposition of a younger, permeable layer, the chemical environment of the upper part of the remaining clay also changes. It may be exposed to an environment with more oxygen and, potentially, a different salinity, when the locality is sufficiently close to the surface water system present. In many respects, the effect of postglacial erosion is comparable with the effect of excavation: in both cases the sediment which was left to age in a relatively homogeneous environment for a long time becomes exposed to highly heterogeneous conditions over a relatively short timescale. This is expected to create strong gradients which can act as driving forces for geochemical reactions. The question is what the extent of these reactions is, and to which distance the effects will reach.

4. Geochemical processes in the Rupel Clay - literature

In the following sections we will briefly investigate literature studies on the following aspects that are potentially relevant in the long-term geochemical evolution of the Rupel Clay:

1. Release of EBS reaction products
2. Oxygen exposure
3. Degradation of sedimentary organic material;
4. Microbially mediated reactions;
5. Silicate weathering;
6. Cation-exchange
7. Clay swelling

We present general insight below with limited amounts of references as scientific support. We did not attempt to present complete overviews on these topics addressed.

4.1. Release of EBS reaction products

Perturbations will mainly occur in the near-field, where the near-field is described as that part of the repository that includes the waste packages, further engineered barriers and the zone disturbed by the presence of any excavations (Verhoef & Schröder, 2011). Four perturbations of importance that were studied, are: iron corrosion (from packings of radioactive waste), the alkaline plume from the cement casing, oxidation and generation of H_2 gas. We illustrate the knowledge on these effects with some examples from literature as they can help to understand effects of other perturbations in the far field.

The first example of this is a modelling study by Esnault et al. (2013) of the effects of microbial development associated with the corrosion process of iron in argillite (Fig. 4.1). The modelling estimated the effects to a maximum time scale of 1 million years. The modelling shows two aspects. Firstly, geochemical and microbial conversions are possible in the impermeable clay matrix. Secondly, these conversions are predicted to be limited to the first few meters of the clay. The reason for this is the slow transport process of diffusion.

The effect of the alkaline plume from the cement was studied by various researchers using geochemical models, for example by Gaucher & Blanc (2006), Jacques & Wang (2012) and Wang et al. (2008) (Fig. 4.2). It was shown that the geochemical effect is significant (pH increase, clay conversions), but the effect is limited to one or a few meters distance (Fig. 4.3).

The effect of advection at the clay rock-cement interface was investigated by Kosakowski et al. (2013) for several proposed clay host rocks in Switserland . These calculations show that the mineralogical changes at material interfaces are restricted to narrow zones for all host rocks. The extent of strong pH increase in the host rocks is limited, although a slight increase of pH over greater distances seems possible in advective transport scenarios. The calculations for diffusive and partially also the advective transport show massive porosity changes due to precipitation/dissolution of mineral phases near the interface, in line with other reported transport calculations on cement/clay interactions (Gaucher & Blanc, 2006; Jacques & Wang, 2012; Wang et al., 2008). For all investigated transport scenarios, the degradation of concrete materials in emplacement caverns due to diffusive and advective transport of clay pore water from the caverns is limited to narrow zones.

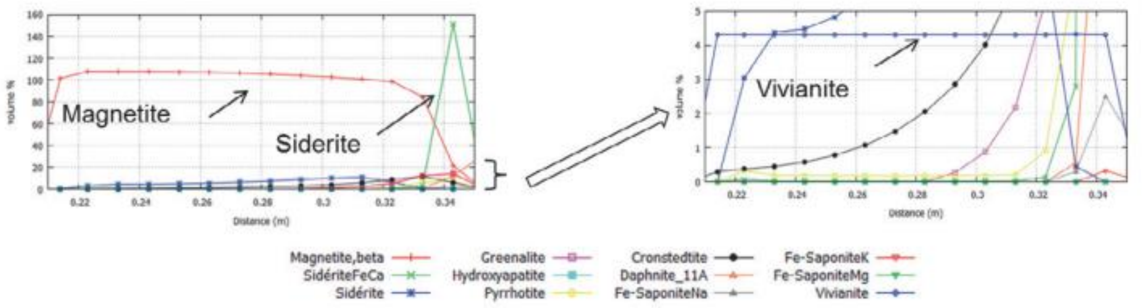

Fig. 1. Corrosion product volume percent at 30,000 years (end of corrosion) in the container zone.

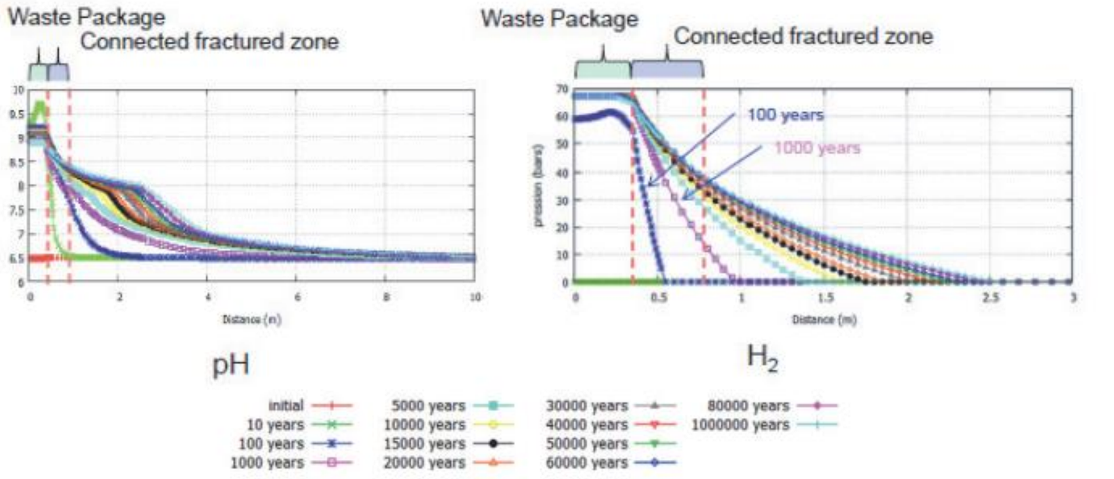

Fig. 2. Evolution of pH and H_2 in claystone during HLW packages corrosion process.

Figure 4.1. Extent of expected evolution of corrosion products, pH and H_2 due to corrosion of iron in argillite claystone as modelled by Esnault et al. (2013).

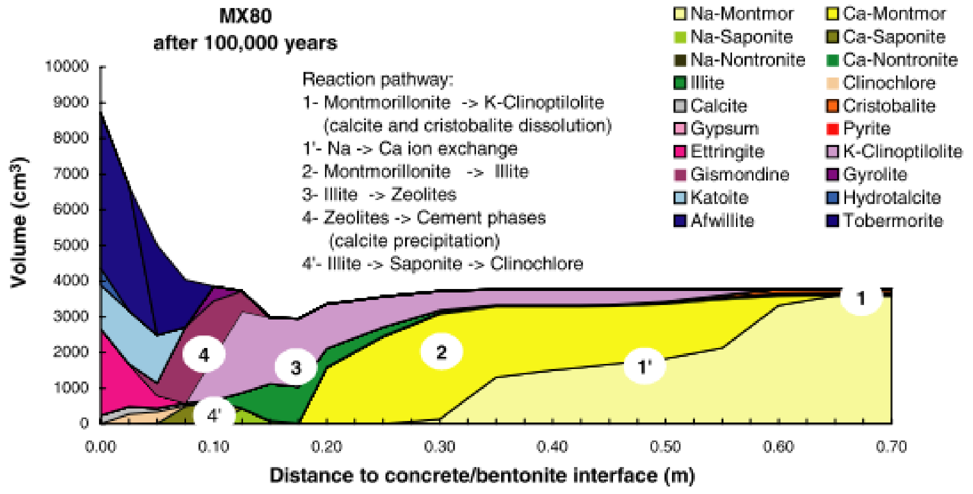

Fig. 2. Composition of a clay barrier after 100,000 years of interaction with an effective diffusion coefficient of 10^{-11} m^2/s.

Figure 4.2. Effects of the concrete/clay interface on geochemical conversion over a time course of 100,000 years, as modelled by Gaucher & Blanc (2006).

Figure 2: pH evolution near the concrete – Boom Clay boundary for the reference model (vertical line indicates the concrete – Boom Clay interface).

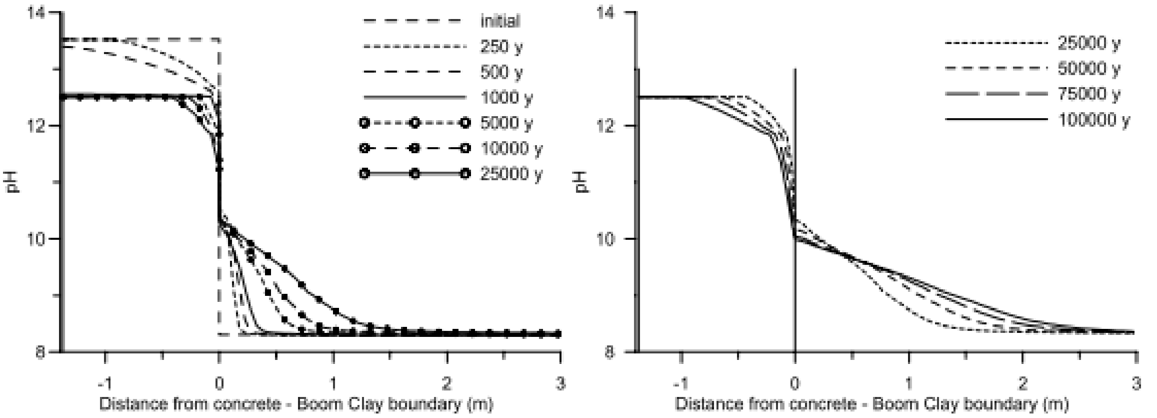

Figure 4.3. Effects of concrete on the pH in Rupel Clay as modelled by Jacques & Wang (2012).

Hydrogen may be produced during subsurface disposal due to anaerobic corrosion of steel and other metals, radiolysis of water and degradation of (natural or not) organic material (Norris, 2015). When it is produced in large quantities, the expansive gas pressure may disrupt the solid matrix causing cracks to develop (e.g. Jacops et al., 2015). This lies outside the scope of the present study. The produced hydrogen may serve as reductant in microbially mediated redox processes, which also diminishes the risk of disruption of the solid matrix (Bagnoud et al., 2016). Depending on the operational redox processes and its secondary processes, other gases as CH_4 and CO_2 may be produced. Redox reactions with natural Fe(III) and SO_4 (if present) are most probable after closure of the subsurface disposal site, when small, unreactive amounts of organic matter are present (Libert et al., 2014). The phenomenon of H_2 production has not been considered any further in this study.

4.2. Oxygen exposure

Oxidation by means of penetration of oxygen can potentially induce the following processes:

- Pyrite dissolution, accompanied with acidification;
- Calcite dissolution in response to acidification (neutralization);
- Exchange of calcium from calcite with sodium on the clay minerals.

The overall result of these 3 processes together is that dissolved Na and SO_4 increase in the pore water.

The main redox process expected to occur in the Rupel Clay as a consequence of oxidation is the oxidation of pyrite. This occurs according to the following equation:

$$FeS_2 + 3.5O_2 + H_2O \rightarrow Fe^{2+} + 2H^+ + 2SO_4^{2-} \qquad (1)$$

The mobilised Fe(II) can also be oxidized to Fe(III). The increased acidity from pyrite oxidation will induce pH buffering by carbonates such as calcite and dolomite when present:

$$CaCO_3 + H^+ \rightarrow HCO_3^- + Ca^{2+} \qquad (2)$$

$$CaMg(CO_3)_2 + 2H^+ \rightarrow 2HCO_3^- + Ca^{2+} + Mg^{2+} \qquad (3)$$

As a result, the concentration of SO_4 increases, the pH goes down under insufficient pH-buffering, Ca (and Mg) go up under sufficient Ca-carbonate buffering and Fe(II) increases when oxygen is limitedly present. The dissolution rate of calcite is much higher than that of dolomite per unit surface area and in their mutual presence the first will initially buffer the pH. This will subsequently have an effect on cation exchange reactions.

The release of iron and sulfate can result in the formation of Fe-oxyhydroxides, under more neutral pH, gypsum ($CaSO_4 \cdot 2H_2O$) and, under more acid pH, jarosite ($KFe_3(OH)_6(SO_4)_2$). The iron in jarosite is Fe^{3+} so the oxygen availability should be high. Both gypsum and jarosite are common products of iron sulfide oxidation (De Craen et al., 2008; 2011). Yet, since both minerals are hydrated, the pressure and temperature effect should be included. In case of disposal in clay under atmospheric conditions or excavation for a repository, the temperature and lithostatic (and gas, hydraulic) pressure in the Rupel Clay go down. At conditions prevailing at depth, the potential pressure and temperature effect on the formation of hydrated minerals needs to be taken into account and instead of hydrated minerals, unhydrated variants such as anhydrite might need to be included. The temperature above which anhydrite precipitates instead of gypsum depends on the groundwater composition and the pressure, but can be as low as 14°C (MacDonald, 1953). Depth of conversion of gypsum to anhydrite can range between 400 m for rocks overlain by e.g. shale or gypsum, and >4 km when overlain by salt (Jowett et al., 1993).

In practice, no acidification due to sulphate oxidation was found in piezometers at locations of clay repositories (ONDRAS-NIRAF, 2001). Elevated sulphate concentrations were, however, reported indicating the occurrence of pyrite oxidation (De Craen et al., 2011). Inspection of fracture zones induced by excavation of drifts in the underground showed gypsum indicating pH-buffering by Ca-carbonate (Vinsot et al., 2014). It is expected that diffusion is the dominating process because of the very low vertical hydraulic permeability of the clay matrix ($K_v \approx 10^{-12}$ m s^{-1}; ONDRAS-NIRAF, 2001). The effects of oxidation on the Belgian Boom Clay were modelled by De Craen et al. (2008). Oxygen is expected to penetrate into the Boom Clay over 50 years to a maximum depth of 4 meters (Fig. 4.4). This was calculated without taking into account geochemical consumption. When this is taken into account, a higher amount of oxygen is expected to diffuse into the Boom Clay, but the concentration of oxygen in the Boom Clay is expected to be less, both because of geochemical consumption. The oxidation accounted for was considered to be due to construction and operation of a geological repository. In such a repository, immediate contact exists between air and the Boom Clay. Hence, it is an open system at the outer face of the Rupel Clay. The concept for the diffusion modelling is similar to some extent to the oxidation as a result of postglacial erosion. The main difference is in the time scale, which is only tens of years for the excavation scenario. In addition, boundary conditions and the Rupel/Boom Clay characteristics are somewhat different for the Dutch and Belgian cases. The sulphate concentration due to oxygen diffusion and associated pyrite oxidation was modelled using PhreeqC (De Craen et al., 2008). The sulphate concentration within the excavation damaged zone diminishes fast (Fig. 4.5). The majority of the sulphates mobilised are transported towards the gallery, while the diffusion of the sulphates further into the host rock is very slow, even after 50 years. The extent of oxidation remains limited to a few meters. The limited range of influence is caused by the absence of advection and the low effective diffusion coefficient in this medium.

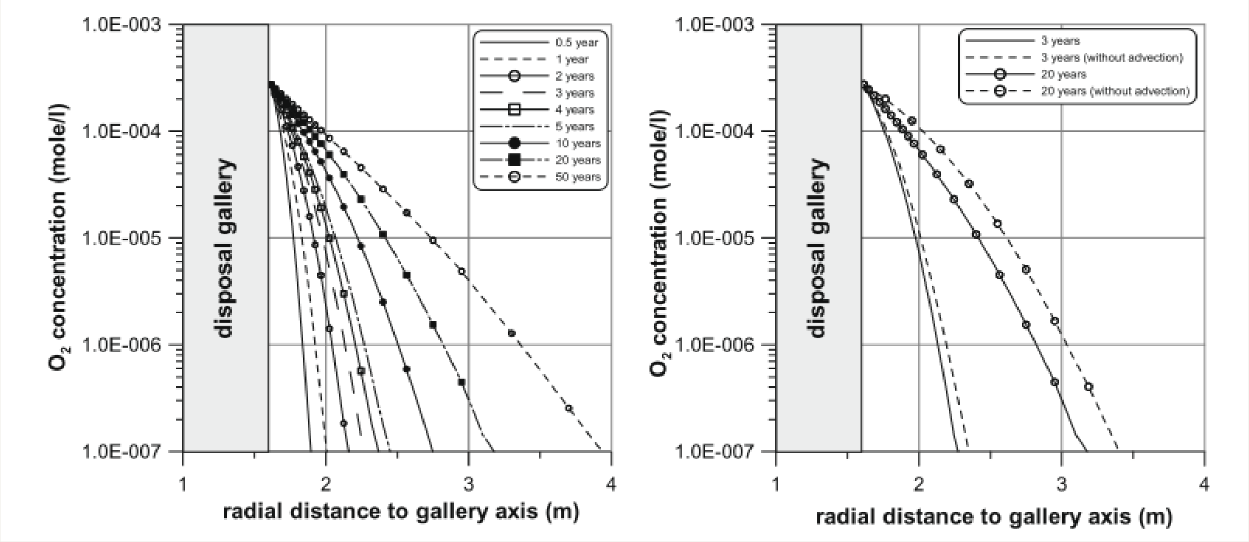

Figure 4.4. Modelled oxygen profiles in Boom Clay, without taking into account chemical consumption (De Craen et al., 2008).

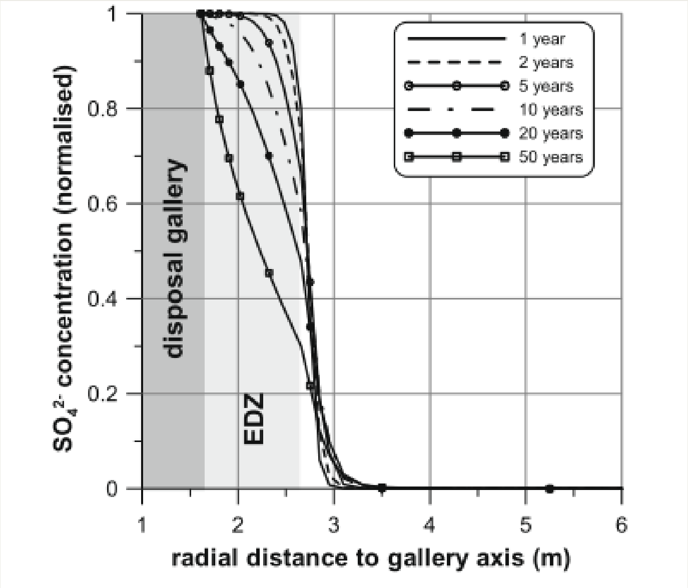

Figure 4.5. Modelled sulphate concentration profiles in Boom Clay (De Craen et al., 2008).

4.3.Degradation of organic material

There is information about the nature of the Rupel or Boom Clay incl. organic matter content (Van Geet et al., 2003; Koenen & Griffioen, 2014; 2016; Bruggeman & De Craen, 2012) as well as for other comparable locations (e.g. Michels, 2003). The organic content of the Dutch Rupel Clay varies around 1 % (Koenen & Griffioen, 2014; 2016). The organic matter is immature and the past diagenetic evolution has been very minor (Deniau et al., 2001; 2004; 2005). However, oxidation of the organic matter is mainly expected to take place upon exposure to oxygen. Michels (2003) concluded for a similar clay that, for the next 1 My, it is most likely that the organic material will thermally not evolve further. Any reactions are mainly expected to occur due to perturbations. There is potential reactivity towards oxidation and biodegradation; however, the limiting factor is also the availability of oxygen or other oxidizing agents as SO_4.

4.4. Microbial reactions

It is quite certain that there are active microorganisms present in the Rupel Clay (e.g.: Boivin-Jahns et al., 1996; Wouters et al., 2013). These are expected to become more active when exposed to chemical redox gradients. Here, microbial activity is expected to remain very limited in the undisturbed far field, whereas enlarged microbial activity can be expected at locations with enhanced oxidation or other forms of perturbation in particular with respect to redox state. Such examples are fractures due to excavation, where entry of air is enhanced (Vinsot et al., 2014) and H_2 production by corrosion of steel (Bagnoud et al., 2016). Especially bacteria that are active in hydrogen, sulphur and iron redox processes can be expected to become active.

4.5. Clay weathering

Reactions involving silicates are generally much slower than those involving carbonates, sulfides, sulfates and oxides. However, silicate reactions could be important at the considered time scale of 10,000 – 1,000,000 years. The clay mineralogy of the Rupel Clay consists mainly of smectite, kaolinite and illite (and their interstratified versions). A relevant question is whether the clay minerals in the Rupel Clay have a detrital origin or are authigenically produced. Both Kuhlmann et al. (2004) and Zeelmaekers (2011) explain the shifts in clay mineral assemblages in terms of provenance for Pliocene and Paleogene clays, respectively. The latter also noted variable kaolinite fractions following a Milankovitch cyclic pattern. This suggests that authigenic production or modification of clay minerals has been minor up to present in these Dutch clay units.

Two common diagenetic clay conversions are those of smectite to illite, and kaolinite to illite, with increasing depth. These two conversions have a different nature of reaction. The illitization of kaolinite involves dissolution and subsequent precipitation of the pure end-member illite (Berger et al., 1997). The conversion of kaolinite to illite has a high energy barrier, requiring either a high temperature, or influx of fluids rich in potassium (Lanson et al., 2002). In the case of a high temperature, K-feldspar could provide the potassium required for illite, although this theory is a topic of debate. At low temperature, potassium influx is required since K-feldspar would be oversaturated together with illite (Berger et al., 1997). High temperatures are not foreseen in the autonomous evolution scenario within the timeframe considered. Increased temperatures could be expected from the radioactive waste disposal, but these will not be sufficient for enhanced K-feldspar dissolution. Yet, cement degradation could result in potassium leaching into the Rupel Clay, which might lead to illitization.

The illitization of smectite would result in a release of water, sodium, magnesium and/or calcium ions in the pore fluids, due to the dehydration and a decrease in cation exchange capacity. In addition, the swelling capacity of the rock will decrease since illite has negligible swelling capacity (see next section). The illitization of smectite is a progressive process in which mixed-layered structures become enriched in end-member layers with time. It is a much more gradual process than kaolinite illitization. Although the knowledge on the exact mechanisms of the process is evolving due to improvements in characterization technologies (e.g. Berger et al., 1997, Lanson et al., 2009), the process of illitization is known to be very slow. Especially at low temperatures as prevailing in the Rupel Clay in the Netherlands, it will take millions of years (Huang et al., 1994). In experimental studies at temperatures as high as 250 to 450°C the process of illitization was observed on the time scale of (tens of) days. In addition to temperature, a high potassium activity will enhance the process (Weibel, 1999). Taking into account the thermal and temporal stability of clay minerals and realising the age of the Rupel Clay (Fig. 4.6), little conversions are also expected in the Rupel Clay (Sammartino et al., 2003).

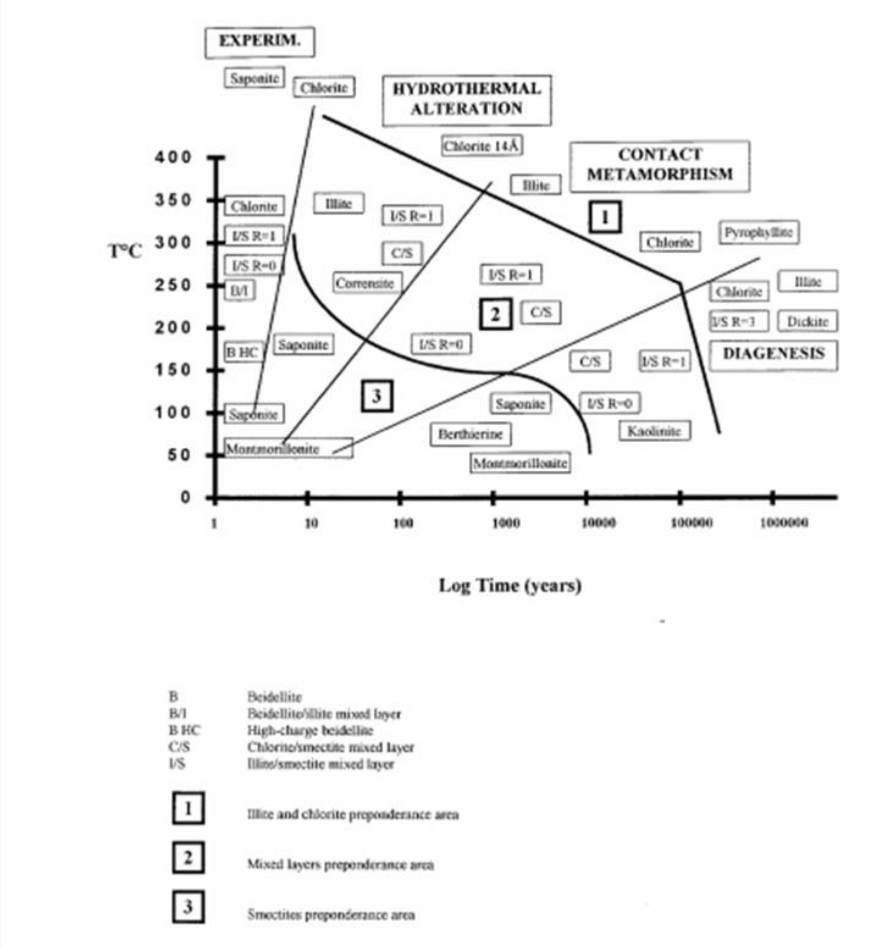

Figure 4.6. Stability of clays as a function of time and temperature (Pellegrini et al., 1999).

Hence, not much silicate weathering is expected in the Rupel Clay (as long as it does not acidify due to oxygen exposure, related pyrite oxidation and insufficient carbonate buffering; see later). The clay has already aged for ca. 30 million years with little or no authigenic clay diagenesis (Zeelmaekers, 2011). Furthermore, temperature and pressure are relatively mild, and little perturbations are probably present in the far field. Gautschi & Mazurek (2004) assessed the expected future evolution of the Opalinus Clay in Switzerland on the basis of historic data and expected not much significant development on a time scale of 1 million year. Chamley (1994) also stated that there may be changes in the near field, but little perturbations are present for the far field. Although a lot of uncertainties exist, it is generally expected that smectite to illite conversion happens at alkaline pH (Eberl et al, 1993; Srodon, 1999a; Srodon, 1999b) at ambient temperature. This is only likely to occur near the interface between the Rupel Clay and cement.

4.6. Cation exchange

Sorption reactions are important to consider as they retard the transport of actively sorbing solutes. In addition, the exchanger may act as a buffer which may alter the composition of the pore fluid (Appelo and Postma, 2005).In this workpackage we will focus on the major cations (Na, K, Ca, Mg, Al and H) and the effect of oxygenation and interaction with the EBS on cation exchange processes. The transport and adsorption of radioactive nuclides onto charged clay surfaces and organic matter is assessed in OPERA work package 6 and will not be taken into account here. Clay minerals have two types of charge. The permanent charge is negative due to ion substitutions in the tetrahedral or octahedral sheets of the minerals. A pH dependent charge originates at clay surfaces which is due to protonation/deprotonation reactions. The current state of the adsorbed (major) cations is not known for the Dutch Rupel Clay and needs to be calculated from the fluid composition and assumption about the cation-exchange selectivity coefficients of the pore matrix. This will be evaluated by the computation of the formation water composition in Chapter 5.

Little information exists on the pore water composition of the Rupel Clay in the Netherlands (Behrends et al., 2015; 2016) and this information is not representative for the situation across the Netherlands. The occupancy of the cation exchange complex can thus only be estimated for subsurface conditions of the Rupel Clay. Available information on groundwater quality above and below the Rupel Clay suggests that the pore water is predominantly brackish or saline (Griffioen, 2015).The influx of fresh, oxygenated water into the Rupel Clay will affect the fluid conditions. When freshening happens, it will result in cation exchange and eventually swelling of clay minerals because of a decrease in ionic strength (see below). In addition, the mobilisation of calcium from enhanced dissolution of calcite will result in the partial exchange of adsorbed cations such as Na^+ by Ca^{2+}.

If the clay mineralogy becomes significantly affected by long-term mineral reactions, the cation exchange capacity should be linked to the amount and type of clay minerals present. In this case, the exchange capacity is linked to the exchange site of each specific clay mineral using a value in meq/mol. Depending on the transformation, the cation-exchange capacity may increase or decrease. However, not much silicate weathering is expected and, relatedly, changes in the CEC are not of major importance.

4.7. Clay swelling

Clay swelling is a well-known phenomenon in sedimentary deposits. Kaolinite and illite have very limited swelling potential, while smectite has large swelling potential. Here, the swelling potential is dependent on the *type* of smectite. The most common smectite is montmorillonite (Zhou et al., 1997) and Na-montmorillonite is the type of smectite with the highest swelling potential. Koenen and Griffioen (2014) identified the presence of Na-montmorillonite as the main smectite mineral in the Rupel Clay in the Netherlands. The sodium in this clay mineral is present as a layer of adsorbed cations between the clay sheets and at the clay surface as a result of negative charge of the sheets. The sodium can be hydrated by attracting water molecules around it, thereby forcing the clay sheets apart. Up to three or even four layers of water molecules can be present around the sodium. This type of swelling is called ‘crystalline swelling’ (Anderson et al., 2010). The difference in clay volume between unhydrated and fully hydrated (4 water layers) Na-montmorillonite is a factor of 2. Other types of clay minerals generally have less than 3 hydration layers and therefore have less swelling potential. The number of hydration layers depends, besides on the type of clay mineral, on the type of adsorbed cation and on the prevailing conditions. The hydration potential increases with increasing relative humidity and decreasing ionic strength of the pore water, temperature and pressure (Huang et al., 1994; Laird, 2006; Anderson et al., 2010).

As discussed in the next chapter, pore water in the Rupel Clay is presumably mostly saline in the Netherlands which limits the clay swelling. A future scenario that brings freshening of the clay layer is glacial or postglacial erosion and subsequent infiltration of fresh river or rain water. This would result into a fresh Na-HCO_3 water type that brings forward optimal swelling conditions. Clay swelling may thus be a side effect of glacial or postglacial erosion.

In addition to crystalline swelling, osmotic clay swelling can occur. It occurs as an extension of crystalline swelling once the maximum number of hydration layers have formed (Anderson et al., 2010). Not everything is understood about this type of swelling, but Na-montmorillonite is known to have the highest osmotic swelling potential. According to Zhou et al. (1997) osmotic swelling occurs for a Na-montmorillonite at an ionic strength of the formation water below 0.5 M, while Ca-montmorillonite does not show the tendency for osmotic swelling even at ionic strength < 0.001 M. However, a critical water:clay ratio is required for osmotic swelling of Na-montmorillonite to occur, which is 1200 mg of water per g of clay (Anderson et al., 2010). The clay volume can then increase by a factor of 10 compared to unhydrated clay (Laird, 2006).

According to Huang et al. (1994) Na-montmorillonite with three hydration layers is stable at general P-T conditions in subsurface environments. Ca-montmorillonite can also contain up to three hydration layers while K-montmorillonite generally only has zero or one hydration layer. Hence, cation exchange of sodium or calcium by potassium could cause dehydration (shrinkage) of the clays and the release of water. This has impact on the pore structure of the sediment, as well as on the ratio of free water versus adsorbed water. Both of which are important parameters for the diffusion of radionuclides through the Rupel Clay and hence need to be taken into account if relevant.

4.8. Conclusions

On the basis of literature, no large geochemical changes of the Rupel Clay are expected at a time scale of 1 million years without natural or man-induced perturbations. This is expected on the basis of the relatively old age of the clay (ca. 30 million years) and the absence of strongly perturbing factors. The clay is in reduced state and the reduction state is probably determined by the omnipresence of pyrite. The low permeability also helps to maintain a stable state as the inward fluxes of reactive solutes will be small associated with groundwater transport.

Potentially relevant factors that were assessed are: clay weathering, organic matter degradation and microbially mediated conversion. Clay weathering is expected to be limited because of the absence of extreme pressure, temperature or pH which is required for significant clay weathering. Organic matter degradation is expected to be limited because of the constant reducing conditions which have stabilized the current state of organic matter, and the absence of factors which change this (specifically, oxidizing conditions). Microbially mediated conversions are expected to be limited because of the absence of chemical gradients which are necessary for these.

The major factor potentially causing changes of the Rupel Clay is formed by glacial events, and most specifically postglacial erosion. This might lead to exposure to oxygenated surface water and, due to pressure differences, advective flow, which might cause geochemical reactions.

5. Rupel Clay pore water composition

5.1. Introduction

Since the pore water composition of the Rupel Clay could only be established for relatively shallow depth in Zeeland (Behrends et al., 2015; 2016), geochemical modelling was performed to simulate the composition in (near-)equilibrium with the mineralogy of the Rupel Clay as defined in task 5-2-1 (see section 2.1).

Gaucher et al. (2006) developed a thermodynamic model to calculate the 'mobile' pore water chemistry for clay-rich formations. This model computes the water chemistry which can be sampled by in situ experiments. Leroy et al. (2007), alternatively, developed a geochemical equilibrium model which incorporates an electrical triple layer (more often referred to as diffuse double layer) model for adsorption reactions. This is important with regard to microporosity where the electrical double layers of two opposite clay surfaces overlap, since the mean solution composition in these pores will not obey the classical electroneutrality condition (Leroy et al., 2007). In their model, the computation is separated for the macropores and the micropores with a cut-off between the two groups determined by the diffuse layer thickness, which depends on the ionic strength of the pore water. Our approach is somewhat simplified and computes an average formation water composition, excluding the part of the pore space where the classical electroneutrality condition is not obeyed. One may assume this equals the 'mobile' pore water chemistry.

The geochemical modelling of the Rupel Clay formation water composition and the long-term autonomous evolution was performed with the geochemical computer code PHREEQC-3 (Parkhurst and Appelo, 2013). The thermodynamic PHREEQC database (as delivered by USGS) was used. The database was adapted to include cation exchange species for clay surfaces and organic matter (see later). In our simulations, the starting composition for the pore fluid is a seawater composition. This formation water is equilibrated with several mineral phases and the CEC: the major cations Na^+, K^+, Ca^{2+}, Mg^{2+} and Fe^{2+} as well as H^+ are involved in cation exchange. Aluminium is controlled by gibbsite, as Fest et al. (2007) showed that shallow groundwater in the Dutch subsurface is generally in near-equilibrium with gibbsite. Silica is controlled by quartz assuming an supersaturated state with a saturation index (SI) of 0.5. This implies near-saturation for chalcedony and corresponds to average values in formation waters in the Dutch subsurface (as observed in the groundwater quality database established by Griffioen et al., 2013). Pyrite controls the S^{2-} and Fe^{2+} concentrations where pe was fixed at 0 and SO_4 at seawater concentration. We consider the majority of the clay minerals not to be reactive for fixing the pore water composition by solubility reactions (De Craen et al., 2004a).

Carbon dioxide dissolved in formation water can have either external or internal control. Internal control is the result of equilibrium between the formation water and the (carbonate) minerals. External control would imply influx from an external source. For the purpose of this task, we assume some influence from in-situ organic matter degradation and negligible external controls under present-day conditions. In correspondence to the values from the database of groundwater samples from deep wells as reported in Griffioen (2015), we assume an average log CO_2 partial pressure of -1.5. The formation water is further assumed to be in equilibrium with calcite. This combination fixes the Ca concentration and alkalinity. For the Boom Clay in Belgium, Wang et al. (2010) considered that the partial pressure of CO_2 would be controlled by the mineral assemblage, so that the fugacity is only a function of temperature. At a temperature of 25°C the partial pressure would be $10^{-2.8}$ atmosphere. For the Callovian-Oxfordian formation in France, measurements of the CO_2 partial pressure gave values of $10^{-2.15}$ to $10^{-2.9}$ atmosphere

(Gaucher et al., 2006). Hence, the partial pressure in our model is assumed to be somewhat higher, probably as a result of more extensive anaerobic organic matter mineralization.

5.2.Model input

5.2.1. Mineralogy

The mineralogy used in this chapter is based on the average whole rock XRD mineralogy, as shown in Table 2.1. The mineralogy was corrected for the artefacts from pore water evaporation and oxidizing storage conditions. Sylvite, halite and jarosite were removed from the composition. The first two are likely the result of pore water evaporation, whereas jarosite is an oxidation mineral assumed to have formed after coring. Gypsum is also assumed to be an artefact of pyrite oxidation and calcite buffering and its content was added to the pyrite and calcite contents. Anatase was not taken into account and removed from the composition. The remaining minerals were normalized to 100%. The kaolinite content was taken from the whole rock XRD analyses. The normalized 2:1 clay fraction from the whole rock XRD was divided over illite and smectite, thereby assuming 30% of the 2:1 clay to be illite and 70% smectite. Because of the pH buffering capacity of $CaCO_3$ upon pyrite oxidation and the variation in $CaCO_3$ and pyrite contents (see Chapter 2), we will consider different mineralogy scenarios for the autonomous Rupel Clay evolution and the far-field Rupel Clay evolution due to disposal of radioactive waste (see Chapter 7). Three different cases were initially defined (Table 5.1):

- Case A: average mineralogy as described above;
- Case B: the maximum $CaCO_3$ content. The mineralogy is normalized to 100%;
- Case C: the maximum pyrite content is used. The corresponding low $CaCO_3$ content of the particular sample is used. The mineralogy is normalized to 100%.

Cases A and C were systematically used for transport simulations as it turned out that case B did not provide additional insights.

5.2.2. Cation exchange

The current CEC value is not known for the Dutch Rupel Clay except for a few measurements for samples from Borssele and Limburg (Behrends et al., 2015; 2016). We estimated the CEC from the clay mineralogy using the XRD analysis for a series of Rupel Clay samples (Koenen & Griffioen, 2014). The total bulk charge density of a clay-rich rock or sediment can be calculated using the grain density, the connected porosity and the cation exchange capacity of the medium. Considering average clay mineral contents and average mineral specific CEC values, a total CEC of 295 meq/kg (29.5 meg/100g) rock material is assumed (Table 5.2). This is slightly higher than the values measured by Behrends et al. (2015; 2016) for drillings in Zeeland of 18.5 ± 4.5 meq/100 g and samples from Limburg of 11.5 ± 1.3 meq/100 g. It is in the high end of the range of values measured by Honty (2010) for Boom Clay in Belgium of 7-30 meq/100 g.

Table 5.1. Mineralogy of the three cases defined. The mineralogy in mol/kg water is based on a porosity of 20% and full water saturation.

	molar mass	molar vol.	density	**Mineralogy (wt%)**			**Mineralogy (mol/kg water)**		
	(g/mol)	(cm3/mol)	(g/cm3)	A	B	C	A	B	C
Quartz	60.08	22.69	2.65	42.0	34.7	40.7	75.45	62.33	75.50
Albite	262.3	100.28	2.62	2.4	2.0	2.4	1.00	0.82	1.00
K-feldspar	278.33	108.87	2.56	6.7	5.5	6.5	2.59	2.14	2.60
Clinoptilolite/Heulandite	1344.40	625.30	2.15	0.6	0.5	0.5	0.04	0.04	0.04
CaCO3	100.10	36.93	2.71	5.3	21.8	1.3	5.67	23.53	1.42
Pyrite	119.98	23.94	5.01	1.4	1.2	8.3	1.27	1.05	7.74
Chlorite	341.70	106.78	3.20	1.1	0.9	1.1	0.36	0.30	0.36
Kaolinite	258.16	99.52	2.59	4.1	3.4	4.0	1.71	1.41	1.71
Smectite	367.01	134.27	2.73	25.4	21.0	24.6	7.48	6.17	7.48
Illite	384.00	138.98	2.76	10.9	9.0	10.6	3.06	2.53	3.06
Sum				100	100	100			

Table 5.2. Cation exchange capacity (CEC) values for the clay minerals and organic matter. Average (initial) mineral and organic matter specific CEC values are taken from Appelo and Postma (2005). For organic matter, the following equation is used: 510*pH-590 = CEC per kg organic carbon. A pH value of 7 is applied as reference.

	wt%	mineral specific CEC (meq/kg)	meq/kg
Smectite	25.1	1000	251
Kaolinite	4.0	90	4
Illite	10.9	350	38
Chlorite	1.1	250	3
Total charge (clay)			**295**
Organic matter	0.9	2827	25

The CEC (simulated by PHREEQC using the Gaines and Thomas convention) as available for basic cations is pH-dependent due to the occupancy of H^+. The cation-exchange between H^+ and cations as Ca^{2+} is called proton-buffering and depicted as:

$$HX + \frac{1}{2} Ca^{2+} \leftrightarrow \frac{1}{2} Ca\text{-}X_2 + H^+$$

The actual CEC increases with about 10-20% per pH unit, where the pH-effect is larger for organic matter than for clay minerals (e.g. Helling et al., 1963). As simple assumption, we set the pH-dependent charge to 25 meq/kg and the pH-independent charge to 295 meq/kg. Transport modelling scenarios (see Chapter 6) were also run where the pH-dependent charge was set to 30% of total CEC.

Recalculation of the permanent CEC (meq/kg material) into concentration (meq/L pore water) as should be defined in the PHREEQC input (eq/ L pore water) can be done as follows (Appelo and Postma, 2005):

$$CEC_{meq/l(w)} = CEC_{meq/kg(s)} \times \rho_s \times (1-\theta)/\theta$$

where θ is the porosity and ρ_s is the solid mass density. Assuming a solid mass density of 2.7 kg/l (which is the approximate density for smectite) and a porosity of 20% results in a pH-independent CEC of 3186 meq/L pore water and a pH-dependent CEC of 270 meq/L pore water. The exchange coefficients for the major cations used in the modelling are relative to the adsorption coefficient of Ca^{2+} (Table 5.3). Exchange coefficients for other cation-pairs are calculated by combining two reactions of different cations relative to Ca^{2+} (Appelo and Postma, 2005). Note that two constants were used for H^+ to mimick buffering at different pH-trajectories (see next chapter).

Table 5.3. Log K_1 values for permanent CEC (based on Bruggenwert & Kamphorst, 1982) and Log K_2 values for pH-dependent CEC from Smidsrod & Painter (1984). Both are relative to Ca^{2+}, which has Log K of 0.

	Log K_1	Log K_2
Na^+	-0.3	-0.85
Fe^{2+}	-0.36	0
K^+	0.3	-0.70
Al^{3+}	0.9	0.9
Mg^{2+}	-0.2	-0.3
H^+	0.6	5.08 or 6.58

5.2.3. Formation water simulations

The NaCl concentration in groundwater is generally high at depths below which meteoric water circulations and fresh water is dominant although it may vary considerably (Chapter 2.2). We used seawater as a starting composition for the formation water calculation (Table 5.4) as it appears that the salinity of formation water in the Rupel Clay probably varies around seawater salinity. Seawater has a chloride concentration of approximately 19,000 mg/l, a usual pH of 8.2 and an oxic redox state. The redox state we used in the model was lower due to subsurface anoxic conditions and in order to prevent oxidation of pyrite. Two additional scenarios assume mixing with brackish water (brackish water scenario) and evaporation of the seawater (highly saline water scenario). For this purpose, the elemental concentrations are respectively divided and multiplied by 4 (Table 5.4).

In principle, the high NaCl concentration requires the Pitzer database, which is specifically developed for systems with a high ionic strength. However, the number of mineral phases, in particular Fe-minerals, is insufficient in this database for the purpose of this study. Instead, the effect of high ionic strength will be discussed on a qualitative basis.

Table 5.4. Composition of formation water for the brackish water, seawater and highly saline water scenarios (mmol/l) used in the model.

	Brackish water	Seawater	Highly saline water
Ca	2.5	10.0	39.9
Cl	134.0	536.0	2143.9
K	2.4	9.7	38.9
Mg	13.9	55.6	222.2
Na	114.1	456.5	1826.1
S(6)	7.0	28.1	112.4

The mineral and gas phases equilibrated with the pore water scenarios from Table 5.4 to control elemental concentrations are shown in Table 5.5. In the base case, the seawater is equilibrated with the exchangers and the equilibrium phases. Note that regular seawater is supersaturated for calcite and aragonite while CO_2 pressure is close to atmospheric. The assumptions made thus deviate to encompass the subsurface conditions: the CO_2 is elevated due to sedimentary organic matter degradation and calcite equilibrium is assumed due to additional dissolution of Ca-carbonate. The temperature is based on a Rupel Clay depth of 500 m. Following the equation from Bonté et al. (2012):

$$\text{Temperature} = 10.1^\circ\text{C} + \text{depth} \times 31.3^\circ\text{C/km},$$

where 31.3ºC/km represents the Dutch geothermal gradient. This results in a temperature of 26°C.

Table 5.5. Equilibrium phases and corresponding control used in the model.

	SI	Controls
Quartz	0.5	Si
Calcite	0	Ca
SO_4 + pe		S(-II)
Pyrite	0.3	Fe
Gibbsite	0.0	Al
CO2(g)	-1.5	C

5.3.Results

Figure 5.1 and Table 5.6 show the computed formation water composition for the three different scenarios. Figure 5.1 also shows the pH and pe values and the amounts of CO_2 and calcite dissolution. Figure 5.2 shows the adsorbed species onto clay and organic matter. The concentrations of aluminium and iron are low in each scenario. The calcium, iron, potassium, magnesium and sulfur concentrations are, just like sodium and chloride, highest in the evaporated seawater scenario, whereas the carbon, aluminium and silicon concentrations are lowest. The amounts of gibbsite and quartz dissolution slightly increase with decreasing ionic strength, which explain the aluminium and silicon concentrations. The carbon content is determined by a more complex interaction of CO_2 production and calcite equilibrium. The pyrite dissolution slightly *decreases* with decreasing ionic strength. Yet, the iron and sulfur trends are the result of input values since the contribution of pyrite dissolution is negligible.

Table 5.6. Formation water composition computed for the three scenarios.

	Computed values (mmol/kg water)		
	Brackish water scenario	**Seawater scenario**	**Very saline water scenario**
Al	4.1E-05	3.3E-05	1.2E-05
C	7.4	7.2	5.6
Ca	5.7	13.2	44.0
Cl	134.3	541.0	2227.0
Fe	2.7E-06	3.1E-06	3.5E-06
K	2.4	9.8	40.4
Mg	13.9	56.1	230.8
Na	114.4	460.9	1897.0
S	7.0	28.4	116.8
Si	0.3	0.3	0.2
pH	7.0	6.9	6.5
pe	-2.9	-2.8	-2.4

The pH values are 7.0, 6.9 and 6.6 for the three scenarios, corresponding with increasing CO_2 dissolution at higher ionic strength. Calcite precipitates in the evaporated seawater scenario, while it slightly dissolves in the other two scenarios, probably due to the higher CO_2 dissolution and consequently lower pH.

Behrends et al. (2015) reported in OPERA deliverable UTR521 on the measured formation water composition of samples from several core sections of Rupel Clay in Zeeland. They suggest a strong seawater signature, and potential oxidation of the clay in an erosion event prior to deposition of the current overlying Breda Formation. They also proposed that pyrite and calcium carbonate dissolution, followed by microbial sulphate reduction and removal of dissolved sulphate by gypsum precipitation could have affected the pore waters in the measurements but not necessarily in situ.

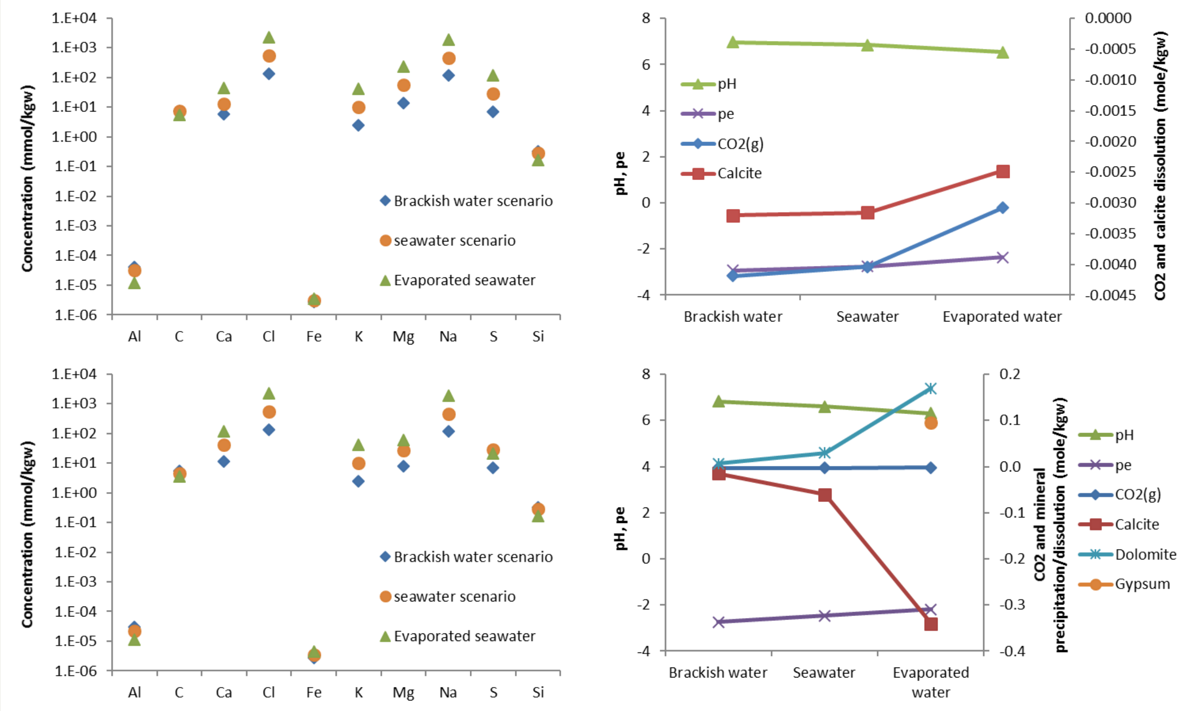

Figure 5.1. Formation water composition computed for the three scenarios (left) and the pH and pe values, and the CO_2 and mineral dissolution (right) for the three different scenarios. In the bottom two graphs, dolomite and gypsum precipitation are included. Note the difference in axis scale for the graphs on the right.

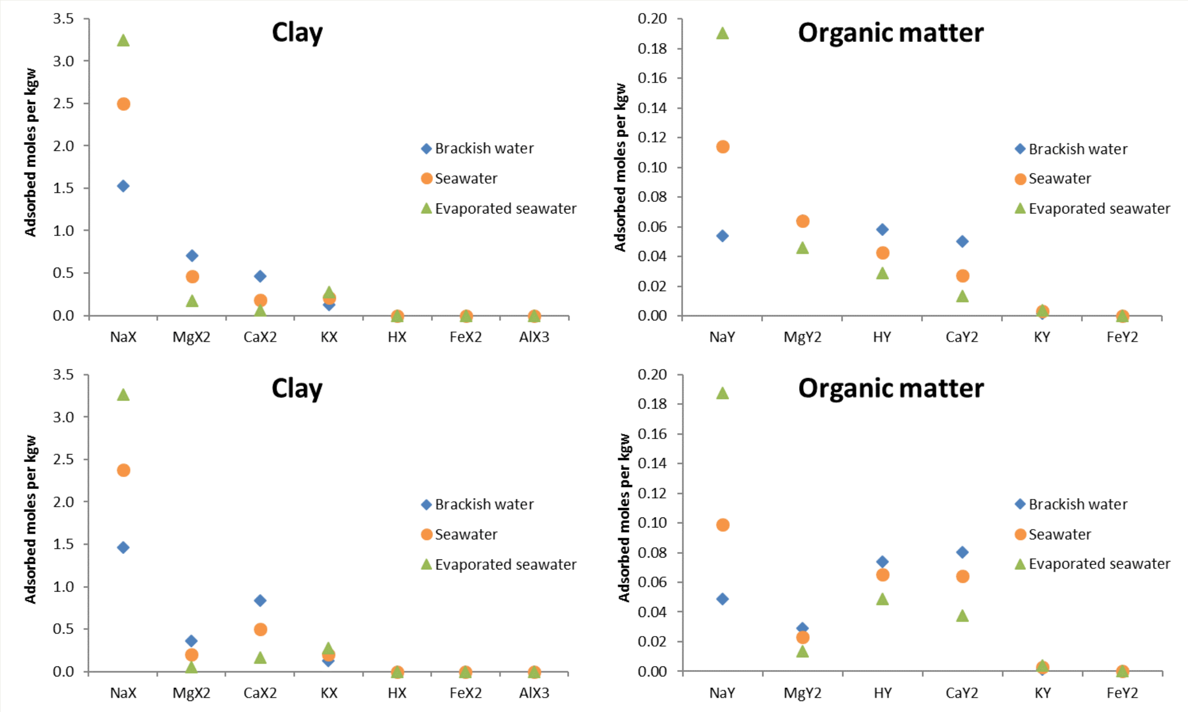

Figure 5.2. Adsorbed species onto clay (pH-independent; left) and organic matter (pH-dependent; right) for the three different scenarios. In the bottom two graphs, dolomite and gypsum precipitation are included.

For the simulation performed, the model predicts that several minerals have a positive saturation index (SI). These include K-mica, kaolinite, dolomite, Ca-montmorillonite, chalcedony and illite. In the seawater scenario, K-feldspar and talc also have a positive SI and in the evaporated seawater scenario both K-feldspar, talc and gypsum are oversaturated. It is possible that the formation water is at or near equilibrium with dolomite and gypsum, but the other minerals involve silicate reactions which are not assumed to take place in the Rupel Clay due to the slow kinetics and high activation energy of these reactions at the prevailing conditions.

The SI value of both dolomite and gypsum are near or well below 1 in each of the scenarios. Including dolomite and gypsum as secondary minerals results in the precipitation of (small amounts of) dolomite in each of the scenarios, and gypsum only in the evaporated seawater scenario (Figure 5.1). In the evaporated seawater scenario, the dolomite precipitation goes hand in hand with increased calcite dissolution. Slight changes in the formation water composition and adsorption (primarily Ca and Mg) occur (Figures 5.1 and 5.2).

6. Geochemical evolution of the Rupel Clay – impacts of postglacial erosion and mine galleries

The focus of this chapter is the long-term evolution of the Rupel Clay under autonomous conditions or impacted by mine galleries. The related question is whether the geochemical conditions of the Rupel Clay may change in time which might affect the boundary conditions for transport of radionuclides from the repository through the Rupel Clay.

6.1. Thermodynamic equilibrium considerations

First, a preliminary thermodynamic batch model was run to assess the type of mineral reactions to be expected in the Rupel Clay induced by oxidation with oxygen. In addition, a reference model was run without the contribution of oxygen to evaluate the thermodynamic stability of the input mineralogy. This thermodynamic batch modelling indicates the importance of primary and secondary minerals relevant in the oxidation scenario. In thermodynamic models, K-feldspar and kaolinite are for example not in equilibrium together and they should react to form illite and quartz until one of the two source minerals is exhausted. In rocks, the coexistence of these minerals is omnipresent. This discrepancy between models and actual rocks is due to kinetic limitations which may not be represented in the modelling software. Therefore, the best way to investigate reactions resulting from a perturbation such as oxidation is to subtract the results from a reference model; any predicted reaction which did not occur in real life in the clay rocks due to such limitations will also be predicted in the reference model. Models were run with the seawater scenario and mineral composition A as shown in Table 5.2.

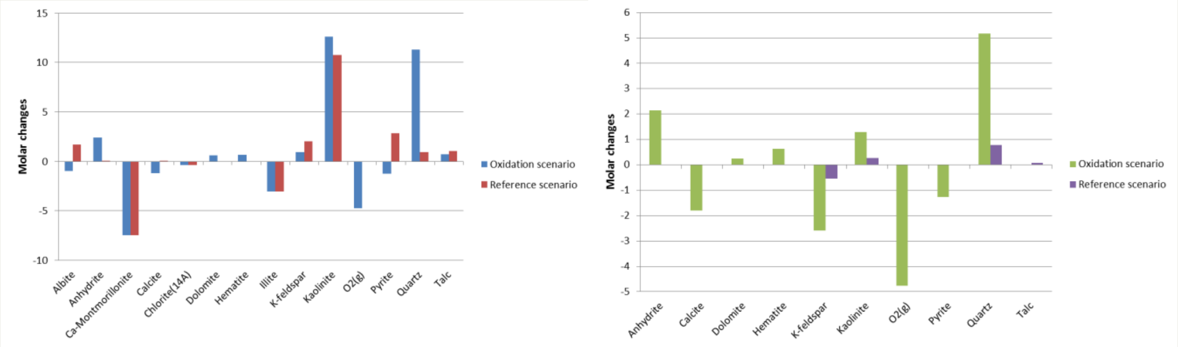

Figure 6.1. Molar changes resulting from the thermodynamic batch models for the oxidation and reference scenarios. Left: including all reaction. Right: eliminating the silicate reactions unrelated to oxidation.

The results of the thermodynamic batch modelling are shown in Figure 6.1 where the prominent silicate minerals were also considered. The results show that in both scenarios, if all mineral reactions are allowed, montmorillonite, illite and chlorite are unstable and react to form primarily kaolinite and quartz, and some additional K-feldspar and talc. Since these minerals are present in the rocks, reactions kinetics are too slow or activation energies too high to have initiated or finalized at this point in time. The mineralogy of the Rupel Clay is thus in disequilibrium with itself which is not surprising but important to realise for a 30 million years old clay layer. After eliminating the silicate reactions which are not predicted to occur as a result of oxidation, the following reactions occur: the partial oxidation of pyrite and the formation of Fe-oxides and gypsum or anhydrite. In addition, calcite partially converts to dolomite, and enhanced K-feldspar conversion to kaolinite and quartz. The latter may also be questioned kinetically as these hydrochemical processes are also slow at ambient conditions, but they could be relevant at the long time scale and elevated temperatures. Here, one may note that slow mineralisation of sedimentary organic matter was not considered.

6.2. *Impact of postglacial erosion*

6.2.1. Model set-up

A model study was performed to assess the effects of oxidation due to postglacial erosion. The reason to focus on this process is that severe oxidation of marine clay may cause acid sulphate soils. This leads to environmental conditions that are strongly different from the present ones. Preference was given to a simple geochemical modelling set-up in which the following hydrogeochemical processes were included:

- Pyrite oxidation due to presence of dissolved O_2 with kinetics faster than time scale considered (i.e. reaction kinetics faster than advective/diffusive transport of dissolved species)
- Equilibrium with calcite at seawater-supersaturation SI of 0.3 when present
- Cation-exchange including pH-dependent proton-buffering.

This model shows some similarities with the model study by De Craen et al. (2011) who modelled the effect of oxidation in the mine gallery. A difference with the approach used by De Craen et al. is that we do not use a cylindrical geometry, but a planar geometry. Furthermore, a longer time scale was considered: whereas De Craen modelled effects over a timescale of 0 to 50 years, we modelled effects with a maximum exposure time of 10,000 years. For exposure after postglacial erosion, this is a worst case scenario, because fast sedimentation is expected after exposure (Gunnink, pers. comm.) and the levels of oxygen that the clay is exposed to are expected to rapidly decrease again. We, therefore, also prepared a subsequent scenario for which infiltration of anoxic seawater happens as if coverage with marine clay occurred.

Figure 6.2. Schematic representation of the 1D diffusion model, showing a cell 0 with oxygenated water on top of a column of cells representing the Rupel Clay. Each Rupel Clay cell is representative of 1 liter of fluid in contact with the Rupel Clay mineralogy based on a porosity of 20%.

Figure 6.2 shows a schematic representation of the 1D diffusion model. Oxygenated water is present on top of a column of Rupel Clay cells. The water composition equals the natural River Rhine composition (Table 6.1; Molt, 1961) equilibrated with an O_2 partial pressure of 0.2 atmosphere (atmospheric oxygen partial pressure). This water composition represents glacial water penetrating the Rupel Clay as if river bank infiltration is happening. The dissolved oxygen diffuses downward into the Rupel Clay, which is present in a reduced state. This will result in oxidation of reduced minerals (particularly pyrite) and associated geochemical effects. The temperature of this water is assumed to be 4°C and is hence lower than the Rupel Clay pore water but mimicks yearly average air temperature under a cold climate. This results in a temperature gradient and corresponding heat diffusion. The oxygenated water is represented as a solution 0 in the model with constant composition, i.e., the solution is renewed every time step. This implies that ions can also diffuse from the Rupel Clay into the oxygenated water corresponding with mass leaching towards the water on top of the Rupel Clay. Goethite equilibrium was maintained in this cell 0 which implies that any Fe(II) that diffuses out of cell 1 will be oxidised and precipitated. This affects the redox balance for the first cells.

Table 6.1. Composition (in mg/l except pH) of natural River Rhine water (Molt, 1961) as used as input.

pH	Cl	Alkalinity (as HCO_3)	SO_4	Na	K	Ca	Mg
8.0	12	160	35	5	5	50	10

A column of 30 meters is modelled and three hydrological conditions were modelled:

1. Only molecular diffusion (while cell length was 20 cm)
2. Advective pore water velocity of 1 mm/y with molecular diffusion and cell dispersivity of 3 cm (while cell length was 10 cm)
3. Advective pore water velocity of 10 mm/y with molecular diffusion and cell dispersion 5 cm (while cell length was 20 cm)

For the purpose of this task we assume that the diffusion coefficient and diffusion accessible porosity are the same for all solution species, similar to the approach by Wang et al. (2010). Anion exclusion and chemical osmosis were thus not considered (cf. Chapter 9). We assume a diffusion coefficient in bulk water (D_0) of $2 \cdot 10^{-9}$ m^2/s, a diffusion accessible porosity (θ) of 0.2, a tortuosity (τ) of 1.5 and a constrictivity (δ) of 1. Using the following approach from Bruggeman et al. (2010) to calculate the effective diffusion coefficient:

$D_{eff} = D_0/F$ and $F = \tau^2/(\theta \cdot \delta)$,

we obtain a D_{eff} of $8.9 \cdot 10^{-11}$ m^2/s. Wang et al. (2004) assumed a diffusion coefficient of $1 \cdot 10^{-10}$ m^2/s for the Belgian Boom Clay, which is the same order of magnitude as our value. For the Callovo-Oxfordian Clay a value one order of magnitude lower is used (Wang et al., 2004). Corresponding porosities are 0.37 and 0.16 for Belgian Boom Clay and Callovo-Oxfordian Clay, respectively.

Porosity or water content values are not available for the Rupel Clay in the Netherlands. In Belgium, a water content of 18 wt% was calculated and used to scale the mineralogical input, with an estimated porosity of 37 vol% (Wang et al., 2010). The Rupel Clay is located at much greater depth in the north of the Netherlands than in Belgium and hence a lower porosity can be assumed. Based on two different approaches for the calculation of porosity, Vis and Verweij (2014) suggested porosity values for the north of the Netherlands of 0.14-0.22 and 0.29-0.41. For this study, we assume a porosity at the low end of this range of 0.2. The mineral concentrations used in the model are scaled to a water content of 1 liter. Since the water saturation is 1, the model is based on a rock mineral volume of 4 dm^3 and hence a total rock volume of 5 dm^3.

Different scenarios were defined with respect to proton-buffering: the logK value of exchange constant for H^+ was varied between 5.08 and 6.58 and the pH-dependent CEC was varied between 10% and 30% of total CEC. This results in different pH trajectories where proton-buffering is strongest and differences in buffering intensity: the occupancy of the exchanger with H^+ will vary in a limited pH range depending on the logK value. It turned out that the pH could rise to about 10 (see later), which implies that any proton-buffering is important as the carbonate equilibria are influenced by this. The pore water composition of the seawater scenario is used, as calculated in Chapter 5. The mineral composition for two scenarios were used (Table 5.2): average composition and maximum pyrite content. The latter would provide the largest risk for acid sulphate soils when related Ca-carbonate is insufficient for pH-buffering upon pyrite oxidation.

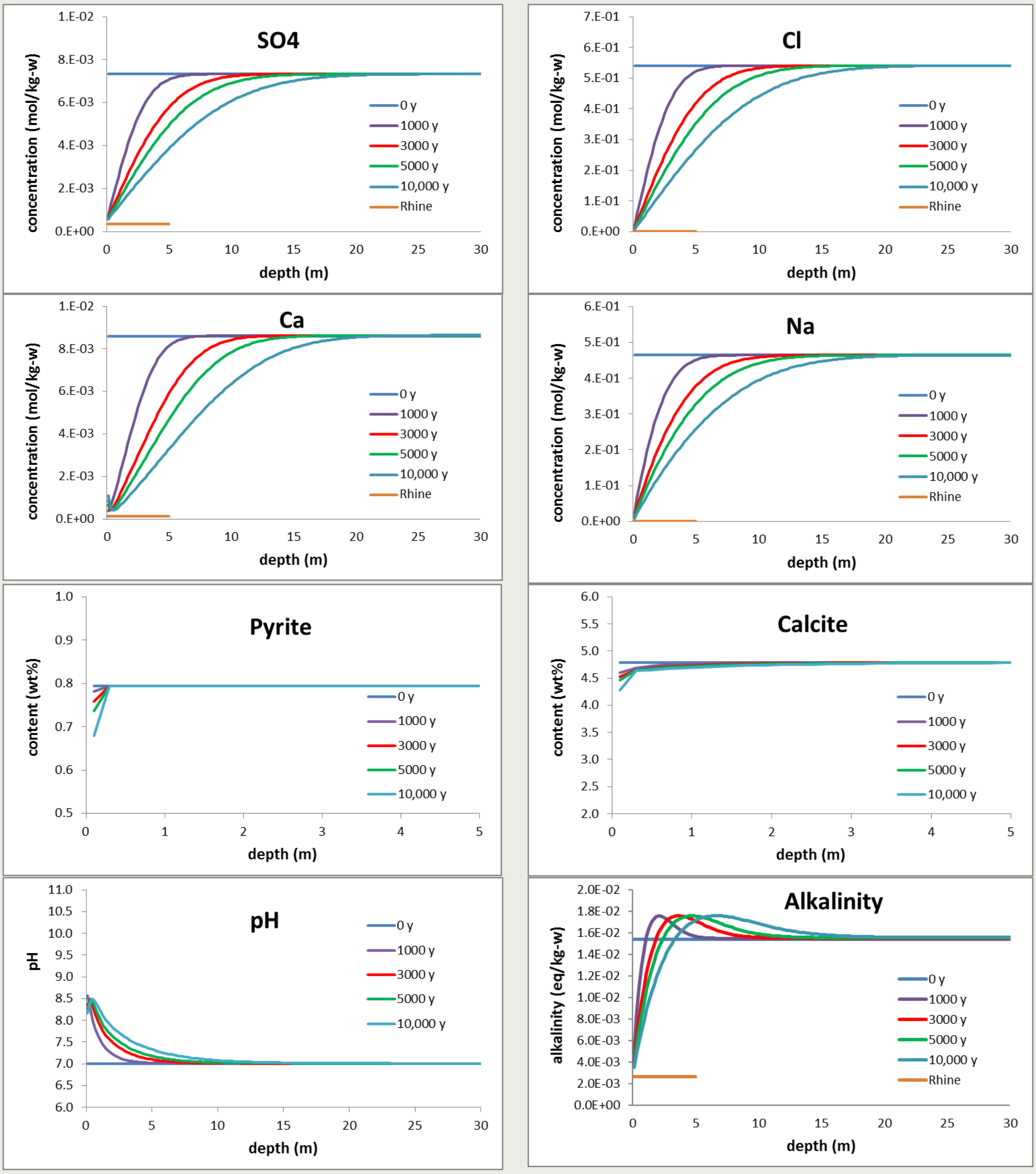

Figure 6.3. Concentration-depth profiles for reference scenario of diffusion of fresh, oxic water in Rupel Clay with anoxic seawater. Note the difference in scale for the x-axes.

6.2.2. Diffusive transport control

The results for the reference scenario on diffusive transport are shown in Figure 6.3. The modelling describes the diffusion of fresh water with dissolved oxygen into the Rupel Clay over time. The depth to which the oxygen itself diffuses remains limited to the first grid cell of 0.2 m, even over prolonged time scales, due to geochemical buffering by pyrite oxidation. The pyrite contents gets lowered with 0.1% to 0.7% and the lowering of the calcite content is also small. The clay layer is thus well-buffered against this perturbation. The low solubility of oxygen in water and the slow diffusion through the clay rocks, combined with fast pyrite oxidation limit the penetration depth of the sediment oxidation. The extent of the depletion is, however, affected by the grid size. The sulphate profiles show an increase in concentration above the fresh water concentration due the release from pyrite oxidation and the subsequent transport of the sulphate formed due to diffusion. The breakthrough curves, however, are not that different from that for Cl.

The largest effect of inward diffusion of oxic fresh water is on the pore water composition. As indicated by Cl, Na and Ca, the ionic strength of the pore water decreases in the upper part of the Rupel Clay down to 15 m depth in the course of 10,000 y due to outward diffusion of dissolved ions. The pH increases slightly because infiltrating water has a higher pH. The maximum pH of 8.5 lies above this value and calcite dissolution must be responsible for this. Cation exchange must occur due to replacement of a saline Na, Mg-Cl solution by a fresh Ca-HCO3 solution: Na and Mg are exchanged against Ca. However, its impact is not clearly reflected in the breakthrough curves as those of Ca and Na look rather similar to that of Cl. This is typical for cation-exchange under diffusive conditions (Appelo & Willemsen, 1987).

6.2.3. Effects of advection

For the act of advection, it is important to consider whether the advective flow is upward or downward within the clay layer, i.e., whether inward or outward flow happens at the top or bottom of the clay layer. If it is downward from the top, it implies that transport of radioisotopes from the Rupel Clay to the surface will be less compared to the diffusion-only scenario. The opposite holds when it is upward to the top. The following situations may give rise to advective flow:

- downward or upward - hydraulic head difference and sufficiently high permeability
- outward – compaction due to ice sheet
- inward – decompaction due to retreat of ice sheet
- downward – chemical osmosis with fresh water on top and saline at the bottom

Wildenborg et al. (2003) showed that glacial periods can cause advective fluxes due to compaction/decompaction: when an ice mass lies on top one may expect compaction and decompaction can be expected following retreat of the ice mass. Upon result, Wildenborg et al. (2003) calculated that temporary groundwater flow up to about 1 mm/year may happen for time period of thousands of years. Such a velocity would thus lead to advective transport of 1 meter in 1000 years in addition to and coupled with the diffusive and also dispersive transport.

The geochemical model analysis focused on inward flow as this may disturb the geochemical characteristics of the Rupel Clay. Two pore water velocities were considered for the advective flow scenarios: 1 and 10 mm/y inward flow. Here, the 1 mm/y scenario serves as reference as this velocity falls within the range calculated by Valstar & Goorden (2016). A few calculations were also made for a scenario with 0.1 mm/y but the results were near-equal to the diffusion-only scenario. These calculations will therefore not be considered any further.

Figure 6.4 shows the concentration profiles for the scenario with advective flux of 1 mm/y and average sediment composition. The depletion of pyrite is again small. The larger influx of water does not cause much additional pyrite oxidation. However, the depletion of calcite is larger than for the diffusion-only scenario. This cannot only be due to carbonate buffering upon pyrite oxidation, because not much additional pyrite oxidation happens. It must, therefore, be due to calcite dissolution in response to cation-exchange and larger inflow of Rhine water having an SI for calcite of 0.14 while the SI was maintained at 0.3 across the profile.

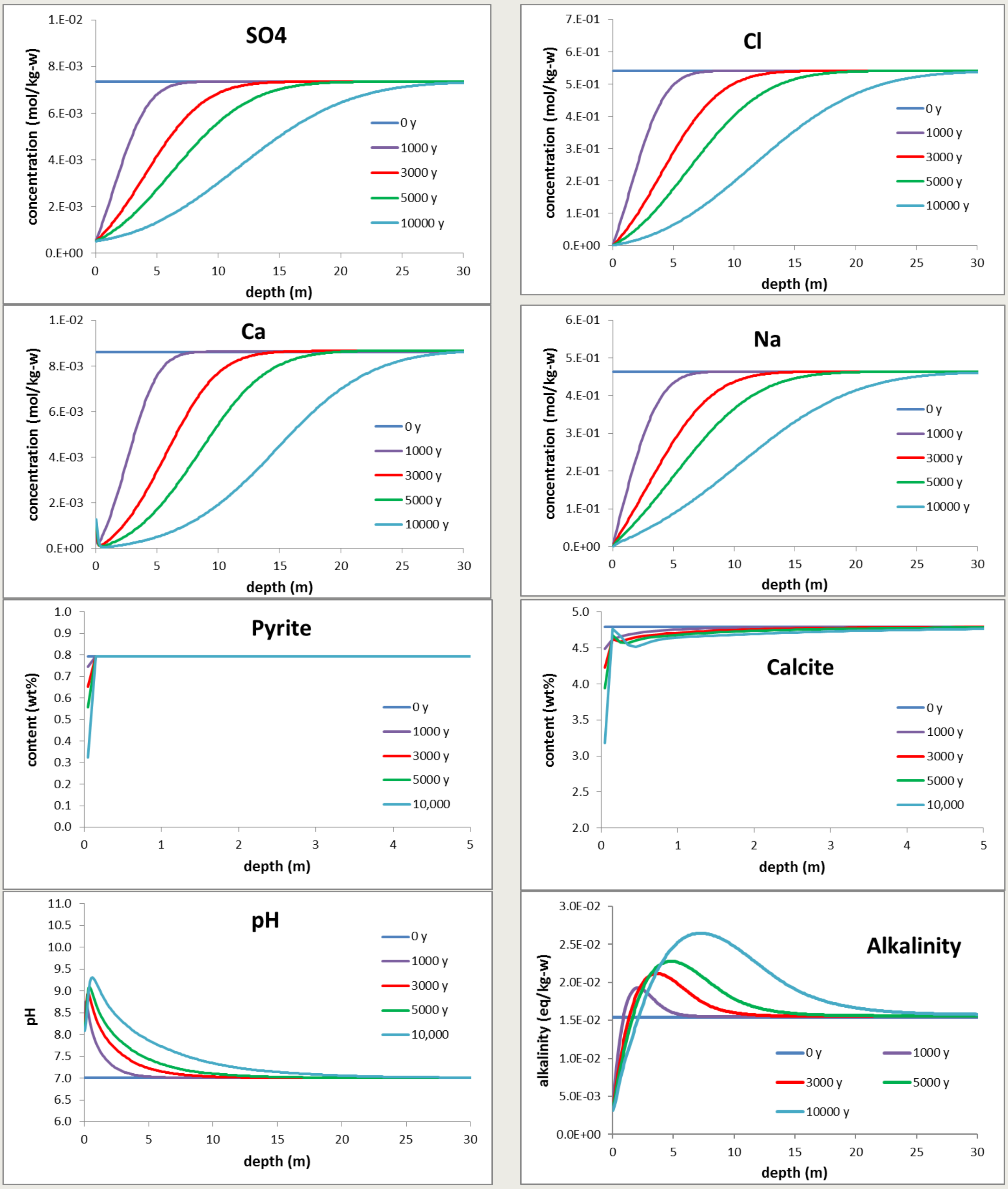

Figure 6.4. Concentration-depth profiles for scenario with 1 mm/y advective inflow of fresh, oxic water in Rupel Clay with anoxic seawater. Note the difference in scale for the x-axes.

The infiltrating fresh groundwater is Ca-rich and the native seawater is Na and Mg rich. Cation-exchange will, therefore, happen among these cations, where equilibrium for calcite is also imposed. The following reactions happen during freshening:

$$Na\text{-}X + \tfrac{1}{2} Ca^{2+} \rightarrow \tfrac{1}{2} Ca\text{-}X_2 + Na^{+}$$

$$CaCO_3 + H_2CO_3^* \leftrightarrow Ca^{2+} + 2\ HCO_3^-$$

The first reaction causes the second reaction to go to the right. This leads to more calcite dissolution than under the diffusion-only scenario. The reaction zone is thus very narrow for advection rate of 1 mm/y as for the diffusion-only scenario. The sediment matrix is thus only affected in a narrow interval at the fringe of the clay layer.

The concentration profiles for the solutes are more S-shaped because of the inflow of fresh water. The penetration depths are also larger: after 10,000 years, the concentration of Cl is half-way between the native and infiltrating concentration is about 12 m where this is 5 m for the diffusion-only scenario. The pore water composition is thus affected to a larger extent than the sediment matrix as result of additional advective transport of the solutes. Figure 6.5 presents the mineral content for the scenario with maximum pyrite and relatively little calcite. The figure shows that calcite becomes exhausted in the first cell within 10,000 y, which makes this zone susceptible for acidification following the calcite leaching but the exhausted zone remains narrow. The Ca-carbonate content may thus be a relevant characteristic with respect to potential acidification but the national, geochemical characterisation suggests that it will often be sufficient (cf. Chapter 2).

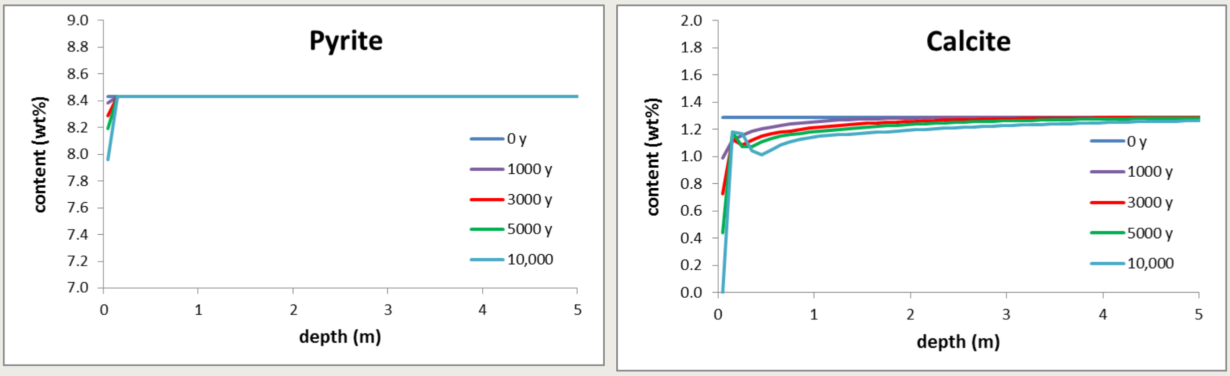

Figure 6.5. Depth profiles of pyrite and calcite contents for scenario with 1 mm/y advective inflow of fresh, oxic water in Rupel Clay with anoxic seawater and maximum pyrite content (Case C of Table 5.1).

Figure 6.6 shows the concentration profiles for the standard scenario with 10 mm/y advection. Such a rate is high and requires boundary conditions that are probably rather extreme. It takes 3000 years to travel 30 m for such an advective flow rate, so originally present pore water will be flushed out of the column within the time period considered. This is illustrated by the concentration profile of Cl and also that of SO_4. The depletion of pyrite is, once more, small so even with a large influx little pyrite gets oxidised because of the limited solubility of oxygen in water. Calcite becomes depleted across a large distance within the clay layer, which is due to calcite dissolution in response to Ca sorption. The concentration profiles for Na show concentrations of several mmol/kg-w or several tens of mmol/kgw, which indicate continuous desorption. The Ca concentration remains below 1 mmol/kgw due to related adsorption. It is striking that for the scenario with maximum pyrite and relatively little calcite, no exhaustion is found in the first cell.

6.2.4. Effects of coverage of exposed clay

In the previous models we only modelled one event of postglacial erosion. However, a cyclic alteration between glacial and interglacial periods can be expected as described by Wildenborg et al. (2003). During the erosion phase of an interglacial period, the clay layer may reach a shallower depth and oxidizing boundary conditions will be present at a shorter distance in the ultimate situation. After this erosion phase, however, the layer will be quickly covered with new sediments. Microbial processes such as sulphate reduction will probably become active in the young sediment which causes relatively fast reduction of the oxygenated layer. This will cause the reestablishment of a covering layer of reduced sediment. With successive glacial cycles, this cycling of erosion and formation of covering layers may repeat itself depending on the areal coverage of the ice sheet and the related depth of erosion.

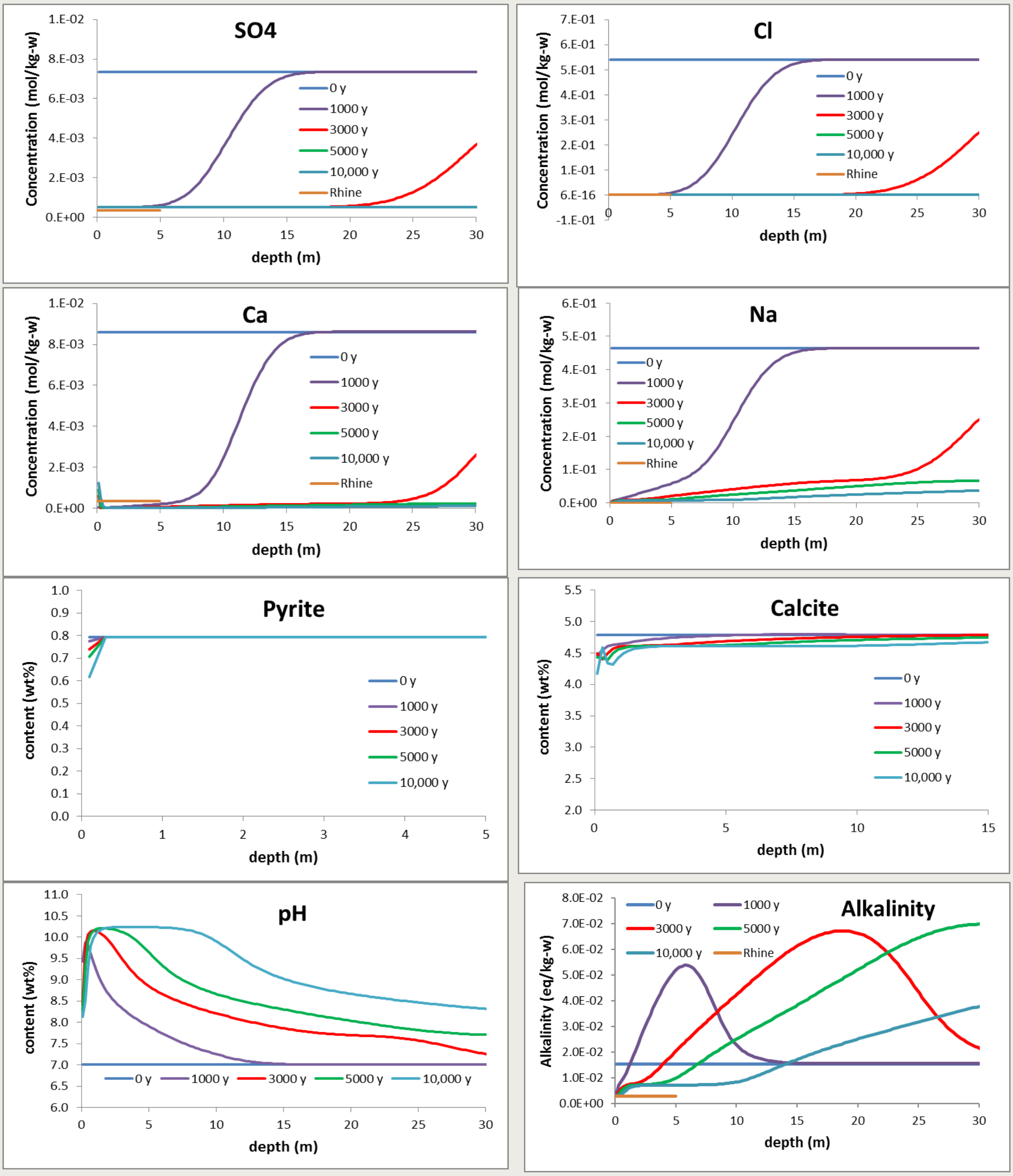

Figure 6.6. Concentration-depth profiles for scenario with 10 mm/y advective inflow of fresh, oxic water in Rupel Clay with anoxic seawater. Note the difference in scale for the x-axes.

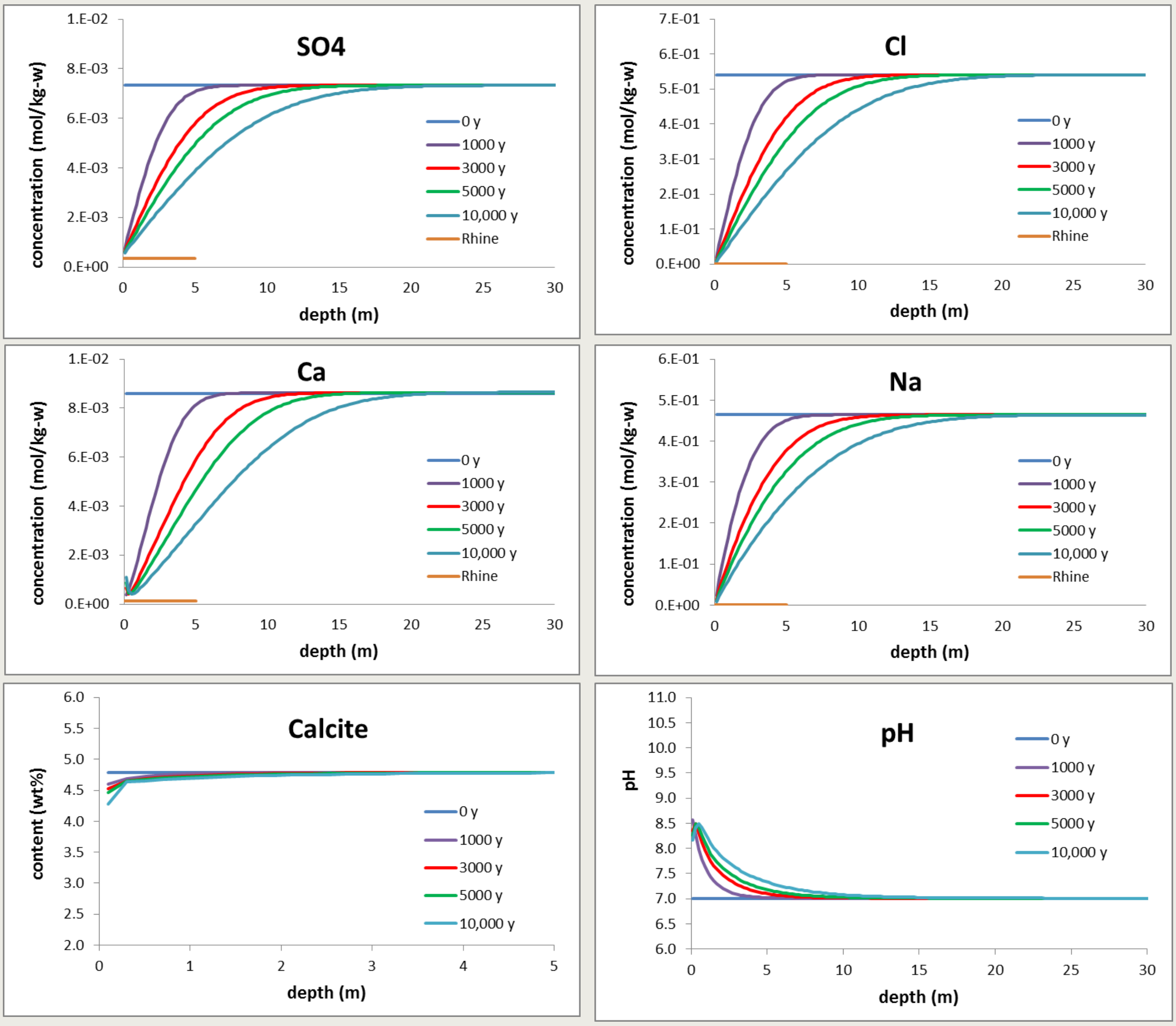

Figure 6.7. Concentration-depth profiles for follow-up scenario of coverage of glacial valley and only diffusion. Note the difference in scale for the x-axes.

The situation was simulated for only-diffusion and 1 mm/y advection with introduction of anoxic seawater on top of the clay layer. The concentration profiles for Cl, SO_4 and Na become a wave which minimum increases in time and moves downward as well (Figure 6.8). The pyrite content remains constant in time as no oxidation can happen due to the anoxic nature of inflowing water and SO_4 thus behaves conservatively. However, the calcite content decreases in time in the first grid cell, which cannot be explained by carbonate buffering upon pyrite oxidation. Infiltration of seawater will induce Ca desorption with Na and also Mg adsorption. The Ca concentration reaches a maximum concentration of about 15 mmol/kgw. This is insufficient to reach saturation for gypsum so precipitation of this mineral cannot happen. One would expect calcite precipitation from this desorption. The opposite must be due to proton buffering of the sediment: the pH goes down again as the anaerobic seawater has a lower pH than river Rhine water. The influx of seawater having a lower pH must induce calcite dissolution.

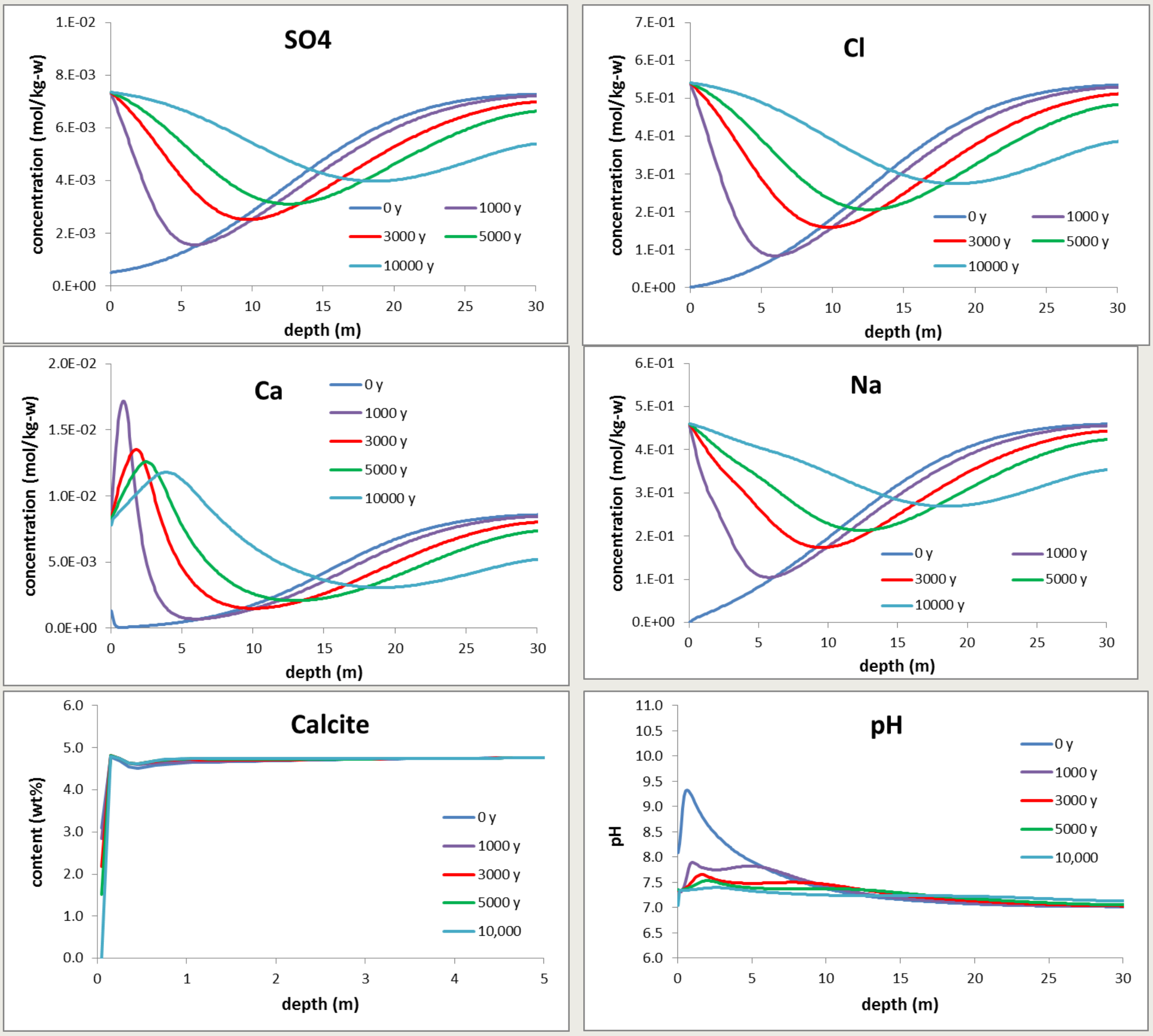

Figure 6.8. Concentration-depth profiles for follow-up scenario of coverage of glacial valley with 1 mm/y advection in addition to diffusion/dispersion. Note the difference in scale for the x-axes.

6.2.5. pH-buffering

The model results indicate that the pH rises above that of the original solutions due to calcite dissolution in a system closed to gaseous CO_2. High pHs are specifically found close to the top of the layer for the scenarios with advection: it rises up to 9-9.5 for 1 mm/y advection and up to 10-10.5 for 10 mm/y. The way in which proton-buffering was modelled is rather simple. Here, the selectivity coefficient for proton sorption was varied as was the fraction of pH-dependent CEC, which influences the pH trajectory at which proton buffering is maximum and the extent of buffering per pH unit. The pH may be an important factor in controlling surface complexation of trace metals, including radioactive ones. It thus deserves better study, where it is also relevant whether any in-situ degradation of sedimentary organic matter happens as this releases CO_2 which lowers the pH and increases the calcite solubility.

6.3.Impact of mine galleries

6.3.1. Background information

De Craen et al. (2008) investigated the effect of oxidation during excavation and ventilation of the Rupel Clay in the disposal galleries in Mol, Belgium. Two different galleries were studied, one after 3 years and the other after 20 years of exposure to oxygen. Pore water compositions and mineralogy were assessed as a function of distance from the gallery (into the Rupel Clay). The results showed pyrite oxidation and calcite dissolution leading to gypsum formation and an increase in cation concentrations in the pore water due to cation exchange. The mineralogy changes were limited to the first few tens of cm into the clay, while the effect on pore water composition was observed up to 1.20 m into the clay. In addition to gypsum, jarosite was observed as a result of pyrite oxidation in the gallery after 3 years of exposure. Jarosite is only stable at a pH below 4. De Craen et al. (2011) concluded from the *absence* of jarosite in the gallery exposed to oxygen for 20 years that the interaction with the concrete lining was significant, resulting in a pH increase with time, whereas the pH is low enough to allow jarosite precipitation in the early stages of exposure.

Vinsot et al. (2014) investigated oxidation in the fractured zone of the underground research laboratory in the Callovian-Oxfordian argillaceous rock in France. They found very similar oxidation reactions, which only occurred in excavation-induced fracture walls or sedimentary elements connected to them by fractures. The rock *matrix* was unaffected by oxidation, implying very low hydraulic conductivity of the pristine rock, in contrast to the permeability of the fracture network.

6.3.2. Modelling approach

The oxidation of the Rupel Clay in the excavation zone might be enhanced by the development of fractures during and after the construction of a geological repository. For the purpose of the assessment of this process, the software TOUGHREACT with the MINC (multiple interacting continua) module was chosen. The MINC module is specifically developed for the purpose of fractured media. It is often used in the field of fractured geothermal reservoirs to investigate the effectiveness of the fluid flow with time.

Fractures are constrained in the MINC module. By selection of the MINC option, a secondary mesh within the primary mesh is generated, subdividing the primary cells into fracture and matrix volume. The matrix volume can be subdivided into several nested grids with increasing distance from the fracture. The fracture parameters required as input are the number of interacting continua, the fracture spacing and fracture volume. Both the double porosity and dual permeability options will be tested. For a diffusion-only system, the maximum time step is limited by the space discretization in order to produce a physically correct solution and should at least respect the Neumann criterion (Marty et al., 2009):

$$N_{\mathrm{eu}} = \frac{2D_{\mathrm{p}}\Delta t}{\Delta x^2} \leqslant 1$$

Where D_p is the pore diffusion coefficient. Based on the smallest grid size at the left side of the mesh of ~0.007 m, tortuosity of 0.1 and a bulk diffusion coefficient of 1E-9 m/s, the maximum time step is 1E5 s (= 1.16 days). In our model we use a fracture volume of 0.1, which means that Δx_{min} is in fact 0.0007 m and Δt_{max} 10,000 s (= 2,78 hours).

A radial model was chosen to represent the circular tunnel shape of the galleries. The initial model is a single layer radial model of 15 cells with a total length of 6 m. The grid sizes decrease in size towards the left side of the column, representing the boundary with the gallery (Figure 6.9). Then a multi-layer model is developed with 10 layers in the Z-direction to assess the effect of connected fractures (Figure 6.10).

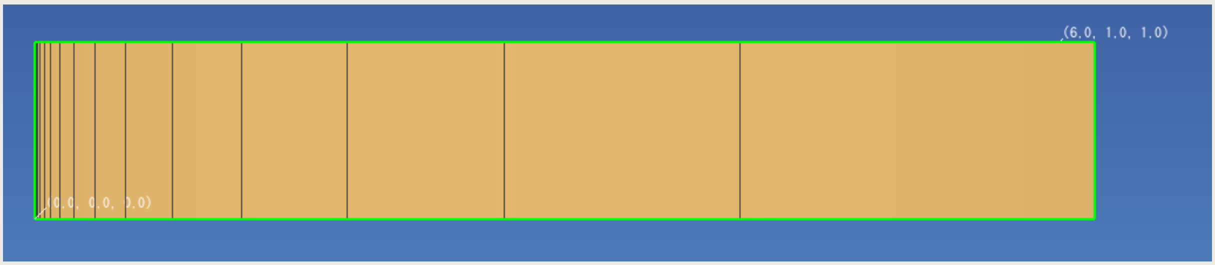

Figure 6.9. Mesh of 1D radial model.

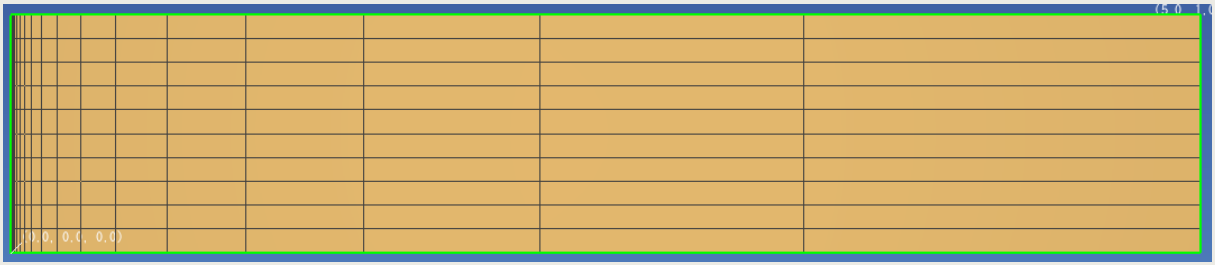

Figure 6.10. Mesh of 2D radial model.

At the time of fracture formation, the fractures will be water saturated. The atmospheric pressure inside the repository is too low for air to penetrate the fractures as long as they are water saturated. Instead, oxygen will dissolve into the pore water and diffuse through the Rupel Clay. Diffusion will be faster through the fractures with high porosity and low tortuosity than in the clay matrix. This allows the modelled system to be represented by one fluid phase, liquid water. Oxygen is included as dissolved species and will only migrate by means of diffusion. We ignore the potential, slow advection of water from the clay towards the gallery. Since permeability values of porous media only affect fluid flow, and not diffusion of species in the aqueous phase, permeability values for the clay matrix and fractures are irrelevant.

The initial pore water composition used in the TOUGHREACT model follows the methodology as explained before. The pore water in the left grid cell is equilibrated with an oxygen partial pressure of the atmosphere. In order to have a constant supply of dissolved oxygen, the composition of this cell is fixed. The pressure in the total mesh is atmospheric pressure. The fractures have a porosity of 0.5 and a tortuosity factor of 0.8. Permeability values are irrelevant in a diffusion-only system. The fracture spacing is set at 0.1m in x, y and z-direction (3D fracture pattern), with a volume of 0.1 (10 vol% of the Rupel Clay is made up of fracture).

The mineral composition used in the TOUGHREACT model corresponds to Case A in Table 5.1. Only the fast reacting minerals are allowed to react, considering the short time frame, in order to speed up the simulations: pyrite, hematite, calcite, dolomite. In previous chapters, equilibrium for goethite instead of magnetite was assumed. Goethite is more soluble; this difference will have little implications as both are highly insoluble under oxic conditions and near-neutral pH. In the 1D model, the minerals are included as equilibrium phases. Pyrite oxidation kinetics becomes important if sufficient gaseous oxygen supply is available. Xu et al (2000) reported on two types of pyrite oxidation mechanisms: one by O_2 and one by iron oxidation followed by pyrite oxidation through oxidized iron. The latter is highly accelerated in the presence of specific catalyzing bacteria. In this study we assume the absence of bacteria and we apply a pyrite oxidation rate of 1×10^{-10} mol $m^{-2}s^{-1}$. Note that we neglect the impact of the cementitious material from which the liner of the mine gallery is made. This is the research topic in the next chapter. The current chapter focusses on whether oxygen penetration and oxidation are enhanced by fractures in the clay. In chapter 6.2 we demonstrated that oxidation under diffusion and/or advection conditions through the bulk clay in absence of fractures is slow.

6.3.3. Results

The results from the 1D model show complete pyrite oxidation, dissolution of calcite and formation of hematite in the first 5 cm of the fracture after 100 years (Fig. 6.11 and 6.12). As a consequence, the porosity and sulphate concentration slightly increased with a corresponding minor decrease in pH. In the matrix of the Rupel Clay, the pyrite oxidation and corresponding calcite dissolution are negligible.

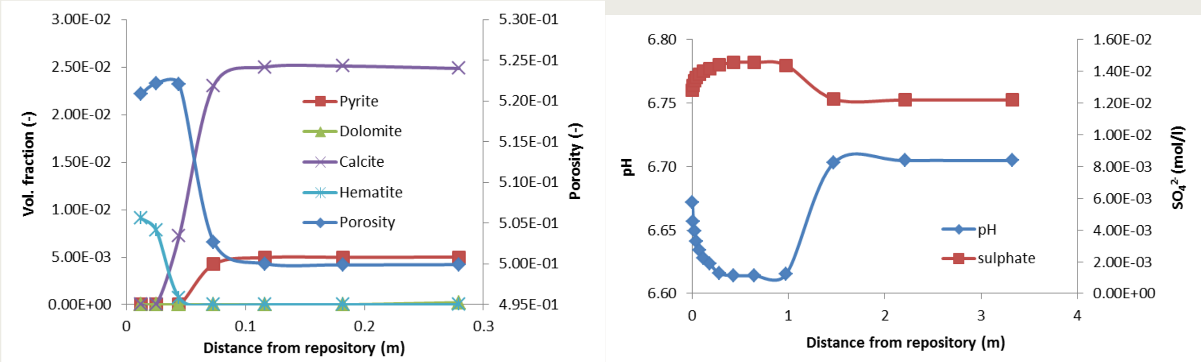

Figure 6.11. Mineralogy, porosity, pH and sulphate concentration after 100 years in the fracture zone with distance from the mine gallery.

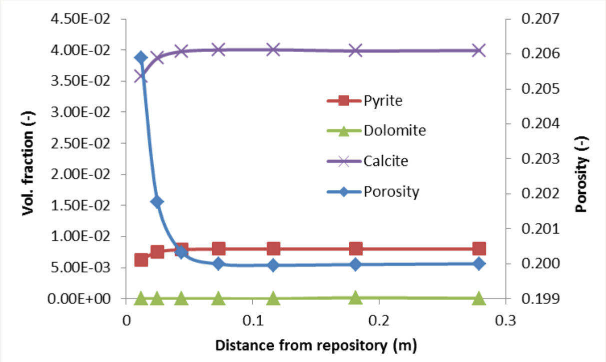

Figure 6.12. Mineralogy, porosity, pH and sulphate concentration after 100 years in the matrix zone with distance from the mine gallery. Note that the initial porosity of the matrix is 0.2, whereas it is 0.5 in the fractures.

The 2D model was used to evaluate the effect of potential sandy layers within the Rupel Clay. Both a homogeneous Rupel Clay, and a model with a sandy layer were run. The sandy layer is included in the model to assess the effect of enhanced oxygen diffusion. In addition, the number of interacting continua is increased from 2 to 4; i.e. the matrix volume is now divided into 3 nested grids (see section 6.3.2). In the northern part of the Netherlands, the porosity of the sandy mud layers is ~25%, whereas in the southern area the porosity is ~50% (Vis and Verweij, 2014). The results from the 2D homogeneous model show a pH decrease surrounding the oxygen source. Although the effect of oxygen on pH spreads further than pyrite oxidation, calcite dissolution and corresponding porosity decrease (Fig. 6.13), the pH decrease is still very limited. The effect of enhanced diffusion through the sand layer is negligible (Fig. 6.14).

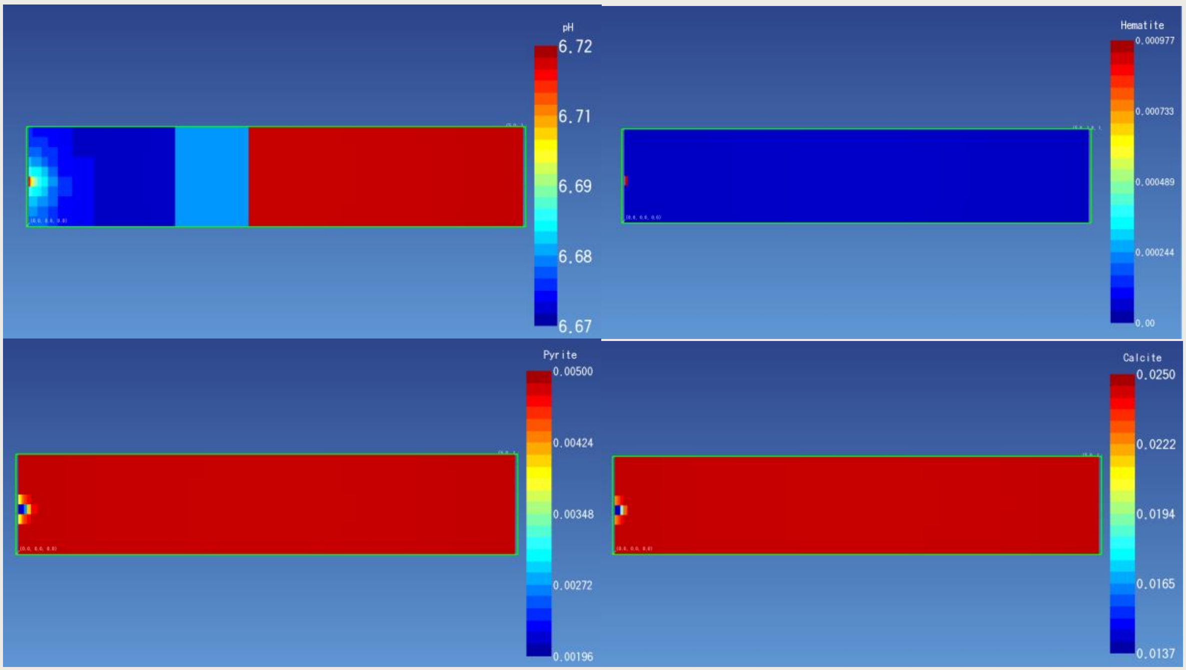

Figure 6.13. 2D model results for homogeneous clay formation after 100 years of oxygen diffusion. Scale: 5 by 1 m.

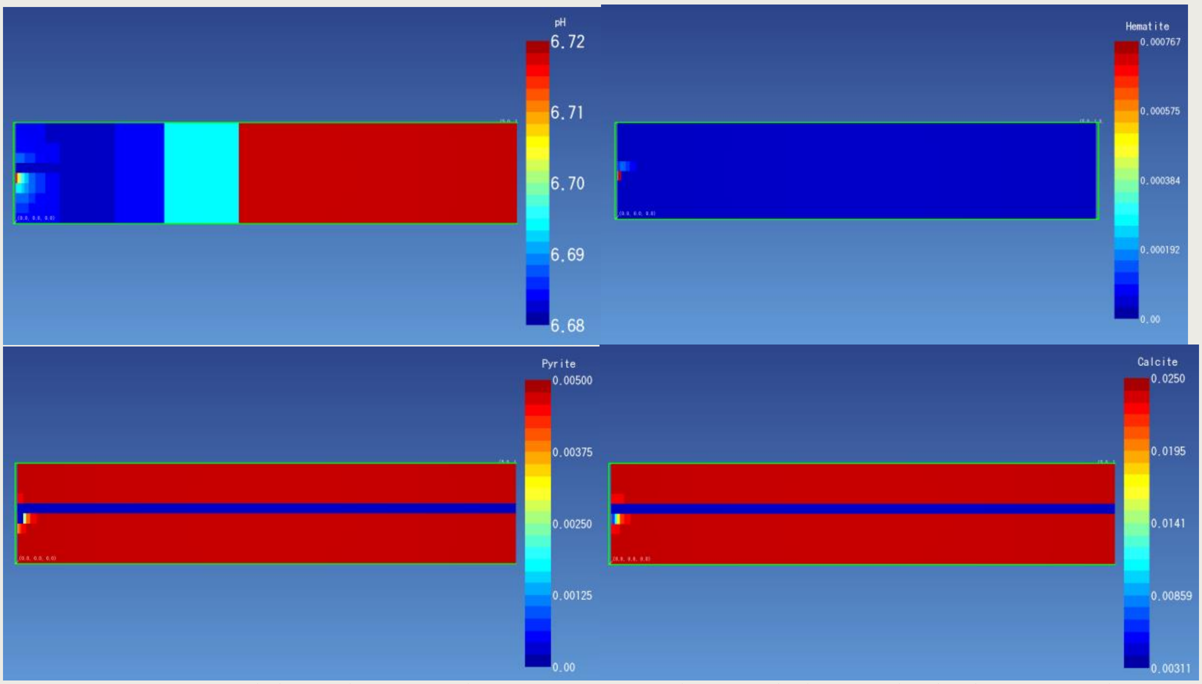

Figure 6.14. 2D model results for a clay formation with a sandy layer (the high porosity layer in the middle) after 100 years of oxygen diffusion. Scale: 5 by 1 m.

6.4. Conclusions

Model studies provide quantitative information on the potential effects of oxidation and freshening/salinisation on the relevant characteristics of the Rupel Clay. The results suggest that the reaction zones stay limited to a few dm but reaction products get transported several meters or tens of meters away depending on advection in addition to diffusion. It must be realised that this all holds as long as the clay layer remains water saturated. An entirely different situation arises when cracks are present that enable aeration of the anaerobic clay, which was not considered.

7. Geochemical processes at the Rupel Clay – EBS interface

This chapter describes the results on the expected development of chemical conditions at the EBS – clay interface over longer time scales, as far as relevant for the macro chemistry of the clay. The development of these local chemical conditions is driven by the contrasting chemical compositions of the EBS material on one hand, and the Rupel Clay on the other hand. These different conditions and the resulting chemical/physical interactions determine the development of local chemical and physical conditions over time in the EBS-Clay interface. These local conditions depend on:

- Amounts and chemical character of the EBS degradation products (of which an overview and quantitative model will be defined in OPERA WP 5.1)
- The chemical and physical properties of the EBS as present at the clay interface (as studied in OPERA Task 5.1.4)
- The chemical and physical properties of the Rupel Clay (subject of task 5.2.1).
- The re-saturation behaviour,
- Interactions between EBS material and Rupel Clay via diffusion.

7.1. Chemical characterisation

7.1.1. Chemical characteristics of the EBS material

The main material of the EBS that is in direct contact with the surrounding clay material from the time the EBS is constructed, is the structural concrete of the galleries. According to the suggested composition (Verhoef, 2014) this will be a Portland cement concrete type with fly ash and quartz aggregates.

Table 7.1. Suggested composition of EBS structural concrete material.

Component/parameter		Type	
Cement	CEM II/A to B-(V)	386	kg m-3
Water	125		kg m-3
Plasticiser	Woermann BV 514	1.33	kg m-3
Superplasticiser	Woermann FM 30	3.65	kg m-3
Fine aggregate	quartz sand: 0-2 mm	615	kg m-3
Coarse aggregate	quartz gravel: 2-8 mm	612	kg m-3
Coarse aggregate	quartz gravel: 8-16 mm	700	kg m-3
w/c	Property		0.39

Apart from the structural cementitious material, another important fraction of the total mass of repository is the non-structural cementitious material present in the cemented waste, supercontainers and backfill material. However because this material will not be in direct contact with the clay, the main interaction between EBS and clay will be via the structural cement/ concrete material (Meeussen & Rosca-Bocancea, 2014).

An overview of the estimated degradation products of the cementitious EBS materials is provided in OPERA report OPERA-PU-SCK514 (Jacques and Seetharam, 2015).

The main interface material present in the EBS is the structural concrete described in their paragraph 2.1 and table 2-1. For these types of materials the general porosity is within the range of 10-15%. Regarding the bulk composition with respect to alkalinity, this will be predominantly present in the CaO (Portlandite) fraction of the cement, which amounts to 60% of 380 kg which is equivalent to ca. 230 kg CaO, or ca. 4000 mol/m3 or 8000 mol OH-.

These numbers are in agreement with estimations made in SCK514 (Jacques and Seetharam, 2015).

7.1.2. Chemical stability calculations for macro elements Fe, S and Ca

To evaluate whether the thermodynamic equilibrium model that will be used for the reactive transport calculations is able to describe/predict the macro chemistry of the Rupel clay we have performed stability calculations with this model for a range of pH-pe conditions. These calculations show the predominant chemical forms of each macro element as a function of pH and pe. The pH-pe values as measured in Belgian Boom Clay pore water are indicated with the data point (grey box) in the diagrams. In these calculations the pH and pe are given as input values, and in this way it is possible to cover a wide range of conditions. This range of conditions is much larger than would be possible in the real material, and only intended to illustrate the stability ranges for different minerals/forms. In reality it is not straightforward, or even possible to vary pH and pe independently as these parameters are correlated by different chemical reactions.

For sulfur we can see that the measured data point is located at the boundary of the regions where sulfur is predominantly oxidized (gypsum) and reduced (pyrite). In practice this means that redox conditions are likely to be buffered by dissolution/oxidation of pyrite. For iron we can also see that the measured pH/pe conditions are at the boundary of two regions, in this case the pyrite and siderite dominated regions. In the diagram for calcium we can see that measured Boom Clay conditions are located at the boundary between calcite and gypsum. This implies that under these conditions calcite, may coexist with gypsum. The results should be interpreted carefully as they assume thermodynamic equilibrium for all reactions in the model which in reality rarely is the case, especially for redox reactions. However, the fact that the thermodynamic model, based on equilibrium with calcite, gypsum, pyrite and siderite predicts pH/pe ranges very similar to observed values suggests that this model can be used to simulate the reactive transport in Rupel Clay. The following graphs show the macro elements and the chemical reactions that were taken into account in the Rupel Clay equilibrium simulations.

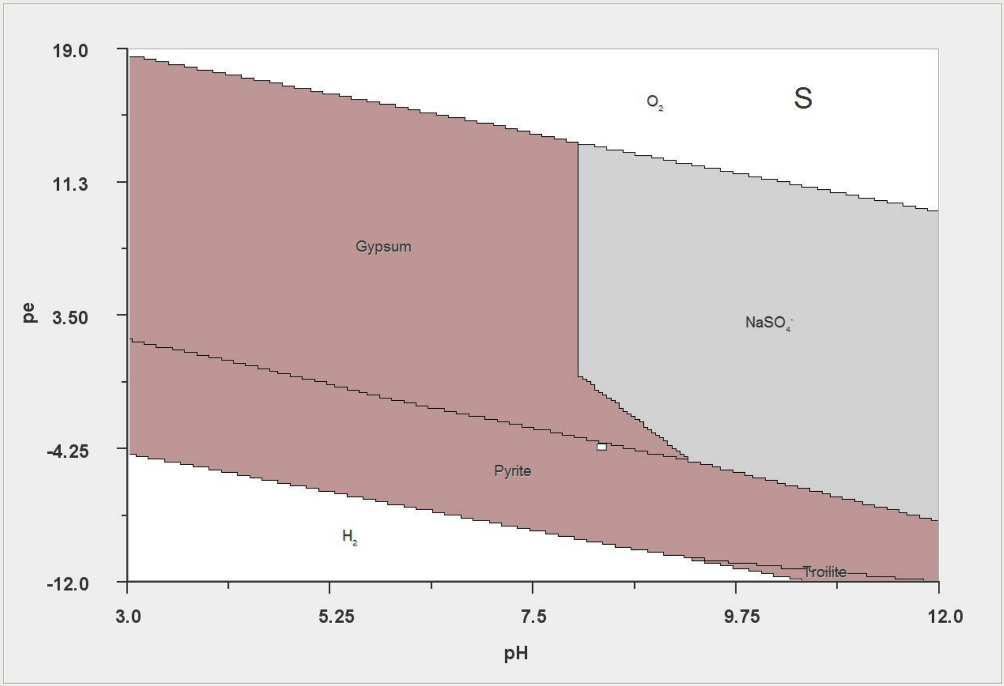

Figure 7.1. Stability diagram for Sulfur with Boom Clay conditions in Belgium (Table 7-2, Mol) indicated by data point.

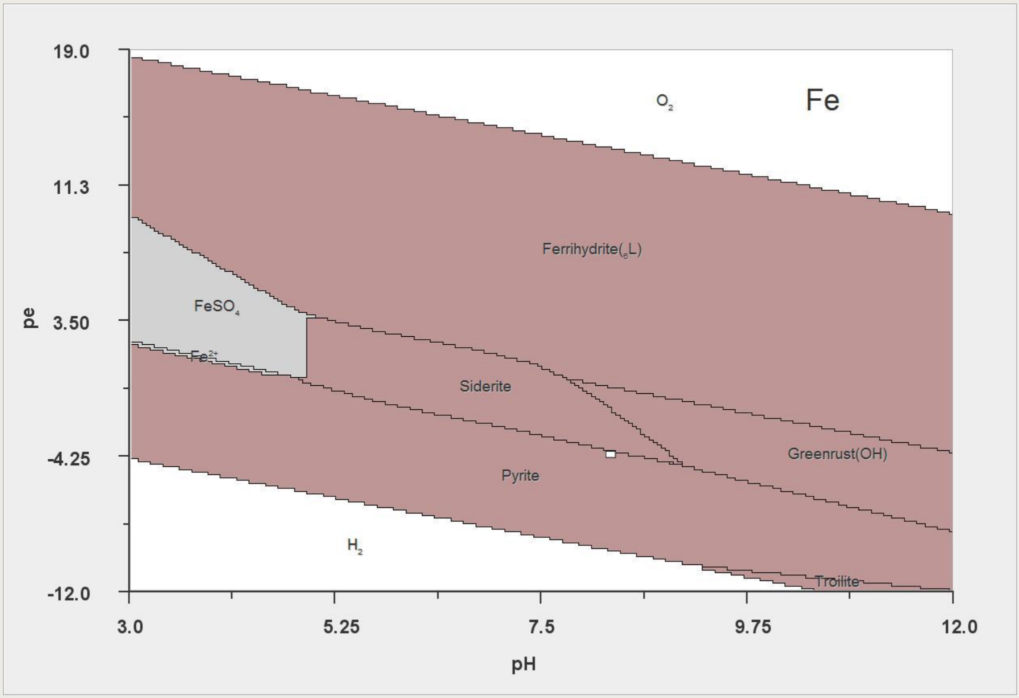

Figure 7.2. Stability diagram for Iron with Boom Clay conditions in Belgium (Table 7-2, Mol) indicated by data point

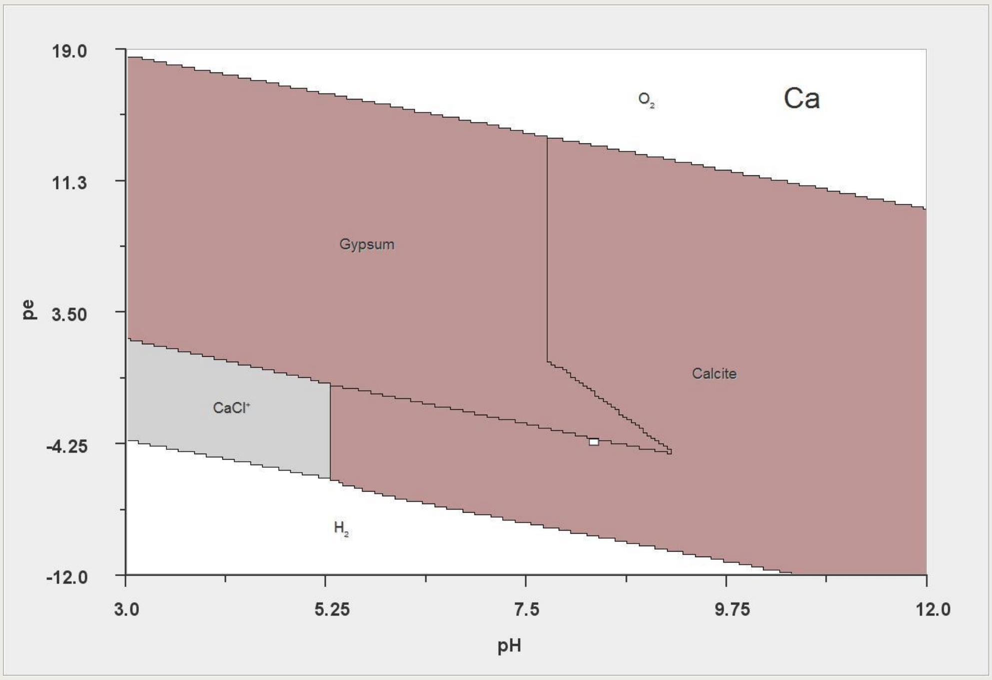

Figure 7.3. Stability diagram for Ca with Boom Clay conditions (Table 7-2, Mol) indicated by data point.

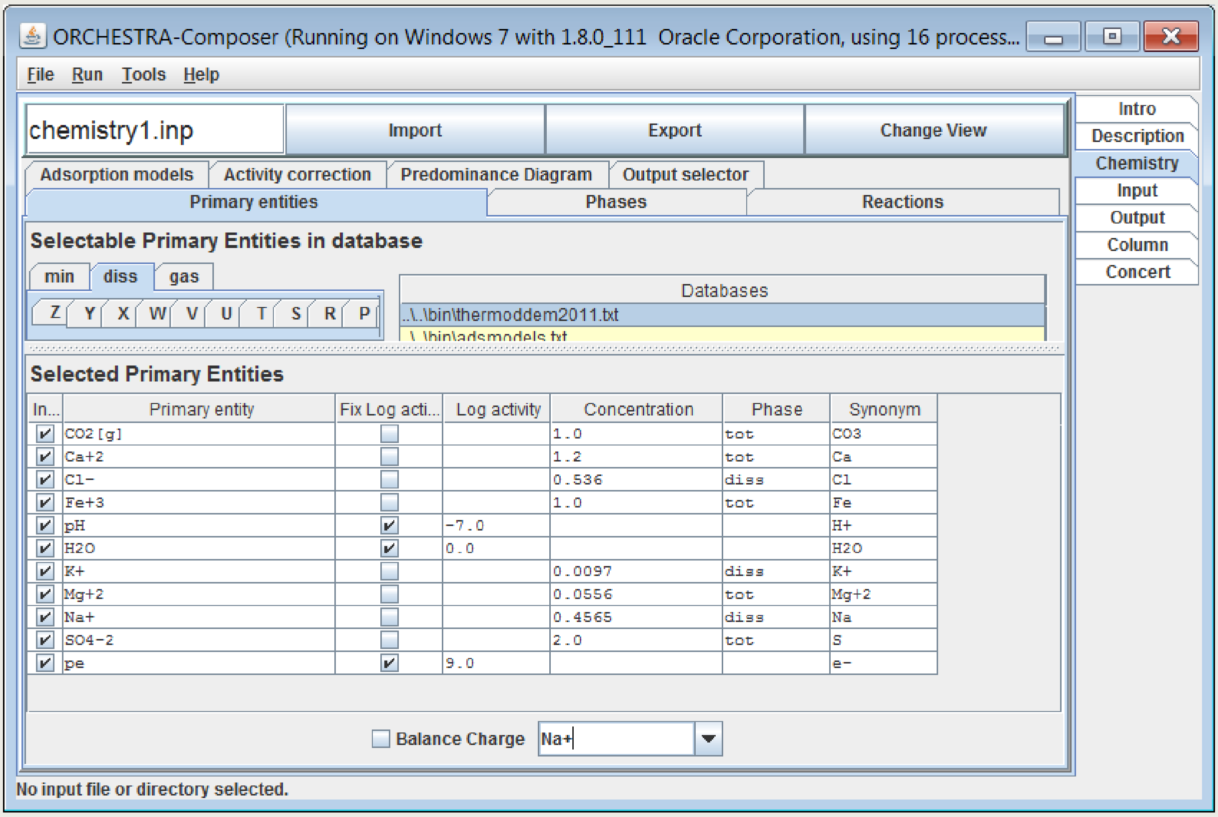

chemistry1.inp

Selectable Primary Entities in database

Databases

..\..\bin\thermoddem2011.txt

..\..\bin\adsmodels.txt

Selected Primary Entities

In...	Primary entity	Fix Log acti...	Log activity	Concentration	Phase	Synonym
☑	CO2 [g]	☐		1.0	tot	CO3
☑	Ca+2	☐		1.2	tot	Ca
☑	Cl-	☐		0.536	diss	Cl
☑	Fe+3	☐		1.0	tot	Fe
☑	pH	☑	-7.0			H+
☑	H2O	☑	0.0			H2O
☑	K+	☐		0.0097	diss	K+
☑	Mg+2	☐		0.0556	tot	Mg+2
☑	Na+	☐		0.4565	diss	Na
☑	SO4-2	☐		2.0	tot	S
☑	pe	☑	9.0			e-

☐ Balance Charge Na+

No input file or directory selected.

Figure 7.4. Primary entity settings used in the predominance calculations.

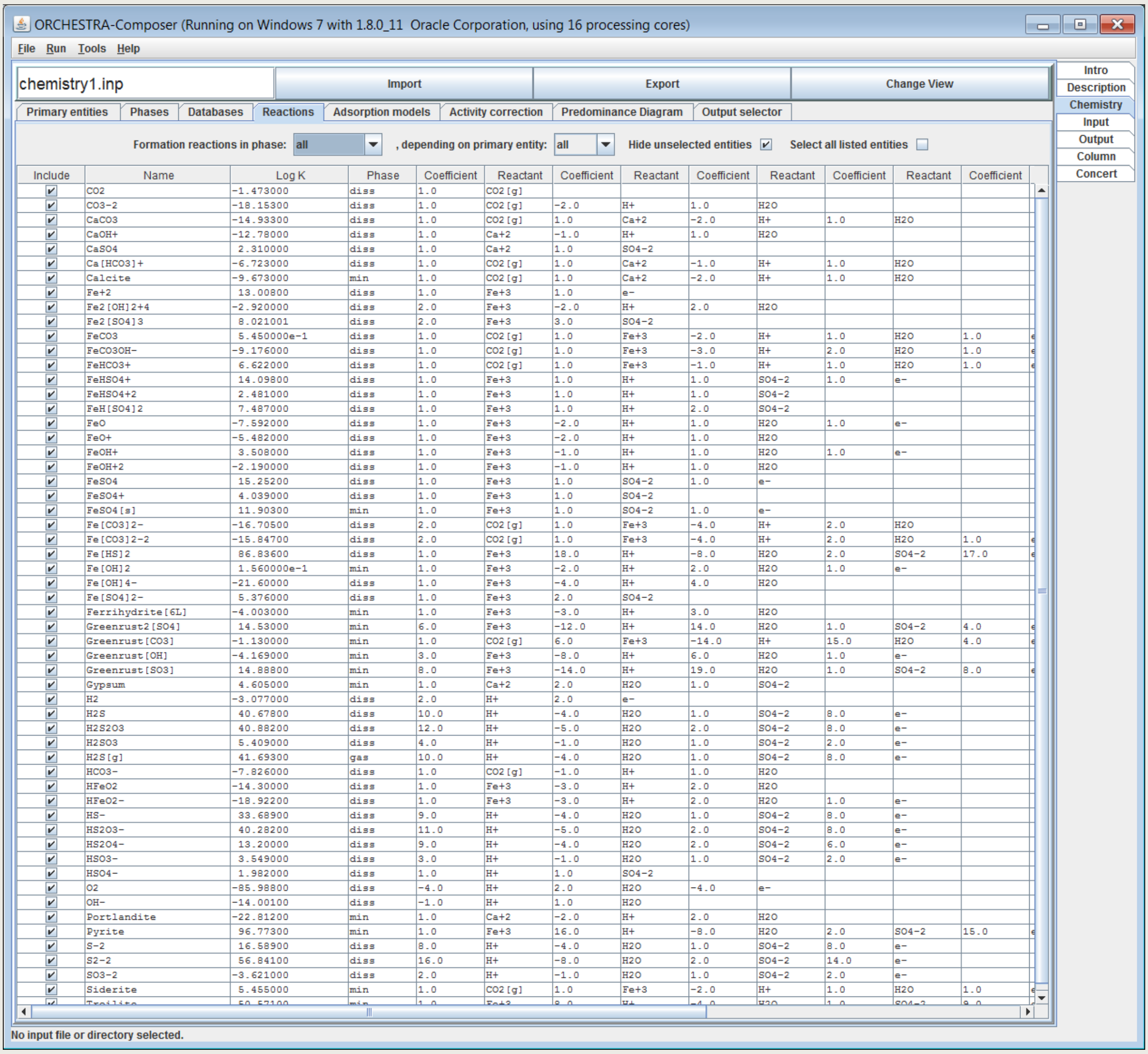

Formation reactions in phase: all , depending on primary entity: all Hide unselected entities ☑ Select all listed entities ☐

Include	Name	Log K	Phase	Coefficient	Reactant	Coefficient	Reactant	Coefficient	Reactant	Coefficient	Reactant	Coefficient
☑	CO2	-1.473000	diss	1.0	CO2[g]							
☑	CO3-2	-18.15300	diss	1.0	CO2[g]	-2.0	H+	1.0	H2O			
☑	CaCO3	-14.93300	diss	1.0	CO2[g]	1.0	Ca+2	-2.0	H+	1.0	H2O	
☑	CaOH+	-12.78000	diss	1.0	Ca+2	-1.0	H+	1.0	H2O			
☑	CaSO4	2.310000	diss	1.0	Ca+2	1.0	SO4-2					
☑	Ca[HCO3]+	-6.723000	diss	1.0	CO2[g]	1.0	Ca+2	-1.0	H+	1.0	H2O	
☑	Calcite	-9.673000	min	1.0	CO2[g]	1.0	Ca+2	-2.0	H+	1.0	H2O	
☑	Fe+2	13.00800	diss	1.0	Fe+3	1.0	e-					
☑	Fe2[OH]2+4	-2.920000	diss	2.0	Fe+3	-2.0	H+	2.0	H2O			
☑	Fe2[SO4]3	8.021001	diss	2.0	Fe+3	3.0	SO4-2					
☑	FeCO3	5.450000e-1	diss	1.0	CO2[g]	1.0	Fe+3	-2.0	H+	1.0	H2O	1.0
☑	FeCO3OH-	-9.176000	diss	1.0	CO2[g]	1.0	Fe+3	-3.0	H+	2.0	H2O	1.0
☑	FeHCO3+	6.622000	diss	1.0	CO2[g]	1.0	Fe+3	-1.0	H+	1.0	H2O	1.0
☑	FeHSO4+	14.09800	diss	1.0	Fe+3	1.0	H+	1.0	SO4-2	1.0	e-	
☑	FeHSO4+2	2.481000	diss	1.0	Fe+3	1.0	H+	1.0	SO4-2			
☑	FeH[SO4]2	7.487000	diss	1.0	Fe+3	1.0	H+	2.0	SO4-2			
☑	FeO	-7.592000	diss	1.0	Fe+3	-2.0	H+	1.0	H2O	1.0	e-	
☑	FeO+	-5.482000	diss	1.0	Fe+3	-2.0	H+	1.0	H2O			
☑	FeOH+	3.508000	diss	1.0	Fe+3	-1.0	H+	1.0	H2O	1.0	e-	
☑	FeOH+2	-2.190000	diss	1.0	Fe+3	-1.0	H+	1.0	H2O			
☑	FeSO4	15.25200	diss	1.0	Fe+3	1.0	SO4-2	1.0	e-			
☑	FeSO4+	4.039000	diss	1.0	Fe+3	1.0	SO4-2					
☑	FeSO4[s]	11.90300	min	1.0	Fe+3	1.0	SO4-2	1.0	e-			
☑	Fe[CO3]2-	-16.70500	diss	2.0	CO2[g]	1.0	Fe+3	-4.0	H+	2.0	H2O	
☑	Fe[CO3]2-2	-15.84700	diss	2.0	CO2[g]	1.0	Fe+3	-4.0	H+	2.0	H2O	1.0
☑	Fe[HS]2	86.83600	diss	1.0	Fe+3	18.0	H+	-8.0	H2O	2.0	SO4-2	17.0
☑	Fe[OH]2	1.560000e-1	min	1.0	Fe+3	-2.0	H+	2.0	H2O	1.0	e-	
☑	Fe[OH]4-	-21.60000	diss	1.0	Fe+3	-4.0	H+	4.0	H2O			
☑	Fe[SO4]2-	5.376000	diss	1.0	Fe+3	2.0	SO4-2					
☑	Ferrihydrite[6L]	-4.003000	min	1.0	Fe+3	-3.0	H+	3.0	H2O			
☑	Greenrust2[SO4]	14.53000	min	6.0	Fe+3	-12.0	H+	14.0	H2O	1.0	SO4-2	4.0
☑	Greenrust[CO3]	-1.130000	min	1.0	CO2[g]	6.0	Fe+3	-14.0	H+	15.0	H2O	4.0
☑	Greenrust[OH]	-4.169000	min	3.0	Fe+3	-8.0	H+	6.0	H2O	1.0	e-	
☑	Greenrust[SO3]	14.88800	min	8.0	Fe+3	-14.0	H+	19.0	H2O	1.0	SO4-2	8.0
☑	Gypsum	4.605000	min	1.0	Ca+2	2.0	H2O	1.0	SO4-2			
☑	H2	-3.077000	diss	2.0	H+	2.0	e-					
☑	H2S	40.67800	diss	10.0	H+	-4.0	H2O	1.0	SO4-2	8.0	e-	
☑	H2S2O3	40.88200	diss	12.0	H+	-5.0	H2O	2.0	SO4-2	8.0	e-	
☑	H2SO3	5.409000	diss	4.0	H+	-1.0	H2O	1.0	SO4-2	2.0	e-	
☑	H2S[g]	41.69300	gas	10.0	H+	-4.0	H2O	1.0	SO4-2	8.0	e-	
☑	HCO3-	-7.826000	diss	1.0	CO2[g]	-1.0	H+	1.0	H2O			
☑	HFeO2	-14.30000	diss	1.0	Fe+3	-3.0	H+	2.0	H2O			
☑	HFeO2-	-18.92200	diss	1.0	Fe+3	-3.0	H+	2.0	H2O	1.0	e-	
☑	HS-	33.68900	diss	9.0	H+	-4.0	H2O	1.0	SO4-2	8.0	e-	
☑	HS2O3-	40.28200	diss	11.0	H+	-5.0	H2O	2.0	SO4-2	8.0	e-	
☑	HS2O4-	13.20000	diss	9.0	H+	-4.0	H2O	2.0	SO4-2	6.0	e-	
☑	HSO3-	3.549000	diss	3.0	H+	-1.0	H2O	1.0	SO4-2	2.0	e-	
☑	HSO4-	1.982000	diss	1.0	H+	1.0	SO4-2					
☑	O2	-85.98800	diss	-4.0	H+	2.0	H2O	-4.0	e-			
☑	OH-	-14.00100	diss	-1.0	H+	1.0	H2O					
☑	Portlandite	-22.81200	min	1.0	Ca+2	-2.0	H+	2.0	H2O			
☑	Pyrite	96.77300	min	1.0	Fe+3	16.0	H+	-8.0	H2O	2.0	SO4-2	15.0
☑	S-2	16.58900	diss	8.0	H+	-4.0	H2O	1.0	SO4-2	8.0	e-	
☑	S2-2	56.84100	diss	16.0	H+	-8.0	H2O	2.0	SO4-2	14.0	e-	
☑	SO3-2	-3.621000	diss	2.0	H+	-1.0	H2O	1.0	SO4-2	2.0	e-	
☑	Siderite	5.455000	min	1.0	CO2[g]	1.0	Fe+3	-2.0	H+	1.0	H2O	1.0

No input file or directory selected.

Figure 7.5. Reactions taken into account in stability calculations.

7.2. Model of EBS-Rupel Clay interaction

7.2.1. Description of EBS - Clay boundary

The boundary between the projected EBS and the surrounding Rupel clay was in the modelling assumed to consist of a concrete layer of 0.5 m thickness in contact with a Rupel Clay layer of 25 m thickness. Both, the concrete and the clay layer each have their own initial chemical composition and physical properties. Local concentrations of dissolved and mineral phases are governed by a set of reactions that are assumed to be in thermodynamic equilibrium. So no kinetic constraints were taken into account. Contact via the two zones was assumed to take place via transport of dissolved ions in the water filled pores. Cement chemical and physical properties are estimated based on data on the type of cementitious material that will be used in the EBS. To evaluate possible effects of water flow, also simulations are performed that include advection as transport process.

7.2.2. Description of the geochemical model of the concrete zone

Concrete consists of a porous mixture of water, cement and aggregate materials. The reactive transport model includes a geochemical model that calculates the distribution of elements over the solid particle phases and the aqueous phase in the pore space. The element fractions present in the different solid phase are assumed to be immobile, while the fraction in the aqueous phase is assumed to migrate via diffusion or advection. The geochemical models consist of a set of mineral precipitation-dissolution reactions and a number of solid solutions and aqueous complexation reactions. The amount of elements present in the cement phase is assumed to be effectively in equilibrium with the solution over the simulation time period, while the material in the aggregates is assumed to be inert. This assumption seems reasonable because aggregates contain considerable mass but have a low surface area. Precipitation-dissolution reactions may result in a change of the pore space. These changes are not takes into account in the model.

7.2.3. Chemical reactions taken into account

For the total zone (concrete + clay) a set of chemical equilibrium reactions is taken into account. The difference between concrete and clay is characterized by the different total amounts of elements, different initial pH and redox potential and different amounts of adsorptive surfaces. This results in very different local chemical conditions in the concrete and the clay layer and this in turn determines which precipitation reactions or mineral will be relevant. For example, a set of cement mineral precipitation reactions is included, consisting of pure minerals and solid solutions, originating from the work of Matschei (2007). These minerals will be stable under the chemical conditions in the concrete layer. In Figure 7.6 the set of precipitation reactions is shown, the full set of equilibrium reactions taken into account is listed in Appendix 2.

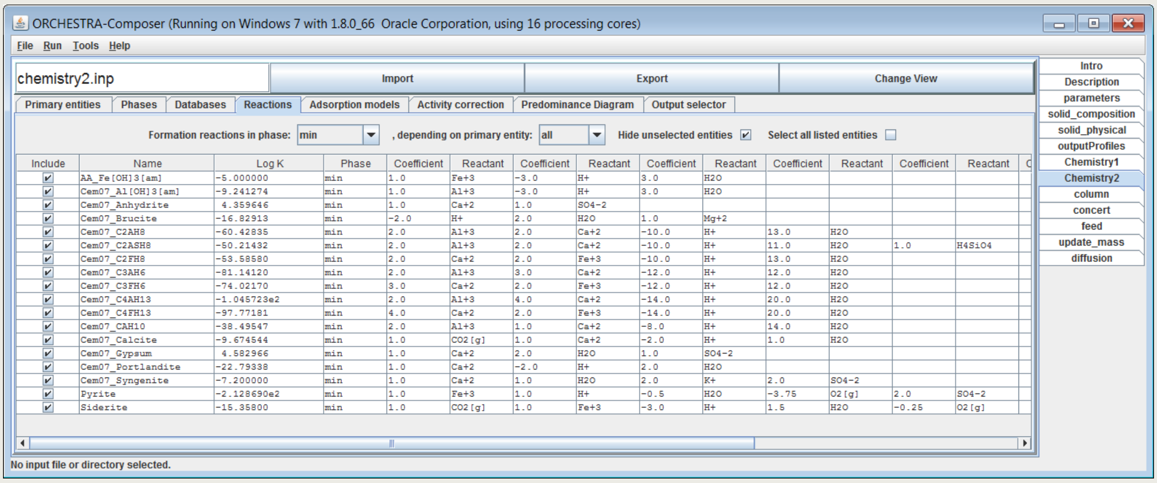

chemistry2.inp

Formation reactions in phase: min , depending on primary entity: all Hide unselected entities ☑ Select all listed entities ☐

Include	Name	Log K	Phase	Coefficient	Reactant	Coefficient	Reactant	Coefficient	Reactant	Coefficient	Reactant	Coefficient	Reactant
☑	AA_Fe[OH]3[am]	-5.000000	min	1.0	Fe+3	-3.0	H+	3.0	H2O				
☑	Cem07_Al[OH]3[am]	-9.241274	min	1.0	Al+3	-3.0	H+	3.0	H2O				
☑	Cem07_Anhydrite	4.359646	min	1.0	Ca+2	1.0	SO4-2						
☑	Cem07_Brucite	-16.82913	min	-2.0	H+	2.0	H2O	1.0	Mg+2				
☑	Cem07_C2AH8	-60.42835	min	2.0	Al+3	2.0	Ca+2	-10.0	H+	13.0	H2O		
☑	Cem07_C2ASH8	-50.21432	min	2.0	Al+3	2.0	Ca+2	-10.0	H+	11.0	H2O	1.0	H4SiO4
☑	Cem07_C2FH8	-53.58580	min	2.0	Ca+2	2.0	Fe+3	-10.0	H+	13.0	H2O		
☑	Cem07_C3AH6	-81.14120	min	2.0	Al+3	3.0	Ca+2	-12.0	H+	12.0	H2O		
☑	Cem07_C3FH6	-74.02170	min	3.0	Ca+2	2.0	Fe+3	-12.0	H+	12.0	H2O		
☑	Cem07_C4AH13	-1.045723e2	min	2.0	Al+3	4.0	Ca+2	-14.0	H+	20.0	H2O		
☑	Cem07_C4FH13	-97.77181	min	4.0	Ca+2	2.0	Fe+3	-14.0	H+	20.0	H2O		
☑	Cem07_CAH10	-38.49547	min	2.0	Al+3	1.0	Ca+2	-8.0	H+	14.0	H2O		
☑	Cem07_Calcite	-9.674544	min	1.0	CO2[g]	1.0	Ca+2	-2.0	H+	1.0	H2O		
☑	Cem07_Gypsum	4.582966	min	1.0	Ca+2	2.0	H2O	1.0	SO4-2				
☑	Cem07_Portlandite	-22.79338	min	1.0	Ca+2	-2.0	H+	2.0	H2O				
☑	Cem07_Syngenite	-7.200000	min	1.0	Ca+2	1.0	H2O	2.0	K+	2.0	SO4-2		
☑	Pyrite	-2.128690e2	min	1.0	Fe+3	1.0	H+	-0.5	H2O	-3.75	O2[g]	2.0	SO4-2
☑	Siderite	-15.35800	min	1.0	CO2[g]	1.0	Fe+3	-3.0	H+	1.5	H2O	-0.25	O2[g]

No input file or directory selected.

Figure 7.6. Overview of the precipitation reactions included in the chemical model.

7.2.4. Chemical composition assumed

The summarized chemical composition of the structural cement / concrete material is given in Table 7.4. To translate these parameters into input for the chemical model, it was assumed that the material in the aggregates is effectively inert during the simulated period. The cement type II consists of CaO, MgO, Al_2O_3, SiO_2 with a ratios indicated in Table 7.4.

7.2.5. Chemical reactions taken into account

The total set of reactions taken into account in case of the clay as well as in the concrete zone is listed in Appendix 1. However, in contrast with the concrete layer, the amount of adsorbing surfaces for clay, hydrous ferric oxides and organic matter are not zero, which effectively takes into account the adsorption reactions with clay (described with a Donnan exchange model), hydrous ferric oxide (described with a Generalized 2 layer model) organic matter (described with a Nica-Donnan model).

Table 7.4. Chemical composition of cement fraction used in the concrete - clay interaction simulations. The aggregate fraction, mainly composed of SiO_2,was assumed to be chemically inert.

	g/100g Portland Cement	mol/100g Portland Cement	molar mass g/mol	Bulk mol/kg		mol/kg	
CaO	62.4	1.1127	56.0794	1.758108	1	1.7581	Ca
SiO_2	18.9	0.3145	60.0843	0.496922	1	0.4969	Si
Al_2O_3	4.4	0.0432	101.961	0.068258	2	0.1365	Al
Fe_2O_3	2.5	0.016	156.0774	0.025281	2	0.0506	Fe
MgO	1.4	0.0347	40.3044	0.054827	1	0.0548	Mg
K_2O	0.95	0.0101	94.196	0.015958	2	0.0319	K
Na_2O	0.1	0.0016	61.979	0.002528	2	0.0051	Na
CO_2	2.1	0.0477	44.01	0.075368	1	0.0754	CO_2
SO_3	3	0.0375	80.0652	0.059251	1	0.0593	S

7.2.6. Chemical composition assumed

For the simulations we have assumed a clay percentage of the solid matrix of 50% clay with an average specific surface area of 500 meq/kg resulting in an overall CEC capacity of 250 meq/kg solid material. This is slightly lower but in the same range, as used for the modelling in Chapter 5.2 where 295 meq/l was used. The adsorption / ion exchange behaviour of organic matter was simulated with a NICA-Donnan adsorption model, which automatically results in pH dependent charging behavior. The total amount of organic matter was estimated at 9 gram per kg (0.9 weight %) .

7.2.7. Transport properties

The physical transport properties of the clay layer were taken equal to those described in Chapter 6.

7.2.8. Discretization

The total concrete-clay boundary system was represented by 100 cells. For the concrete layer the cell thickness was 10 mm (so in total 50 cm), while for the clay layer the layer thickness linearly increased from 10 mm to 500 mm, resulting in an overall thickness of the clay layer of 24.75 m. The variable cell dimensions allowed the model to represent the gradients near the boundary in sufficient detail, while at the same time it was also possible to represent gradients over larger distances of more mobile elements and at longer timescales.

7.2.9. Simulation period

The total simulated period was 10,000 years. To evaluate whether extrapolation of these results to longer timescales is possible we have included a test by extrapolating the results for 1000 year to construct the results for 10,000 years.

7.3. Results and Discussion

7.3.1. Diffusion only

We will first discuss the results of a purely diffusion case where we assume that there is no significant water flow in the concrete-clay system, and subsequently show result of a simulation in which diffusion was combined with an advective water flow of 0.1 mm per year and 1 mm per year.

The output of the model simulations consists of the chemical conditions, such as pH, pe, element and mineral concentrations etc., in the profile as a function of time (Fig. 7.7). In case of the boundary between the alkaline cementitious material of the EBS and the surrounding clay matrix, there initially is a very large contrast in pH values between these zones. Because the pH is a dominant driving factor in soil chemical processes, its deviations from the initial condition can be used as an indicator for the extent of the clay zone that is influenced by the presence of the cementitious material.

From the calculated curves it can be concluded that the zone that is affected by the chemical interaction between the concrete material and the clay is limited to ca. 4 m after 10,000 years. The changes in pH are accompanied by changes in the local chemical conditions, as illustrated by a number of representative other parameters shown in the graphs. The chloride concentration front illustrates the penetration depth for elements with a low reactivity, and thus little retardation. We can see that the depth of the chloride front is similar to the depth of the pH front although protons do interact with the solid matrix and as a result would be expected to migrate slower.

The CSH concentration profile shows a decrease in the concrete matrix, as a result of dissolution. CSH can be considered to be the main reactive substance in the concrete matrix and the mains source of alkalinity production. The clay matrix buffers this alkalinity by a number of different processes such as; ion exchange/ adsorption processes at clay and organic matter particles, but also by dissolution of SiO_2. The profiles show that SiO_2 dissolves close to the clay-concrete boundary where the pH is high, and part of it precipitates further away from the boundary, where the pH is lower.

The sulfur profiles show an increase in dissolved sulfur concentrations, which is the result of oxidation of sulphide/pyrite at the boundary. The concentration profiles clearly show that the penetration depth of the changes is much greater in the clay zone than in the concrete matrix, which is caused by the much larger chemical reactivity per volume of concrete in comparison with the clay.

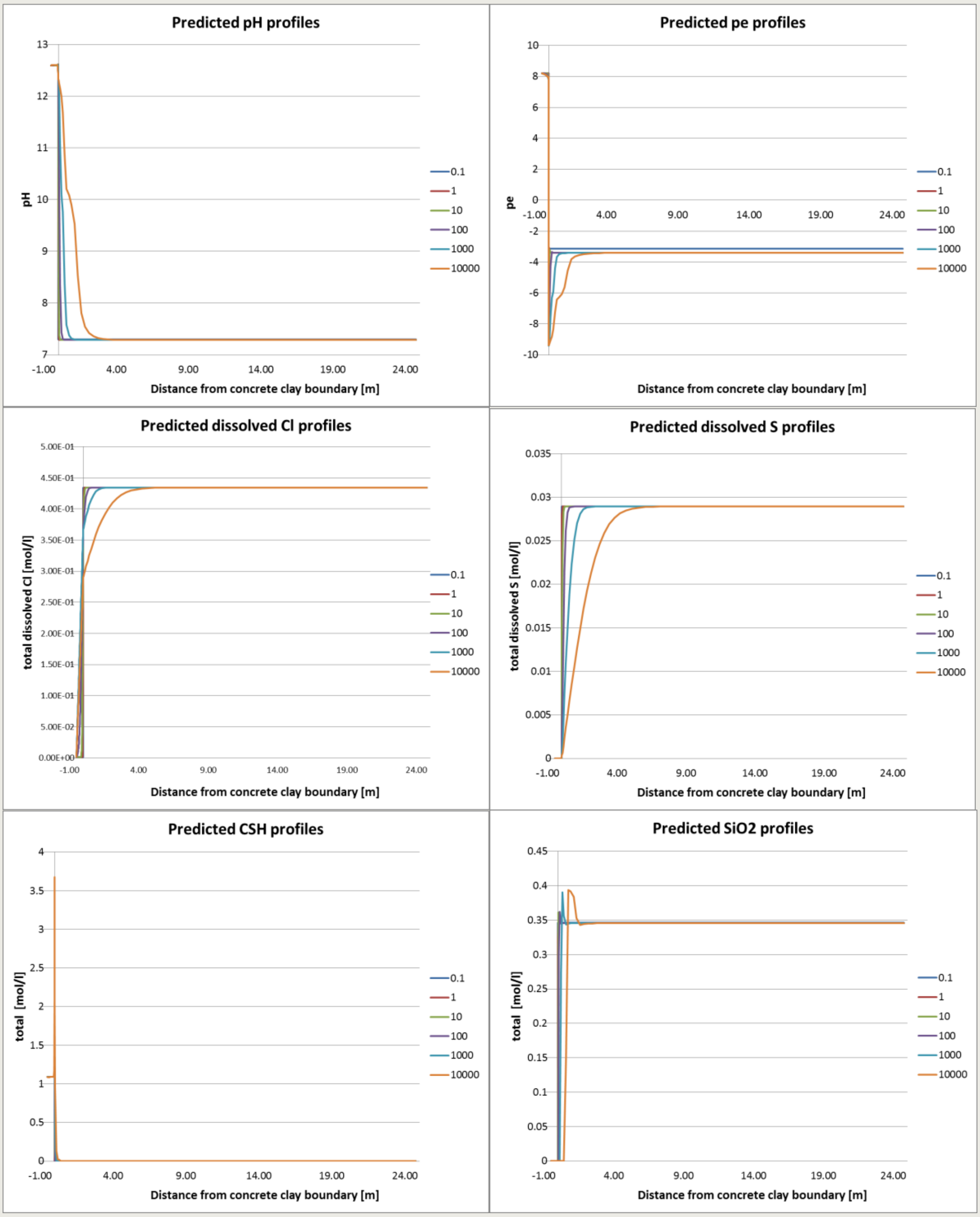

Figure 7.7. pH profiles at the EBS clay interface as a function of time (in years; diffusion).

To evaluate whether it is possible to extrapolate the results obtained with the reactive transport model to longer times we compared the results for 10,000 years, as calculated with the reactive transport model, with the results extrapolated from the curves at 1000 years by assuming a simple square root relationship between travel distance and square root of travel time. Which is generally valid for monocomponent linear diffusion systems in which case travel distance is proportional to √time.

So the concentration profile for 10,000 years was constructed by multiplying the travel distance for the profile at 1000 years with √10 and compared with the actual simulation for 10,000 years. The results are shown in Figures 7.8 and 7.9. The good agreement between the numerically calculated and extrapolated curves for pH and pe demonstrate that extrapolation is quite accurate.

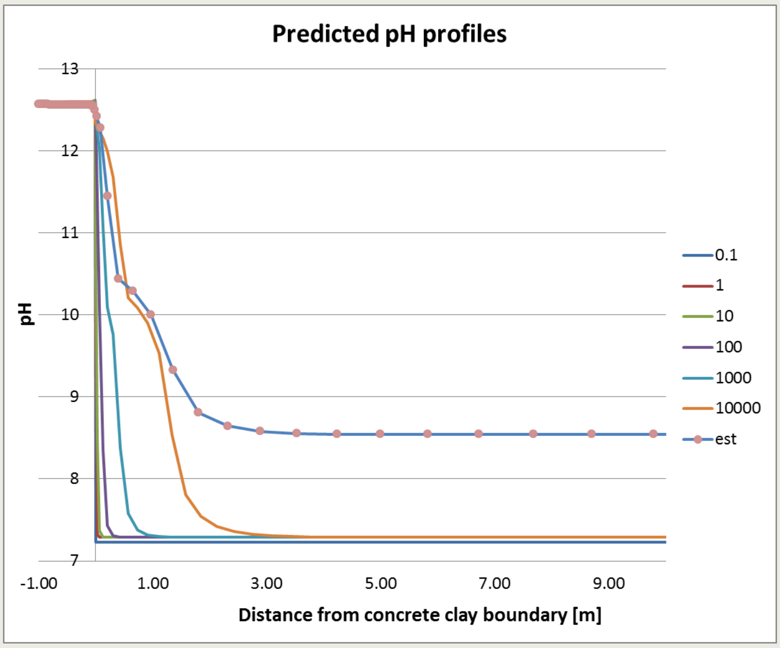

Figure 7.8. pH profiles at the EBS clay interface as a function of time (in years; diffusion). The extrapolated curve for 10000 years is constructed from the curve for 1000 years by multiplying the distance with √10.

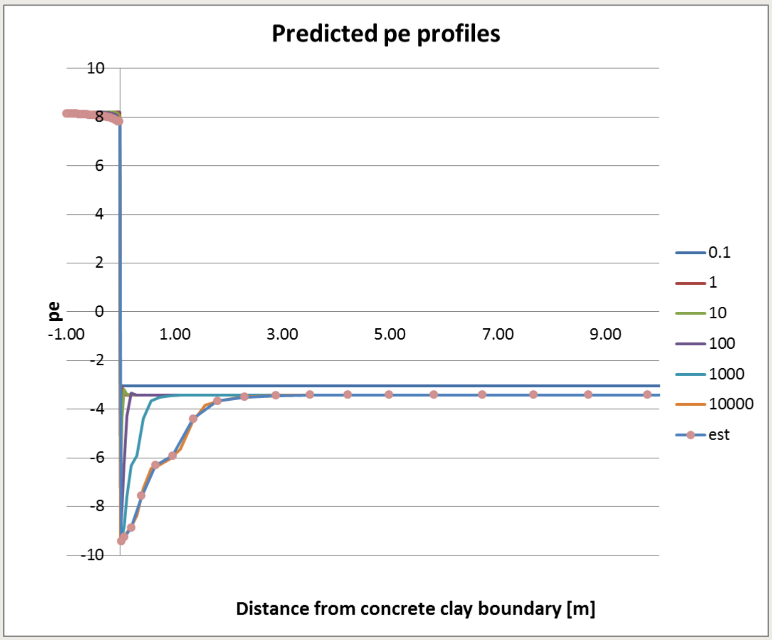

Figure 7.9. pe profiles at the EBS clay interface as a function of time (in years; diffusion). The extrapolated curve for 10000 years is constructed from the curve for 1000 years by multiplying the distance with √10.

The results show that even for the non-linear chemical processes involved it is possible to extrapolate the results to longer time periods if necessary. This simplification assumes a large (infinite) thickness of the concrete layer, and will become inaccurate when the concrete material is completely reacted. If this occurs the simple extrapolation will overestimate the distance over which interaction of the concrete solution with the clay matrix occurs.

7.3.2. Diffusion plus advection

To evaluate the effect of possible water flow we have included simulations that take into account the combination of interaction by diffusion and by additional advective water flow. From the results presented in chapter 8, where hydraulic conductivity and pressure gradients are discussed, we have selected simulations with a water flow of 0.1 mm per year, and, for illustration purposes, a second simulation with a flow rate of 1 mm year.

Figure 7.10 shows the results for a Darcy velocity of 0.1 mm per year. This is equivalent to a total travel distance of 2.5 m in 10.000 years for a porosity of 0.35. If we compare the results with the pure diffusion case, we can see that the results are virtually the same. This indicates that for a Darcy velocity of 0.1 mm per year, diffusion will be the dominant process for at least 10,000 years.

At longer timescales the relative importance of advection will increase and may become the dominant process over longer timescales and further distances, because advective transport linearly increases with time and diffusive transport with square root of time. An accurate estimation of possible water flow rates is needed to substantiate this further. For illustration purposes we also performed a calculation for a flow rate of 1 mm per year (Figure 7.11). This flow rate is at the high range for clay layers at several hundred meters below surface (Valstar & Goorden, 2016). Here we can see, as indicated by the pH and chloride fronts at 10.000 years, that the interaction depth becomes 10 time larger in comparison with a flow rate of 0.1 mm per year. Although 1 mm per year can be considered as a high value, realistic estimations of the actual flow rate depend on reliable estimations or data on hydraulic pressure gradients over the Rupel Clay layer (see chapter 8).

7.4. Conclusions

The results presented in this chapter show that there will be interactions between a concrete EBS structure and the surrounding clay layer. However, the distance over which these interactions will affect the chemical will be limited to several meters for a time period of 10,000 years. The potential effect of changes in porosity were not taken into account. Here, the production of H_2 by in particular corrosion was not taken into account (cf. section 3.1). This might impact the redox processes locally when reactive species as degradable organic matter, Fe(III)-bearing minerals or SO_4 are present.

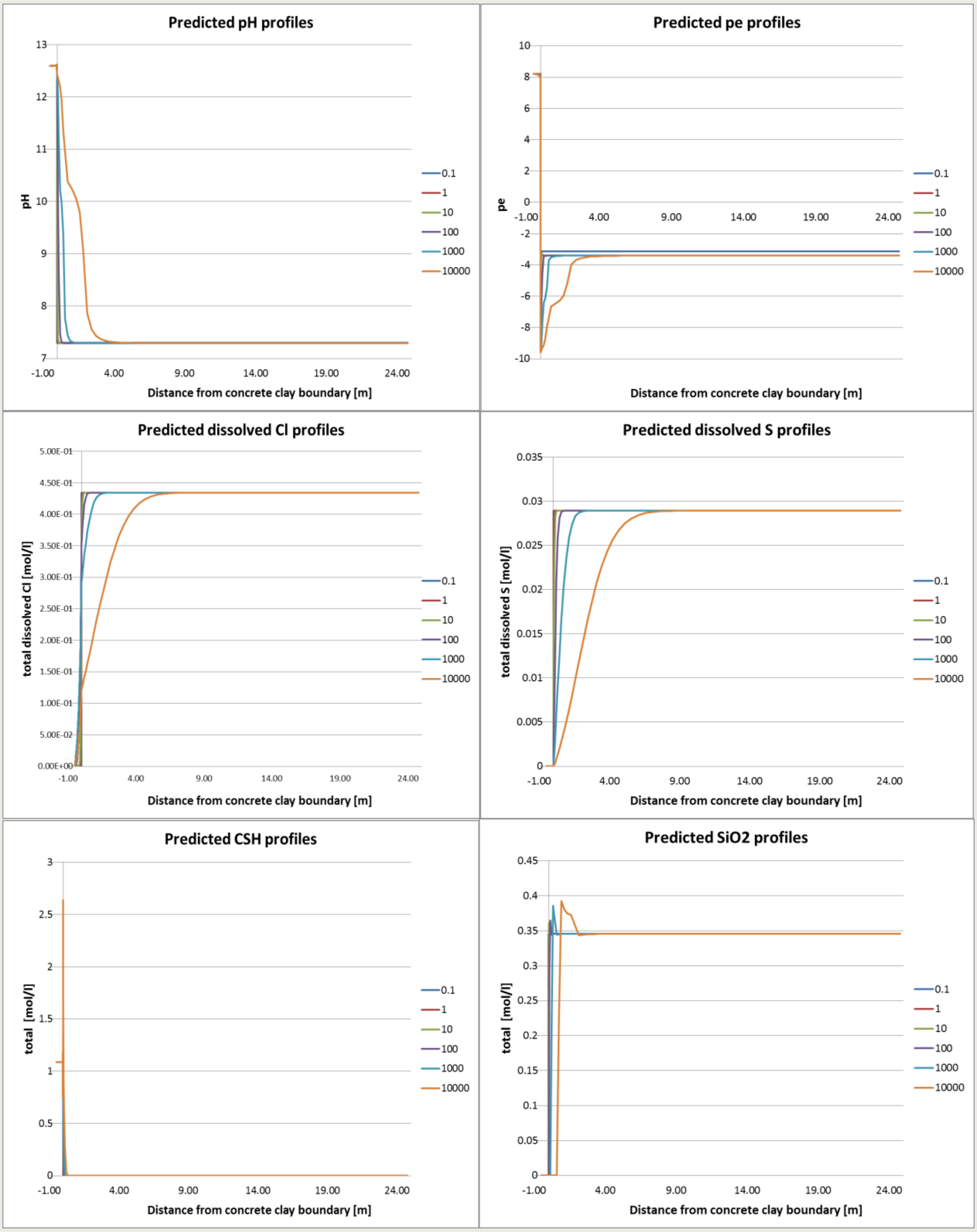

Figure 7.10. pH, pe, profiles at the EBS clay interface as a function of time (in years; diffusion + 0.1 mm/yr Darcy flow).

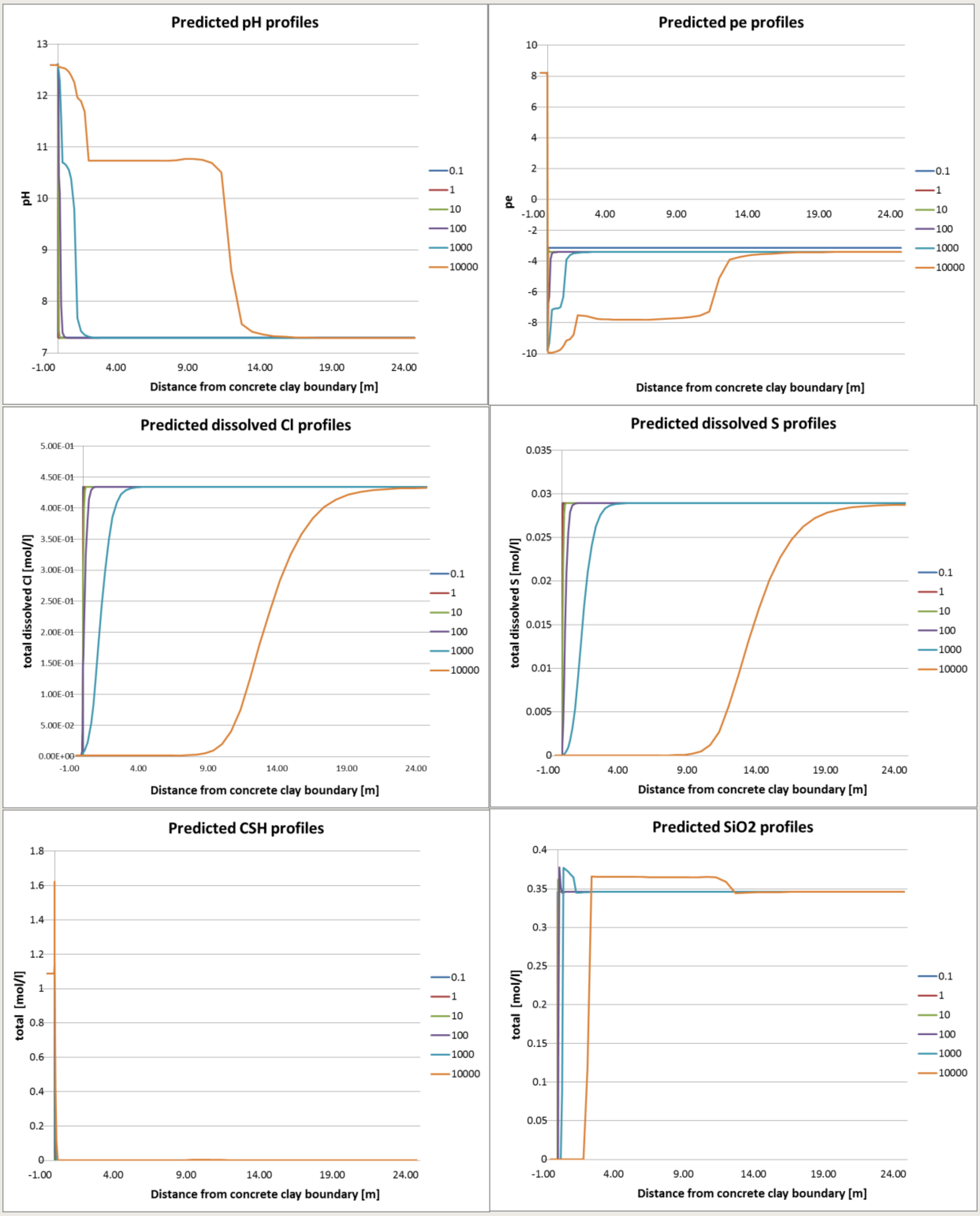

Figure 7.11. pH, pe, and concentration profiles at the EBS clay interface as a function of time (in years; diffusion + 1 mm/yr Darcy flow).

8. Advective flow in the Rupel Clay and the impact of faulting

8.1. Introduction

Valstar & Goorden (2016) analysed the advective flux through the Rupel Clay on a regional scale. This approach means that some processes could not be included. These are:

- The effect of density variations due to temperature and salinity
- The effect of faults on the flow
- The effect of diffusion and dispersion

Also, they could not take into account available, detailed measurements.

To refine the estimates and estimate the effects of some of the processes that were not included, more detailed modelling of the Rupel Clay was done. To do the calculation of the flow velocity through the Rupel Clay, three key inputs are required: permeability and thickness of the Rupel Clay and pressure difference over the Rupel Clay. Since reliable information on these parameters is not available on a regional scale, the inputs are based on what local information is available. Since these observations are local, the results are limited to an indication of what happens on a regional scale. The analysis of the existing, relevant field data is discussed in the next section. The flow simulations and results are discussed afterwards.

8.2. Method and materials

8.2.1. Groundwater heads

The number of wells with measurements of pressure and/or groundwater heads above and below the Rupel Clay is very limited. The following wells (see Figure 8.1) were identified which have measurements of hydraulic head above and below the Rupel Clay in the Netherlands:

- B49F1427
- B50H0373
- B58G0192
- B52E0114

The wells are shown on the thickness map of the Rupel Clay derived by Vis et al. (2016). For this map mainly oil and gas wells were used, because most groundwater wells do not penetrate the Rupel Clay. This is why some of the wells are in the area shown with uncertain thickness.

Of these wells only the first two are suitable for the analysis, since B58G0192 and B52E0114 are influenced by the large scale groundwater withdrawal at the lignite quarries across the border with Germany (Stuurman, 2004 and Figures 8.2 and 8.3). The increase in groundwater head in B58G0192 after 1998 is probably related to a decrease in groundwater withdrawals (Stuurman, 2004). The groundwater level observations in B49F1427 and B50H0373 are shown in Figures 8.4 and 8.5, respectively. Filter 9 is in both cases the deepest filter, which is below the Rupel Clay. Filter 8 shows the groundwater head just above the Rupel Clay. From these values the head difference over the Rupel Clay can be derived. For B49F1427, the groundwater head below the Rupel Clay was higher than above suggesting upward flow. For B50H0373, this is reversed indicating downward flow. These heads are, however, not corrected for temperature and density. In the next section the groundwater heads are, therefore, corrected for salinity and temperature.

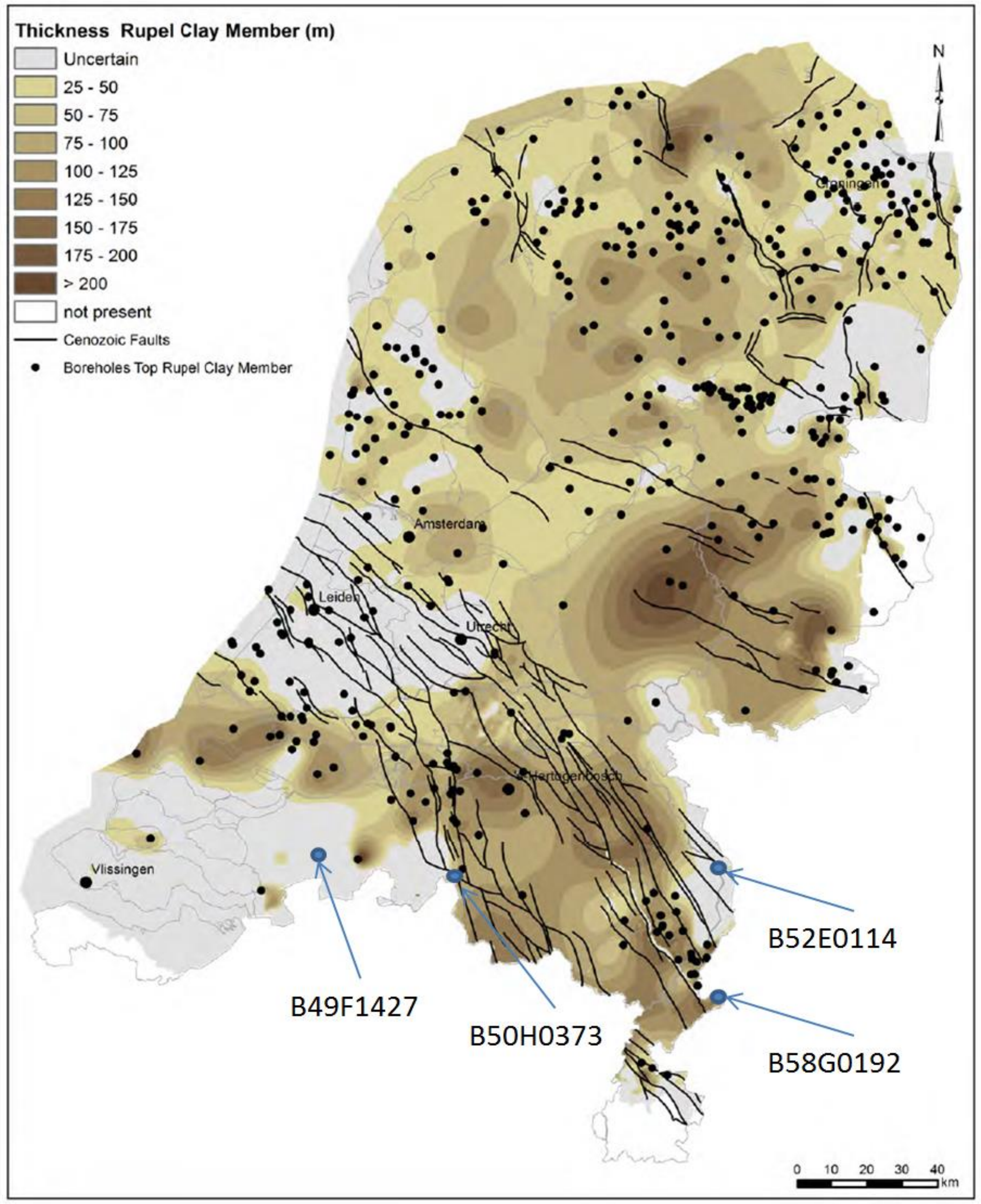

Figure 8.1. Location of wells with observations of hydraulic head above and below the Rupel Clay shown on the map with estimated thickness of the Rupel Clay by Vis et al. (2016).

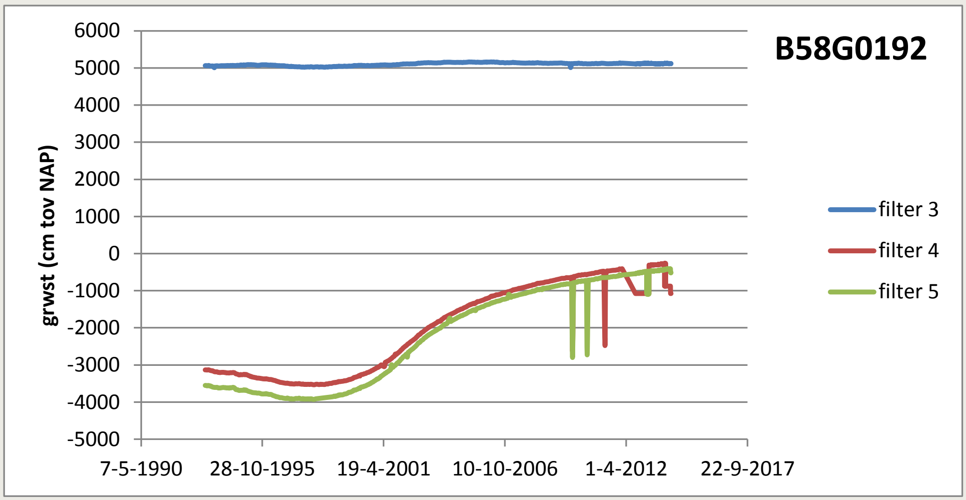

Figure 8.2. Groundwater head observations in B58G0192 in two filters below the Rupel Clay (filters 4 and 5) and one above (filter 3).

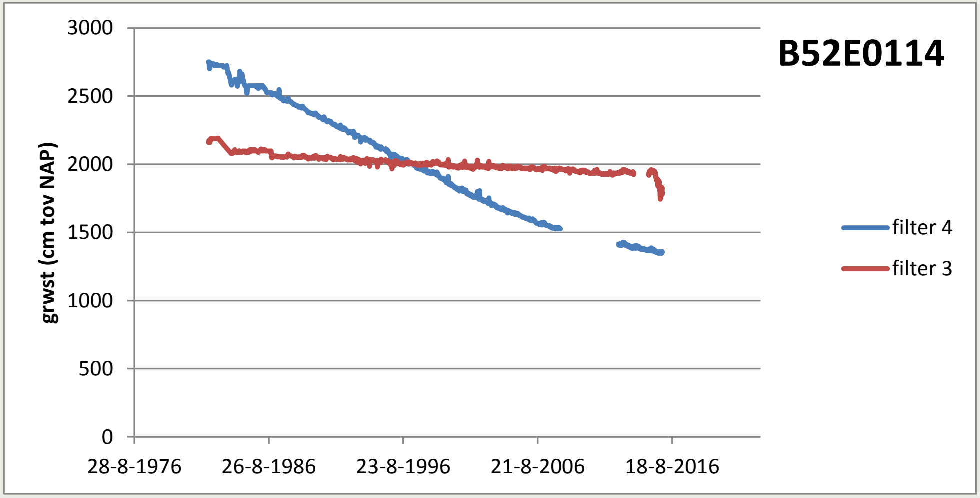

Figure 8.3. Groundwater head observations in B52E0114 in one filter below the Rupel Clay (filter 4) and one above (filter 3).

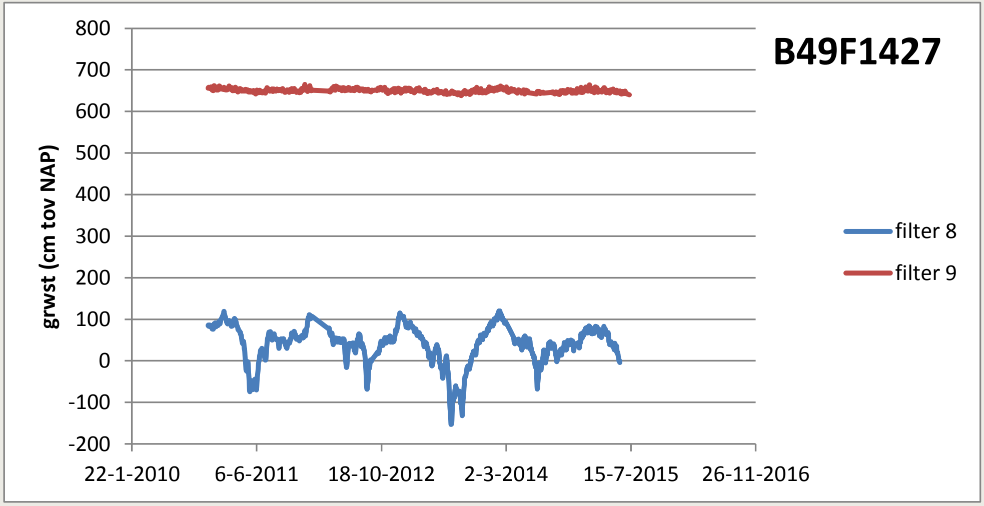

Figure 8.4. Groundwater head observations in B49F1427 in one filter below the Rupel Clay (filter 9) and one above (filter 8).

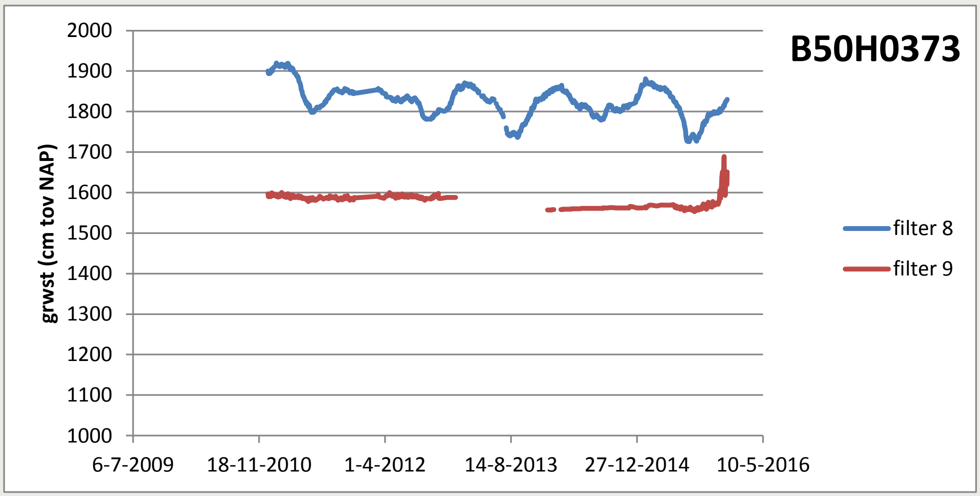

Figure 8.5. Groundwater head observations in B50H0373 in one filter below the Rupel Clay (filter 9) and one above (filter 8).

8.2.2. Recalculation of the groundwater heads

Groundwater head as observed for wells B49F1427 and B50H0373 is a correct representation of pressure only when the density is constant. Since at these depths, salinity and temperature are higher, this assumption does not hold. In order to use these values to calculate the flow across the Rupel Clay, the groundwater heads need~~s~~ to be recalculated to pressure. This is done by taking into account the effect of pressure, temperature and salinity on the density. The density of the brine as a function of salinity, temperature and pressure was calculated according to Spivey et al. (2004). First, an accurate hydrostatic pressure profile is calculated based on these densities. Next, the observed hydraulic head is recalculated to pressure assuming that the tubing is filled with water of formation quality. The comparison of these two values gives the actual pressure and/or head difference over the Rupel Clay.

Table 8.1. Example calculation of the pressure above and below the Rupel Clay for well B49F1427.

Depth	Location	Salinity	Temperature	Density	Hydrostatic Pressure**	Observed head	Observed pressure	Difference (head)
m TVD*		mg/l	°C	kg/m3	Pa	m TVD	Pa	m (@ 1000 kg/m^3)
0	surface		10	999.7	0			
-217	Top filter 8	2000	16.5	1001.2	2.13E6	-5.57	2.08E6	-5.4
-236	Top Rupel Clay	2000	17.1	1001.2	2.32E6			
-388	Bottom Rupel Clay	19916	21.6	1013.6	3.83E6			
-409	Top filter 9	19916	22.3	1013.5	4.04E6	0.584	4.07E6	3.6

*TVD = True Vertical Depth below land surface.
** pressure is given compared to atmospheric pressure for comparison with observed head.

Reliable temperature observations were not available. Therefore, we assumed that the temperature follows a geothermal gradient of 3°C/100 m (Verweij and Nelskamp, 2015). For both wells, a high salinity was measured below the Rupel Clay. This salinity was also assumed within the Rupel Clay. Above the Rupel Clay, no observations of salinity were present and a value of 2000 mg/l was assumed (based on shallower wells in the area). The head used is the average groundwater head over the entire period of observation (Figures 8.4 and 8.5).

Table 8.1 gives an example calculation for well B49F1427. The total gradient in hydraulic head over the Rupel Clay is 9 m ($0.9 \cdot 10^{-5}$ Pa) in this example. The gradient is such that in this location upward flow through the Rupel Clay is expected. The same calculations were also done for well B50H0373. For this well, the total head difference over the Rupel Clay was only 0.3 m (or $0.03 \cdot 10^{-5}$ Pa) (Table 8.2), also indicating upward flow. The hydraulic head difference reported at the regional scale by Verweij and Nelskamp (2015) is between -0.7 and 0.7 m, which is clearly considerably smaller than the value calculated for well B49F1427 but in good agreement with borehole B50H0373.

Table 8.2. Example calculation of the pressure above and below the Rupel Clay for well B50H0373 (footnotes as for table above).

Depth	Location	Salinity	Temperature	Density	Hydrostatic Pressure**	Observed head	Observed pressure	Difference (head)
m TVD*		mg/l	°C	kg/m3	Pa	m TVD	Pa	m (@ 1000 kg/m^3)
0	MV		10	999.7	0			
-314	Top filter 8	2000	19.4	1001.0	3.08E6	-3.92	3.04E6	-3.7
-334	Top Rupel Clay	2000	20.0	1001.0	3.28E6			
-487	Bottom Rupel Clay	15177	24.6	1009.8	4.79E6			
-492	Top filter 9	15177	24.8	1009.8	4.84E6	-6.51	4.81E6	-3.4

8.2.3. Properties of the Rupel Clay

The properties of the Rupel Clay most important for the calculation of the flow are the vertical permeability and the thickness. The vertical permeability has been analysed by Vis et al. (2014). He also analysed well B50H0373. For most of the thickness of the Rupel Clay, the permeability was in the order of $1 \cdot 10^{-18}$ m^2. However, sandier parts can have higher permeability, which increases the average permeability. The permeability can be recalculated to hydraulic conductivity (K in m/s) via:

$$K = k\frac{\rho g}{\mu}$$

where:

ρ : density (kg/m3)
g : gravitational acceleration (m/s^2)
μ : dynamic viscosity (kg/(m·s))

With the appropriate values for the Rupel Clay in this well ($\rho = 1013$ kg/m^3, g=9.81 m/s^2 and $\mu = 0.98 \cdot 10^{-3}$ kg/(m·s)) this results in $1.01 \cdot 10^{-11}$ m/s, which is $8.8 \cdot 10^{-7}$ m/d. The values used by Valstar in the regional modelling are in the order of $5 \cdot 10^{-4}$ m/d for vertical permeability, which is an order of magnitude larger (Verweij and Nelskamp, 2015). Wemaere et al. (2008) evaluated vertical hydraulic conductivity values of the Rupel Clay at the formation scale in Belgium. He estimated a value of $2.6 \cdot 10^{-7}$ m/d at the Mol site to $8.6 \cdot 10^{-7}$ m/d at the Doel site. The horizontal permeability is a factor of 5 to 60 larger than the horizontal permeability at the formation scale according to Wemaere et al.(2008).

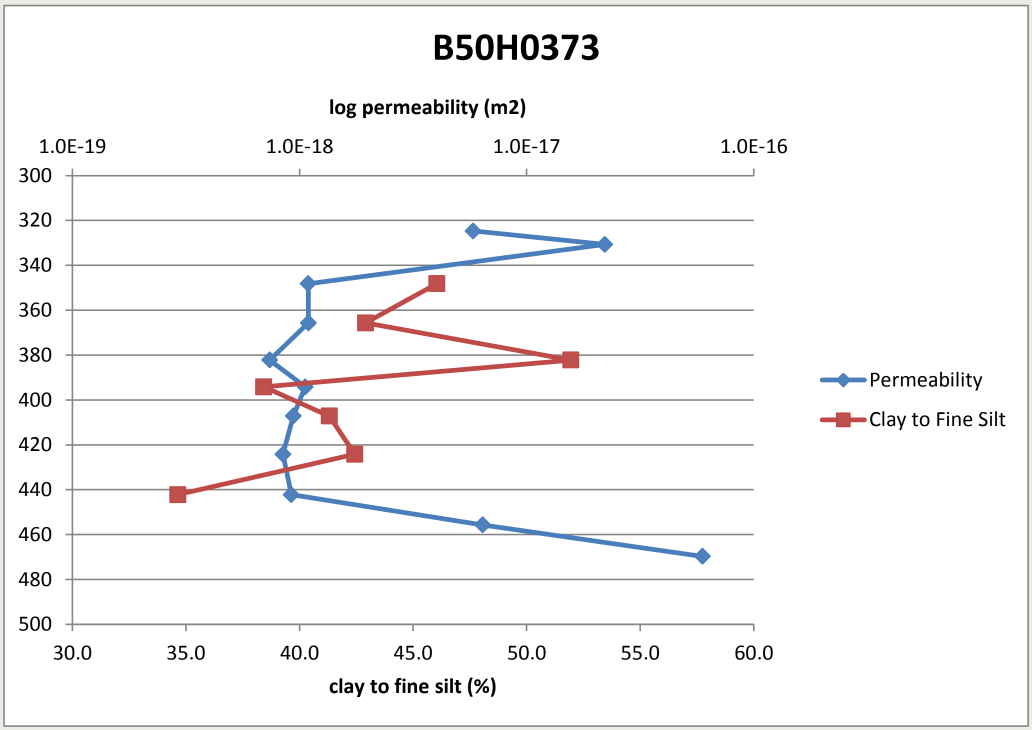

Figure 8.6. Vertical permeability of the Rupel Clay in B50H0373 (based on the data from Verweij et al., 2016).

The thickness of the Rupel Clay is highly variable (Figure 8.1). Also, the related thickness calculations cover only part of the Rupel Clay, since in some areas no wells were available. A further complicating factor is that the Rupel Clay also has sandier parts, which have a much higher permeability (Figure 8.6). Thus, the effective thickness for which the Rupel Clay acts as aquitard may be smaller than shown in Figure 8.1.

8.2.4. Flow calculations

The code TOUGH2 (with eos7c) is used for the flow calculations (Pruess et al., 2012; Oldenburg et al., 2004). Flow is simulated for pure water and isothermal conditions. The model setup is as follows:

- A both the top and the bottom boundary a fixed pressure condition is applied. This will generate a steady state vertical flux through the Rupel Clay. Since no horizontal gradient in the pressure is applied, the flow is perfectly vertical in the base case.
- The Rupel Clay is 100 m thick. Above and below the Rupel Clay 250 m of sand was simulated, which should place the boundaries sufficiently far from the Rupel Clay (Figure 8.7). Thus in the model, the Rupel Clay is from 250 to 350 m depth, which is not the actual depth of the Rupel Clay, which was assumed to be 750 m.
- The pressure drop over the Rupel Clay of $1{\cdot}10^{-5}$ Pa (10 m head) compared to hydrostatic pressure. In this case a downward flow in the Rupel Clay is assumed, in contrast to the flow in the two observed wells. Downward flow generally shows longer travel times and is thus more beneficial for disposal (Valstar and Goorden, 2016)
- Horizontal and vertical permeability are $1{\cdot}10^{-17}$ m^2 and $1{\cdot}10^{-18}$ m^2 respectively for the Rupel Clay and $1{\cdot}10^{-12}$ m^2 and $1{\cdot}10^{-13}$ m^2 for the sandy formations above and below the Rupel Clay.
- The effective porosity is assumed to be 0.18 in the Rupel Clay which lies within the lower range estimated by Vis & Verweij (2014) and 0.35 in the sandy formations which is a standard value for uncemented sandy aquifers.

The resulting steady state flow profile gives the flow velocity in the Rupel Clay.

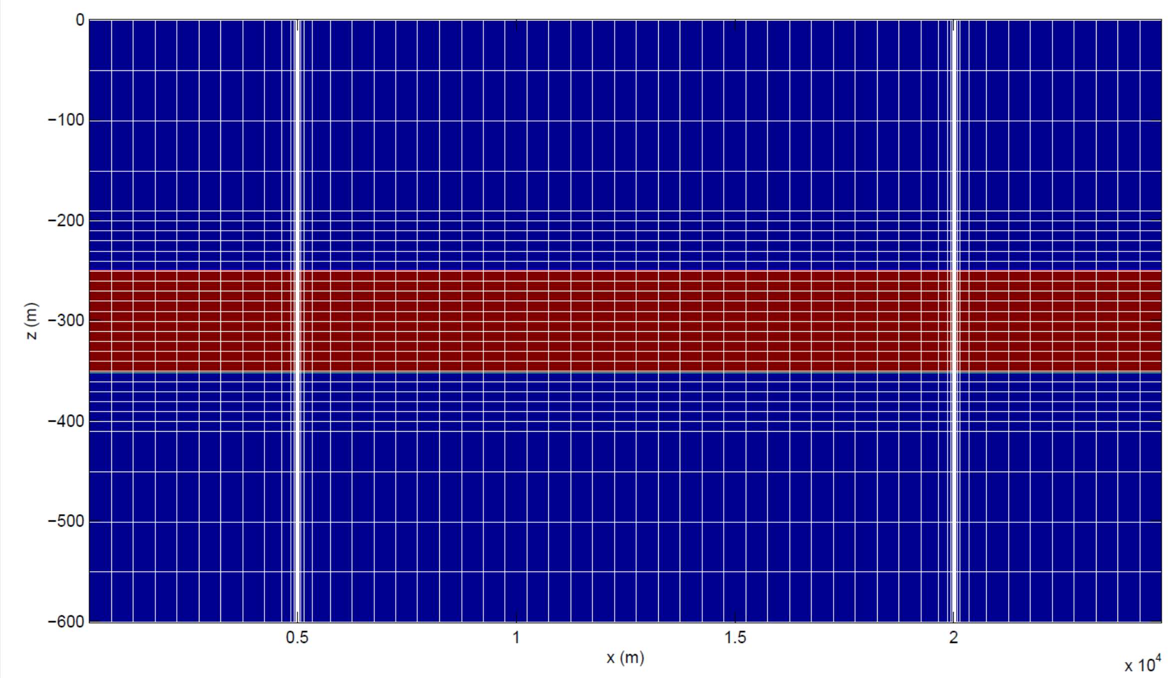

Figure 8.7. Overview of the base case showing the Rupel Clay in red and the grid as white lines. The faults are located at 500 m and 2 km.

Also for the specific cases for the two wells, the flow velocity across the Rupel Clay was simulated. The depth profile was taken as presented in Tables 8.1 and 8.2. However, the Rupel Clay was divided into two parts based on the borehole description: clay and sandy clay. Vertical permeability for the clay part was set to the same values as for the base case ($1 \cdot 10^{-18}$ m^2 in vertical direction and $1 \cdot 10^{-17}$ m^2 in horizontal direction), whereas the permeability for the sandy clay was set a factor of 10 higher. For well B50H0373, the thickness of the clay was taken as 105 m and the thickness of the sandy clay as 50 m. For well B49F1427, clay was 125 m and sandy clay 25 m.

8.3.Results

The flow velocity calculated for the base case is presented in Table 8.3 together with the flow velocity for the two wells. Due to the very small head gradient in well B50H0373, the travel time in this well is much larger than in the base case of well B49F1427. The calculated flow in the two well locations is upward (seepage instead of infiltration). The results in Figure 4.5 of Verweij and Nelskamp (2015) also indicate upward flow at these locations. However, the Darcy velocity is considerably larger, which is mainly determined by the large permeability used in these publications. Note that the pore water velocity is 0.1 mm/y for well B49F1427.

Table 8.3. Overview of the flow velocity in the center of the Rupel Clay.

Name	Flow velocity* (m/s)	Darcy flow velocity (m/s)	Half thickness** (m)	Travel time within the Rupel Clay (yr)
Base case	4.91E-12	8.83E-13	50	3.23E+05
B49F1427	-3.30E-12	-5.94E-13	62.5	6.01E+05
B50H0373	-1.41E-13	-2.53E-14	52.5	1.18E+07

* A positive flow velocity indicates a downward direction.

** The travel time is calculated from the middle of the Rupel Clay to the boundary (in vertical direction).

Since the flow is perfectly vertical in the base case, the sensitivity of the flow velocity to permeability, pressure difference over the Rupel Clay and thickness of the Rupel Clay can easily be evaluated via:

$$q = k\frac{\rho g}{\mu}\frac{\Delta P}{H}$$

Where:

q : Darcy flow velocity (m/s)
k : permeability of the Rupel Clay (m^2)
ρ : density (kg/m3)
g : gravitational acceleration (m/s^2)
μ : dynamic viscosity (kg/(m·s))
ΔP : pressure difference over the Rupel Clay (Pa)
H : thickness of the Rupel Clay (m)

If average permeability or the pressure difference is 10 times larger, the velocity also increases by a factor of 10. For the thickness the relation is inversely proportional. Since the uncertainty in the permeability is very large and can easily be several orders of magnitude (Verweij et al., 2016), this parameter will have the largest impact on the estimated flux. The relevant permeability is the average vertical permeability. Since the flow is also vertical, the averaging must be done harmonically. This means that the lowest permeability dominates the average.

8.3.1. Sensitivities

Faults

In the first test, the impact of faults on the flow velocity in Rupel Clay was tested. Two scenarios were defined with an offset between the fault blocks of 30 m and 60 m, respectively. In both cases, the faults are open to flow. The width of the fault block is 15 km, as in the base case. The impact of the faults is very local: the impact is practically gone at more than 500 m away from the fault (Table 8.4). Figure 8.8 shows the flow velocity in the area of the fault. Please note that the flow velocity is larger in the Rupel Clay than in the sand, due to the smaller effective porosity. The Darcy velocity (flux) is, however, identical. It can also be seen that the flow in the Rupel Clay away from the fault is predominantly in vertical direction.

Table 8.4. Flow velocity in the Rupel Clay at 500 m away from the fault for the base case and two scenario's with different offset for the faults.

Name	Flow velocity (m/s)	Darcy flow velocity (m/s)	Half thickness (m)	Travel time within the Rupel Clay (yr)
Base case	4.91E-12	8.83E-13	50	3.23E+05
Offset 30 m	4.91E-12	8.83E-13	50	3.23E+05
Offset 60 m	4.91E-12	8.83E-13	50	3.23E+05

On the larger scale, conductive faults could reduce pressure build-up and thus flow through the Rupel Clay. This is illustrated in a simulation with a flow boundary condition rather than a pressure boundary condition. In the base case, a fixed pressure boundary condition was used for both the top and the bottom boundary of the model domain and thus changes in pressure due to the presence of faults cannot be evaluated. Also the fixed pressure causes a fixed flow rate through the Rupel Clay between the faults. Therefore, a new model setup was used to examine the effect of faults in a different way.

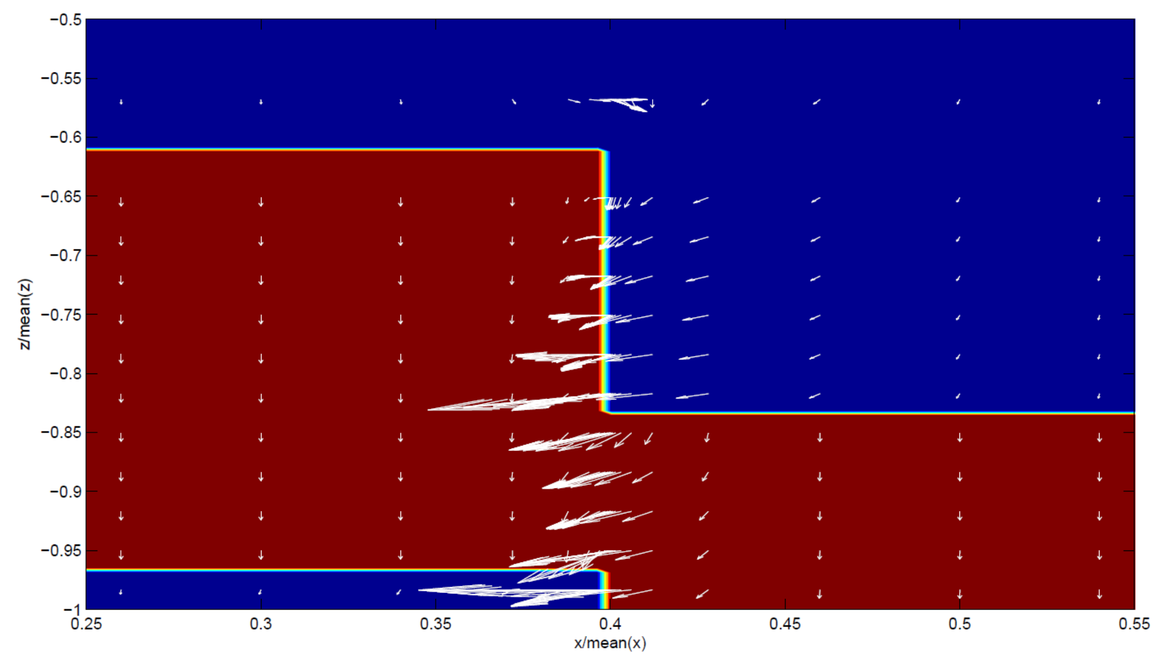

Figure 8.8. Flow vectors indicating the flow across a fault. The length of the vectors is determined by the velocity of the flow. Red background color is the Rupel Clay. Blue indicates sand.

In the new setup, we used a flow boundary condition at the top of the model. The flows implemented at the top are the flows simulated in the base case run. The bottom boundary condition is still a fixed pressure boundary. The faults are again conductive to flow. The results show a decrease in the Darcy flow velocity in the Rupel Clay from $8.83 \cdot 10^{-13}$ m/s without off set across the faults to $8.66 \cdot 10^{-13}$ m/s with 60 m offset across the fault. The difference is the result of more flow being diverted along the conductive faults. Near the fault, only 40 m of Rupel Clay needs to be crossed instead of 100 m, so the resistance to flow is lower. The presence of sealing faults on the other hand might increase a pressure build-up and thus increase flow through the Rupel Clay.

Diffusion

To estimate the impact of diffusion on the travel time in addition to advection, a different grid needs to be used with finer grid cells in the Rupel Clay. The new grid is shown in Figure 8.9. In the middle of the Rupel Clay, the grid height is now 2 m instead of 10 m in the original model. A tracer is placed in the middle of the Rupel Clay and then allowed to migrate with and without diffusion. To allow symmetric flow, the Rupel Clay is now 102 m thick instead of 100 m. The tracer is placed in the central layer that is 2 m thick. The diffusion coefficient is $1 \cdot 10^{-10}$ m^2/s (Rousseau-Gueutin et al., 2008; Cruchaudet et al., 2008).

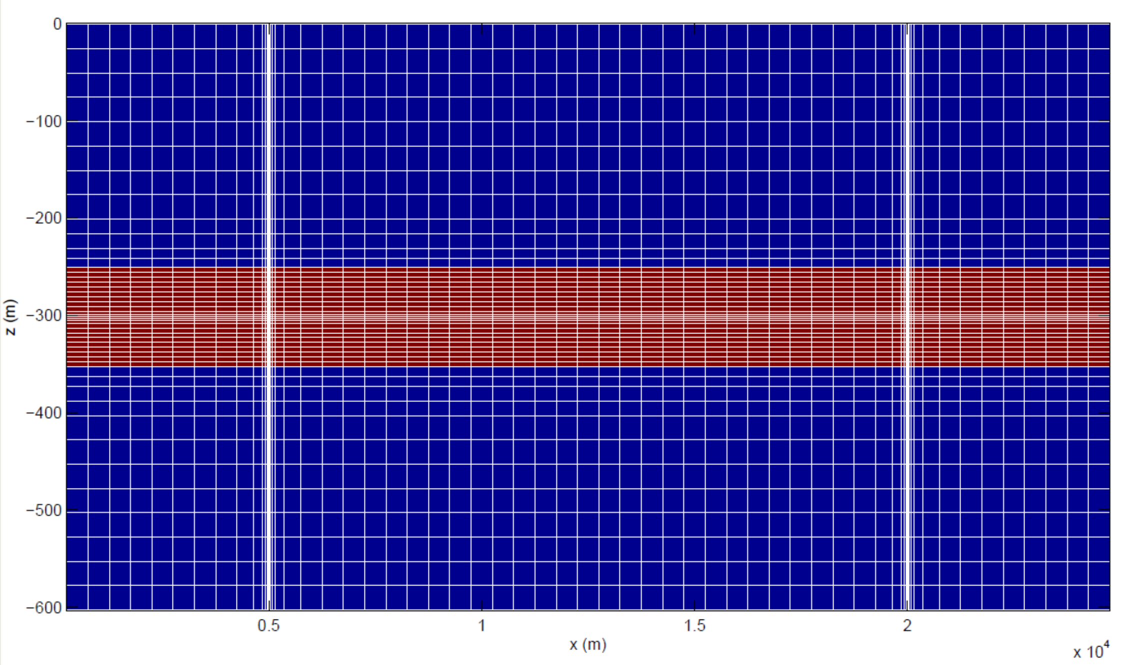

Figure 8.9. Overview of the grid used for evaluation of the effect of diffusion showing the Rupel Clay in red and the grid as white lines. The faults are located at 500 m and 2 km.

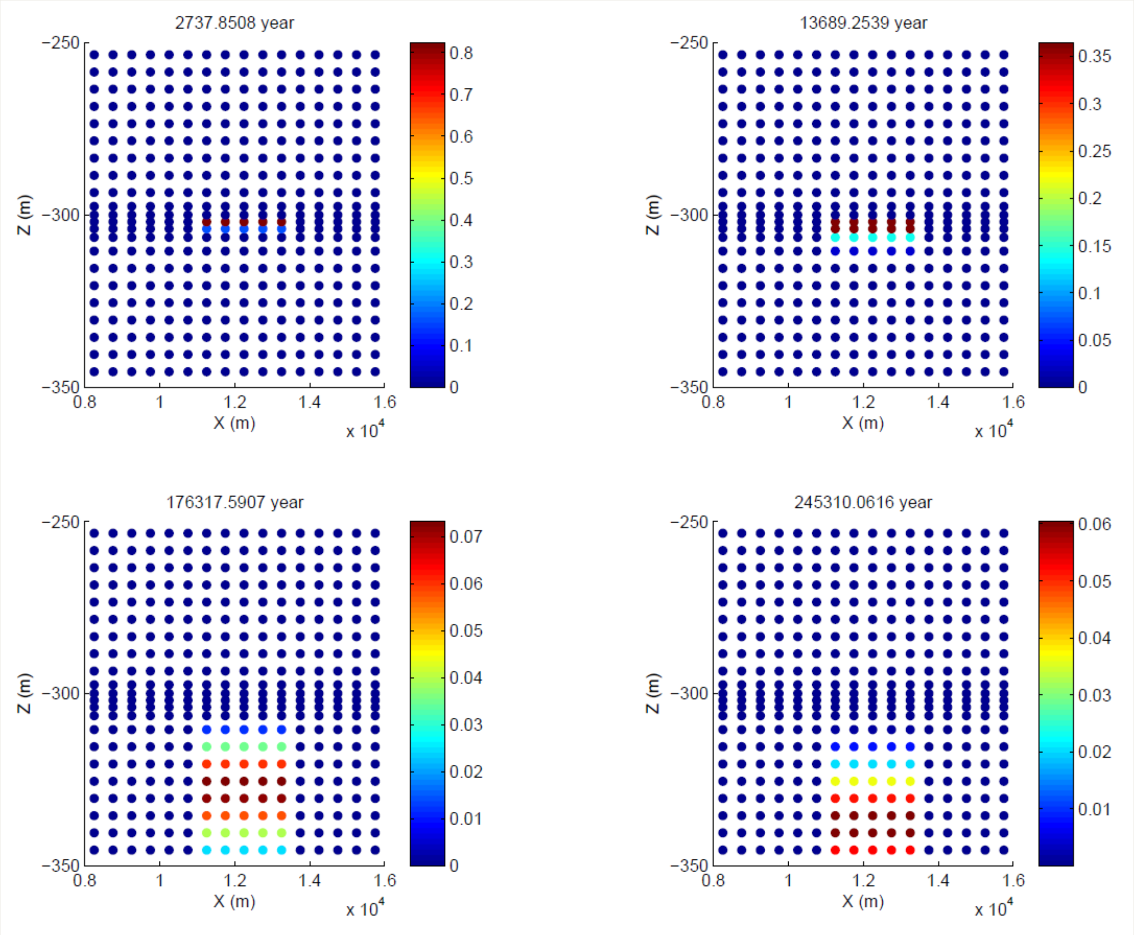

Figure 8.10. Transport of the tracer over time with advection only. The colorbar shows the fraction of tracer in a gridblock. The fraction of tracer in the grid blocks in which the tracer was placed was 1.

In Figures 8.10 and 8.11 the transport of the tracer is shown without and with diffusion, respectively. From a comparison of the plots it is clear that diffusion has a small impact when advection is also happening: it mostly makes the front wider (lower peak and longer tails) but the temporal shift in the centre of the pulse remains the same. This is further illustrated in Figure 8.12, which shows the concentration profile of the tracer with depth in a column in the central part of the model. This plot shows that the depth of the peak in tracer concentration has moved from the original depth of 300 m to around 340 m (almost leaving the Rupel Clay which ends at 350 m depth). The tracer front has moved out of the Rupel Clay to below 400 depth.

The position of the front is affected by numerical dispersion. To evaluate the effect of numerical dispersion, a finer and coarser grid were run for comparison. The results are shown in Figure 8.13. As expected the peak becomes higher for the fine grid and lower for the coarse grid. The effect of the numerical dispersion is in the same order as that of the diffusion (compare Figures 8.12 and 8.13). An effect not accounted for yet is the physical (or mechanical) dispersion. For large advective velocity, dispersion is usually larger that the effect of diffusion. However, for the very small velocities in this case (see Table 8.4), the dispersion (velocity * dispersivity) is probably in the same order of magnitude as the diffusion.

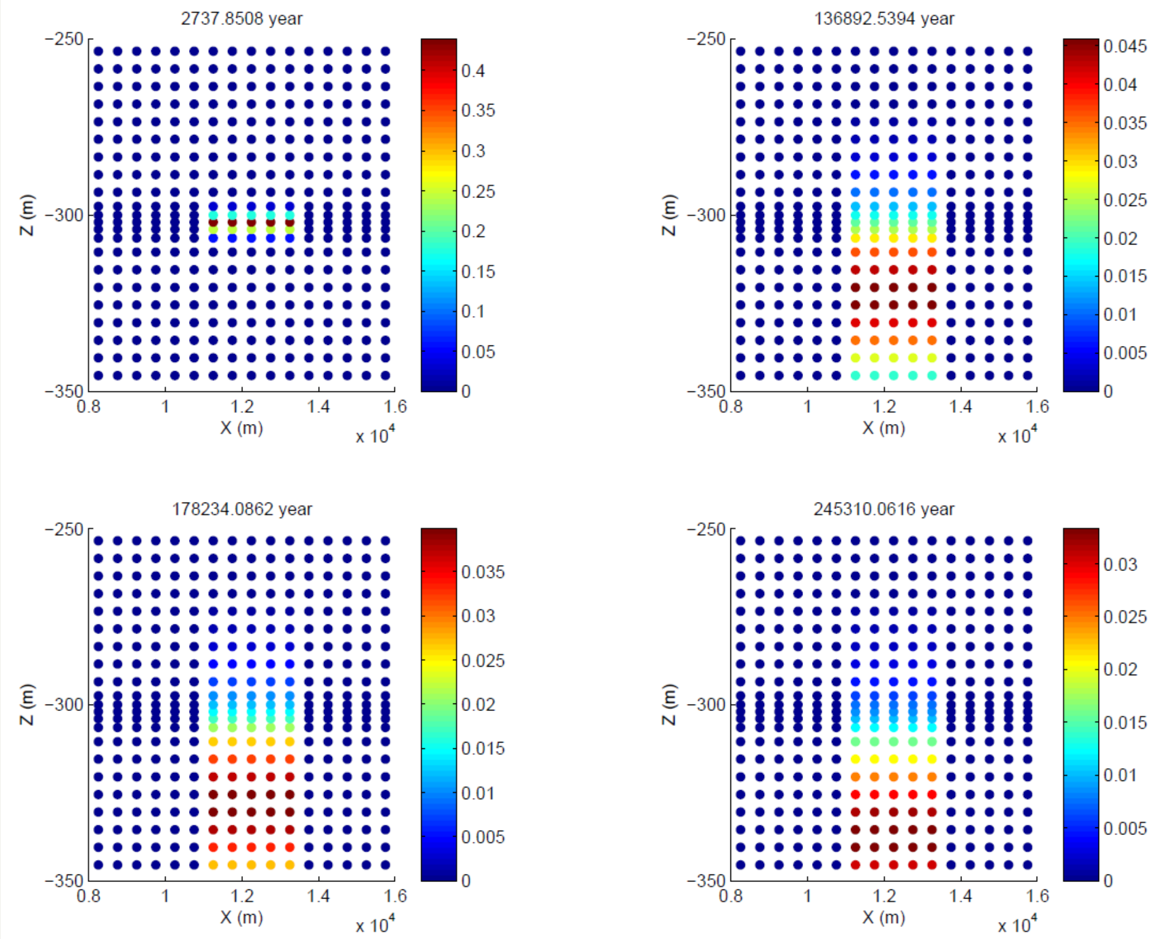

Figure 8.11. Transport of the tracer over time with advection and diffusion. Color bar showing the fraction of tracer in a grid block. The fraction of tracer in the grid blocks in which the tracer was placed was 1.

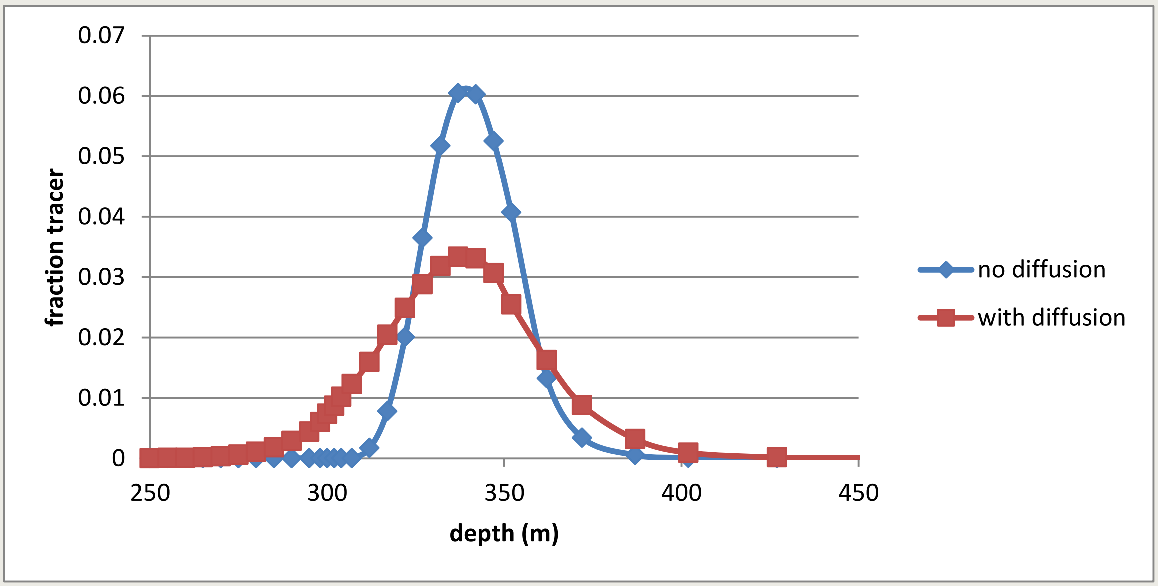

Figure 8.12. Distribution of the tracer as a function of depth for the case with advection only (no diffusion) and with both advection and diffusion (with diffusion) in a column in the middle of the model after 245,000 years.

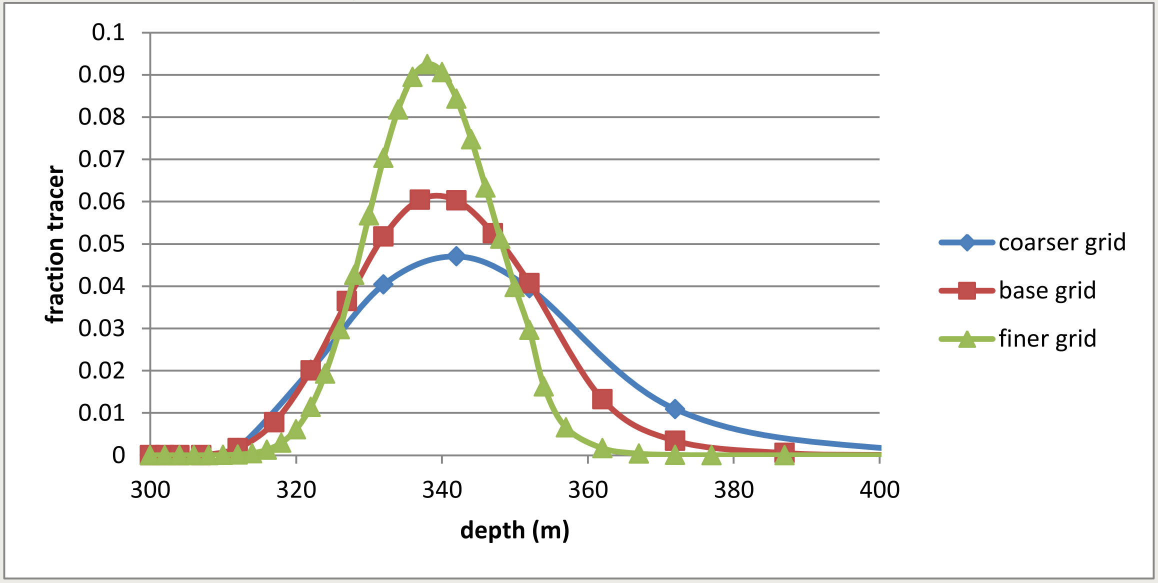

Figure 8.13. Distribution of the tracer as a function of depth for the case with advection only for a coarser and finer grid compared to the grid in Figure 8.12. Values shown in a column in the middle of the model after 245,000 years.

Mazurek et al. (2011) studied natural tracer profiles in several argillaceous rocks. The studied profiles are the result of transport in low-permeability media with evolution times in the range of hunderd thousands to a few millions of years. They found that the profiles can be well-explained by diffusion alone where the possible contribution of advection is small. Chemical osmosis was not considered by the authors, which is the topic of the next chapter.

8.4. Conclusions

The overall conclusion of this chapter is that reactive transport in the Rupel Clay may be influenced by a small advective flux in addition to a diffusive flux. However, few field data is available about hydraulic head under the Rupel Clay: those that exist are for the southern part of the Netherlands. The data must be corrected for salinity because the screens are positioned in saline or brackish aquifers. After correction, the difference in hydraulic head turns out to be 9 m at one well with higher head under the Rupel Clay. Upward advective flow will thus happen at such sites: a pore water velocity of 0.1 mm/y was calculated for estimated vertical hydraulic conductivities.

The impact of faulting was calculated for a situation where an off-set exists of several tens of meters between two blocks with a 100 m thick clay layer. The short-circuit flow that may arise for such a situation does not extend beyond a few hundreds meters away from the fault. Farther away, any advective flow is thus basically vertical. It may also be noted that conductive faults can reduce pressure build-up and thus flow through the Rupel Clay on the larger scale.

9. Osmotic groundwater fluxes through the Rupel Clay

9.1.Introduction

As discussed, clay layers are being investigated as a possible host rock for disposal of radioactive waste. In the Netherlands, the Rupel Clay Formation is a potential candidate for this purpose. One of the requirements is that groundwater flow through the clay layer must be sufficiently small. An important characteristic of clay layers is that transport properties like the intrinsic permeability and the diffusion coefficient are very small. This drastically reduces solute transport within these layers. Often, only groundwater fluxes induced by pressure gradients are considered. However, there are other driving forces in subsurface water flow. One of these is flow due to salt concentration gradients or chemical osmosis, which will be investigated in this study.

Clay layers may act as semi-permeable membranes in which chemical osmosis occurs: fluid flow is induced by salt concentration gradients while the associated transport of dissolved ions is limited because of the repulsive, electric force of the clay minerals. Uncharged radionuclides are not stopped by the semi-permeable membrane like the water molecules themselves. The occurrence of chemical osmosis is thus relevant to consider for the safety function of the clay barrier. Salt concentration gradients can occur for example when a clay layer separates an aquifer containing freshwater and another aquifer containing old seawater. When only hydraulically-driven flow is considered, the fluid flux might be underestimated in these cases. The magnitude of the groundwater flux induced by chemical osmosis must be investigated in order to determine if it is negligible or not.

In this study, the magnitude of the osmotic flux is investigated by solving the governing equations numerically using the finite element method and applying it to the situation of the Rupel Clay as typically found in the Netherlands. Experimental and modelling research on chemical osmosis in the Belgium Boom Clay was performed by Garavito (2007), who showed the act of this process for this clay unit at short time scale.

9.2.Model Description

In this chapter, the model equations, parameters and boundary conditions will be described. When referring to the salt mass fraction, the chloride-concentration is meant. Other anions are present in seawater and brine, but chloride is the most abundant.

9.2.1. Equations

The derivation of the equations used in the model is shown in Appendix 2. The final set of equations which will be solved numerically are summarized here.

Fluid flux:

$$\bar{q} = -\frac{\kappa}{\mu}\left(grad\ P - \sigma \mathrm{vRT\rho\ grad\ \omega}\right) \qquad \text{Eq. 19}$$

Fluid mass balance:

$$S\frac{\partial P}{\partial t} + div\ \bar{q} + \ \beta \bar{q}\ grad\ P = 0 \qquad \text{Eq. 20}$$

Solute mass balance:

$$n\frac{\partial \omega}{\partial t} + S\omega\frac{\partial P}{\partial t} + (1-\sigma) * \mathrm{div}\ (\rho\bar{q}) + (1-\sigma) * \beta\omega\bar{q} * grad\ P - div(D\ grad\ \omega) - D\beta\ grad\ \omega\ grad\ P = 0 \qquad \text{Eq. 21}$$

These equations will be solved using the finite element method in the commercial software COMSOL. The model will be solved for a 1-dimensional case.

9.2.2. Scenarios

The domain consists of a clay layer with a thickness of 100 m. The timescale of decay of radioactive waste is large. Therefore, the pressure, flux and concentration evolution over 100.000 years is calculated. This time period was chosen to indicate the relevance of the process at the geological time scale. Four different scenarios have been considered, which will be briefly discussed here.

Scenario 1A – Freshwater/seawater

In this scenario, the top of the clay layer is assumed to be in contact with freshwater while the bottom is in contact with seawater. Potential flow of water will thus be downwards. It is assumed that the concentration at both boundaries is constant, so that Dirichlet boundary conditions can be used for the concentration. For the chloride-concentration in freshwater, the concentration in natural Rhine Water is used, which equals 20 mg/L. The chloride-concentration in seawater is taken as 19.000 mg/L. The clay layer is initially filled with seawater. There is no hydraulic gradient induced, the initial pressure is set to zero and zero-flux boundary conditions are used for the pressure.

Thus the initial conditions:

$$\omega(x,0) = 0.019$$
$$P(x,0) = 0$$

The boundary conditions are:

$$x = 0 \quad \begin{cases} \omega(0,t) = 0.00002 \\ \dfrac{\partial P}{\partial x} = 0 \end{cases}$$
$$x = 100 \quad \begin{cases} \omega(100,t) = 0.019 \\ \dfrac{\partial P}{\partial x} = 0 \end{cases}$$

Scenario 1B – Freshwater/seawater with existing pressure gradient

This scenario is the same as scenario 1A, except that now a hydraulic head difference of 20 m is applied to the domain. In order to induce the hydraulic head difference, a constant pressure has been set at both boundaries, so that $\Delta\frac{P}{\rho g}$ equals 20 m, where the pressure is highest at the bottom of the clay layer. The hydraulic pressure gradient that induces advection is thus opposite to the osmosis gradient. A pressure of 0 Pa is assigned to the top of the clay layer. Using g = 9.81 m s^{-2} and ρ = 1000 kg m^{-3}, the pressure at the bottom of the aquifer should be equal to 196,200 Pa. The pressure between these points is then linearly interpolated.

The initial conditions are:

$$\omega(x,0) = 0.019$$
$$P(x,0) = 1962x$$

The boundary conditions are:

$$x = 0 \quad \begin{cases} \omega(0,t) = 0.00002 \\ P(0,t) = 0 \end{cases}$$
$$x = 100 \quad \begin{cases} \omega(100,t) = 0.019 \\ P(100,t) = 196200 \end{cases}$$

Scenario 2A - Seawater/brine

In this scenario, the top of the clay layer is in contact with seawater, having a chloride-concentration of 19.000 mg/L. The bottom of the clay layer is in contact with a brine, which has a chloride-concentration of 70.000 mg/L. The clay layer is initially filled with seawater. The thickness of the clay layer is 100 m. There is no hydraulic gradient induced.

Thus, the initial conditions are given by:

$$\omega(x,0) = 0.019$$

$$P(x,0) = 0$$

The boundary conditions are:

$$x = 0 \quad \begin{cases} \omega(0,t) = 0.019 \\ \dfrac{\partial P}{\partial x} = 0 \end{cases}$$

$$x = 100 \quad \begin{cases} \omega(100,t) = 0.070 \\ \dfrac{\partial P}{\partial x} = 0 \end{cases}$$

Table 9.1. Values of parameters used in the model.

Parameter	Symbol	Value	Source
Ideal gas constant	R [J mol^{-1} K^{-1}]	8.314	Constant
Absolute temperature	T [K]	288	Assumed
Dissociation coefficient	v [-]	1	Derived
Fluid compressibility	ß [Pa^{-1}]	4.6*10^{-10}	Assumed
Dynamic viscosity	μ [Pa s]	8.94*10^{-4}	Assumed
Intrinsic permeability	κ [m^2]	10^{-18}-10^{-19}	Verweij et al. (2016)
Porosity	n_0 [-]	0.4	Verweij et al. (2016)
Effective diffusion coefficient	D [m^2 s^{-1}]	5*10^{-12}	Rousseau-Gueutin et al. (2008)
Storage parameter	S [Pa^{-1}]	10^{-7}	Assumed
Reflection coefficient	σ [-]	0.05 - 0.20	Rousseau-Gueutin et al. (2008)

Scenario 2B - Seawater/brine with existing pressure gradient

This scenario is the same as 2A, except that now a hydraulic head difference of 20 m is induced. Thus, a constant pressure has been set at both boundaries, so that $\Delta \frac{P}{\rho g}$ equals 20 m, where the pressure is highest at the bottom.

The initial conditions are:

$$\omega(x,0) = 0.019$$

$$P(x,0) = 1962x$$

The boundary conditions are:

$$x = 0 \quad \begin{cases} \omega(0,t) = 0.019 \\ P(0,t) = 0 \end{cases}$$

$$x = 100 \quad \begin{cases} \omega(100,t) = 0.070 \\ P(100,t) = 196200 \end{cases}$$

9.2.3. Parameters

The parameter values for flow and transport properties have either been assumed or taken from the literature. The parameters used in the model are summarized in Table 9.1. It is worth pointing out that the reflection coefficient for the Belgium Boom Clay was found to be 0.41 at 0.014 M $NaHCO_3$ and 0.07 at 0.14 M $NaHCO_3$ (Garavito et al., 2007).

9.3.Results and discussion

9.3.1. Scenario 1A

In this scenario, an intrinsic permeability of 10^{-18} m^2 is used. Figure 9.1 shows the long-term pressure evolution in the clay layer. The pressure increases over time, however, the rate of increase becomes smaller over time. The location of the pressure drop, e.g. located at x = 70 m for t = 100,000 years, corresponds with the concentration gradient in Figure 9.2. This result does not match that of the Keijzer experiment (Keijzer et al., 1999). In this experiment, the pressure increased at first, but decreases after a certain amount of time. The difference is explained by the boundary conditions. The Keijzer experiment had zero-flux boundary conditions for the concentration. In that scenario, a uniform salt distribution will be obtained eventually. This would remove the concentration gradients and therefore the effect of chemical osmosis, which in turn would decrease the pressure. Constant concentration boundaries are used in this model and thus a concentration gradient will always exist.

The evolution of the specific discharge is shown in Figure 9.3. The specific discharge is not constant in space, since we assumed that the fluid density and porosity are a function of pressure. Excess water is stored inside the porous medium, which corresponds with the results in Bader and Kooi (2005). The flux is negative, which means that it is directed downwards. Thus, water flows from the top, containing freshwater, to the bottom, containing seawater. This is as expected, as osmosis causes a flow of water from regions of low concentration to regions of high concentration.

The specific discharge through the clay layer decreases over time, because the concentration gradients becomes less steep over time (Figure 9.2). Because of the downwards osmotic flux, freshwater is transported into the clay layer. The maximum value that the specific discharge reaches is approximately $8*10^{-12}$ m/s. Using an average porosity of 0.4, this would mean a maximum pore water velocity of $2*10^{-11}$ m/s (or 0.63 mm/y). Thus, it would take 79,000 years to travel 50 m and the importance of osmosis cannot be neglected at the long time scale.

Figure 9.4 shows the pressure profile after 100,000 years for different values of the reflection coefficient. Less selective membranes cause a higher pressure in the clay layer. However, the pressure gradient within the clay layer is smaller for such membranes. The pressure evolution is also shown in Figure 9.5, which shows the pressure evolution at x = 99 m, being located near the bottom of the clay layer. For higher reflection coefficients, the pressure approaches a constant value. For lower values for the reflection coefficient, the pressure keeps increasing. However, it is assumed that it will approach a constant value, but it will take a longer time because the fluxes are smaller.

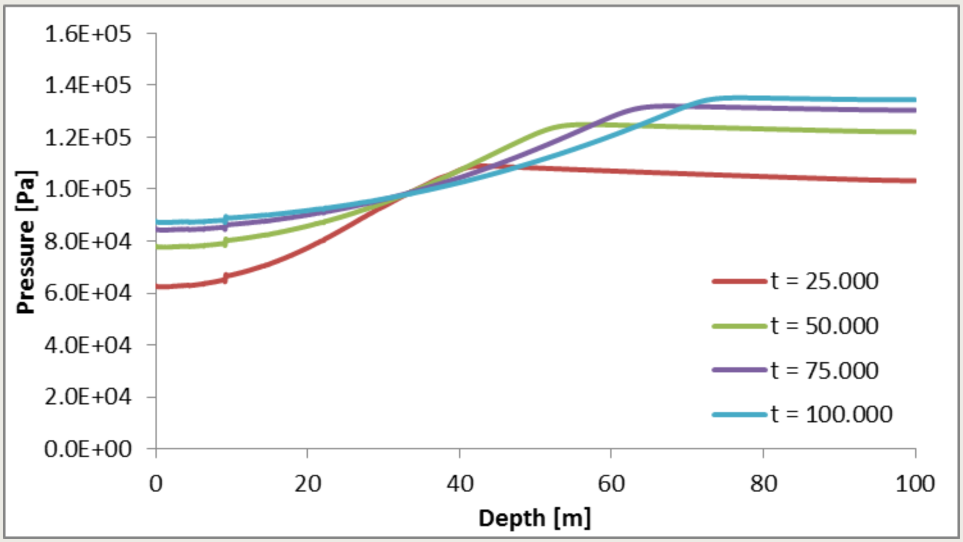

Figure 9.1. Change of the pressure profile in time (in years) for σ = 0.20.

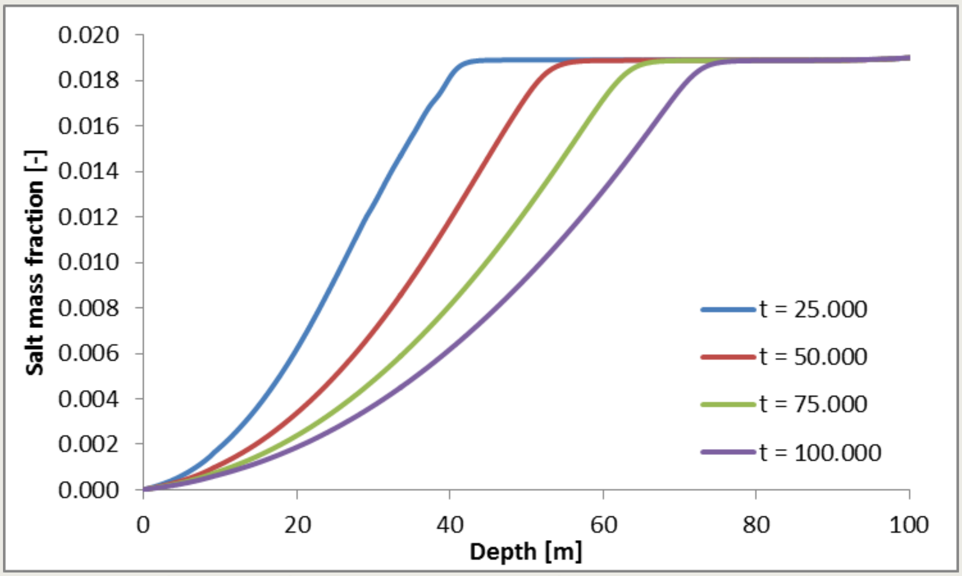

Figure 9.2. Change of the concentration profile in time (in years) for σ = 0.20.

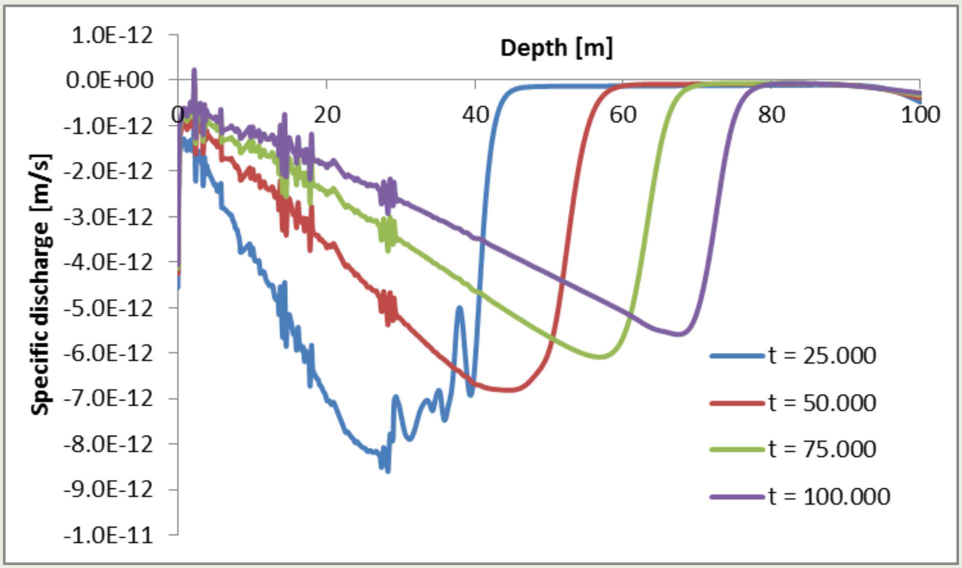

Figure 9.3. Change of the specific discharge through the clay layer in time (in years) for σ = 0.20.

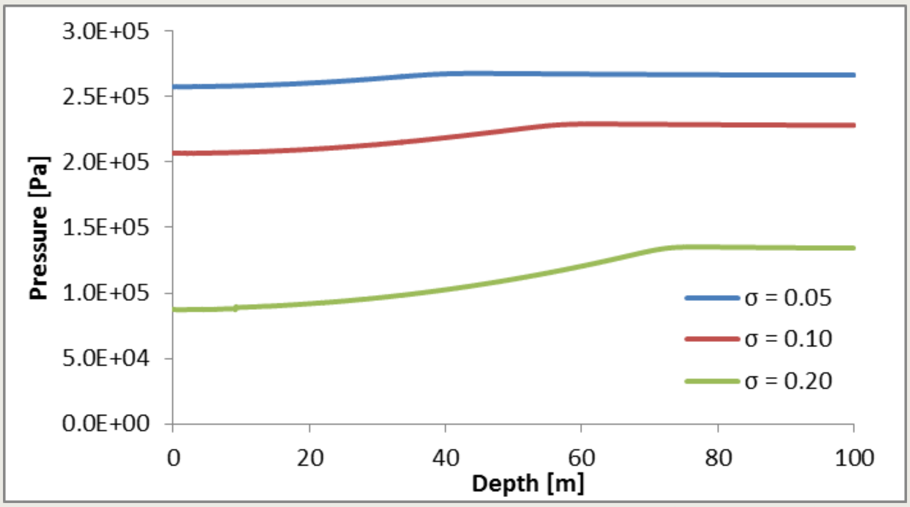

Figure 9.4. Pressure profile at t = 100,000 years for different values for the reflection coefficient.

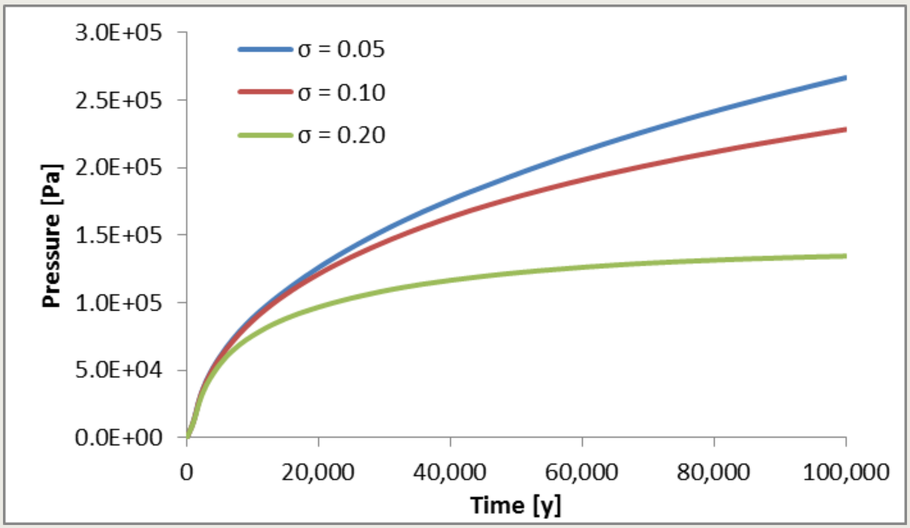

Figure 9.5. Pressure evolution at x = 99 m at t = 100,000 years for different values for the reflection coefficient.

High values for the reflection coefficient correspond to more ideal semi-permeable membranes. It is interesting to note that the solute transport is faster for more ideal semi-permeable membranes. This seems counter-intuitive, as transport of salt is hindered by the semi-permeable membrane. However, if the semi-permeability of the membrane increases, so will the osmotic fluid flux. Therefore, more salt will be transported by advection (Figure 9.6). This explanation is reinforced by Figure 9.7. The specific discharge through the clay layer is higher for clay having a higher reflection coefficient.

The osmotic Peclet number for a reflection coefficient of 0.2 equals 10.4, while for a reflection coefficient of 0.05 it equals 1.9. This means that advection is the dominant transport process for both cases. Advective flow of water becomes increasingly important for higher values of the reflection coefficient and dissolved compounds become dragged with this flow. The non-ideality of the membrane plays its role here, too.

Assuming a reflection coefficient of 0.2, the mean flux through the clay layer equals 2.4×10^{-12} m s^{-1}. Using a porosity of 0.4, this can be calculated to obtain a mean flow velocity of 6.0×10^{-12} m s^{-1}. Assuming a travel distance of 50 m, the time it would take for solutes to travel out of the clay layer is approximately 263,000 years. It should be noted that these figures only show the specific discharge after 100,000 years. As mentioned in the previous section, the specific discharge decreases over time, because the concentration gradient is largest at the start of the simulation. The initial specific discharge can be up to 10 times larger than shown in Figure 9.3, but approaches the values of Figure 9.3 within a few thousands of years. Thus, this calculation underestimates the flow velocity.

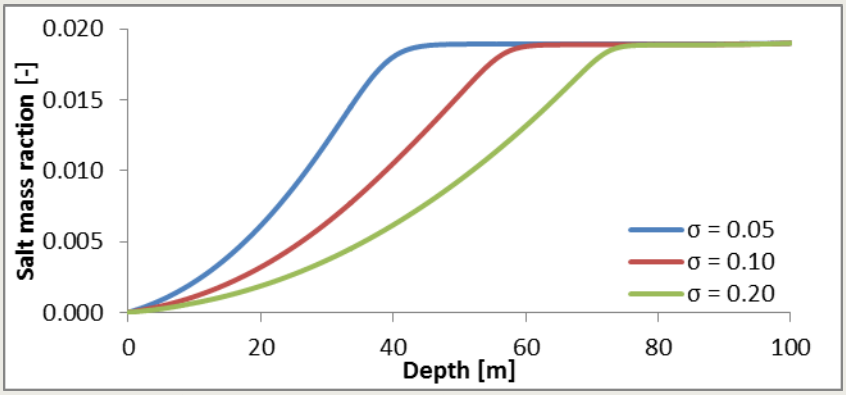

Figure 9.6. Salt mass fraction profiles at t = 100,000 years for different values for the reflection coefficient.

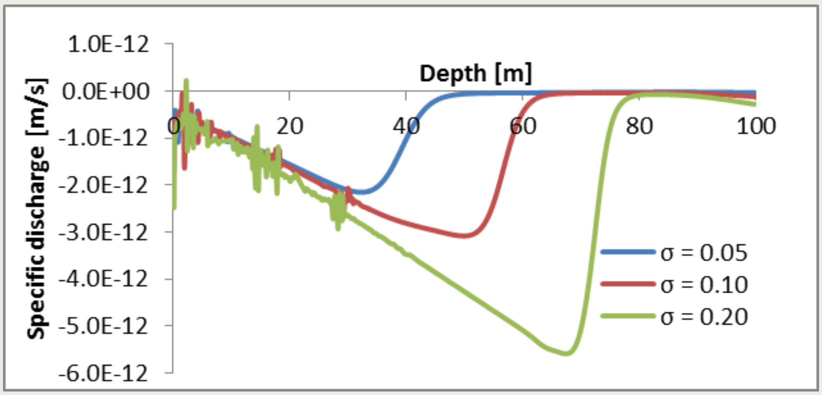

Figure 9.7. Specific discharge through the clay layer at t = 100,000 years for different values for the reflection coefficient.

9.3.2. Scenario 1B

It can be observed from Figure 9.8 that the pressure does not change as much as in the previous scenario, where no pressure gradient was induced. The salt concentration shows the same evolution as when no pressure gradient is induced (Figure 9.9): freshwater is transported into the clay layer. This means that the flow direction is downwards, even though the pressure gradient induces an upward advective flow of water. This is illustrated in Figure 9.10, where the fluid flux through the clay layer is shown. This shows an upwards flux in the part where the flux is driven by the hydraulic pressure gradient. In the upper zone of the clay layer, a concentration gradient exists, which causes a downwards fluid flux due to chemical osmosis. The flux due to chemical osmosis is larger than the hydraulic flux. Again, the osmotic flux decreases over time as the concentration gradient becomes smoother. Thus, even though the pressure gradient induces an upward flow of water, the osmotic flow is larger and the groundwater flow is directed downwards in the upper part.

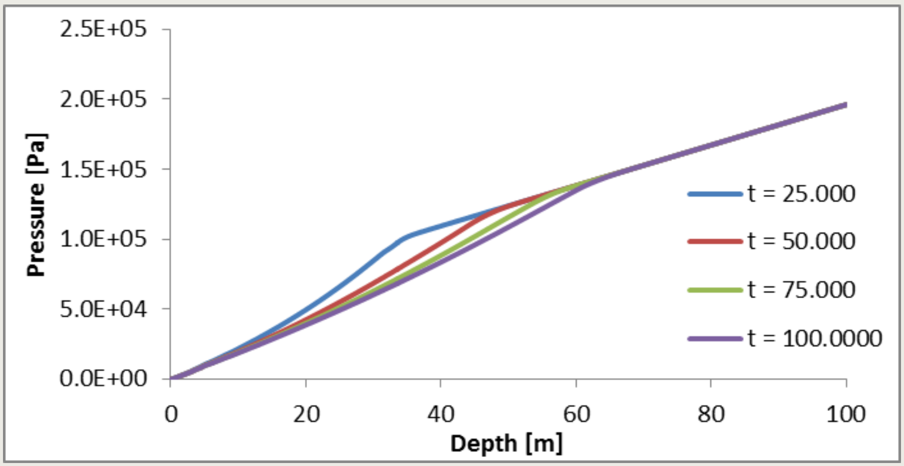

Figure 9.8. Pressure evolution for σ = 0.20.

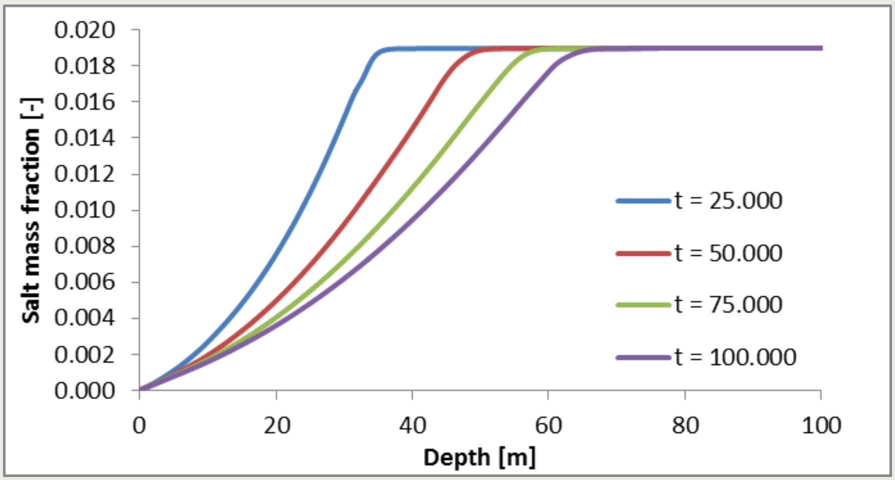

Figure 9.9. Concentration evolution for σ = 0.20.

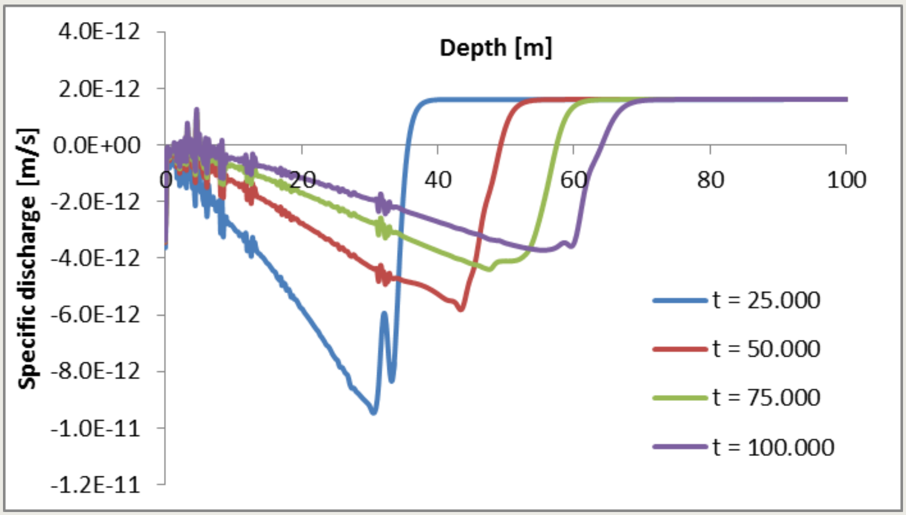

Figure 9.10. Temporal evolution (in years) of the specific discharge for σ = 0.20.

Figure 9.11 shows the pressure profile for varying degrees of semi-permeability of the clay layer. The pressure profile does not alter too much from the existing linear pressure gradient. The pressure difference is only around 10,000 Pa at maximum. In the previous scenario, when no pressure gradient was present, the difference between the degrees of semi-permeability was over 100,000 Pa in some cases. Figure 9.12, shows that freshwater is transported downwards. This corresponds with the downwards flux caused by osmosis. Figure 9.13, shows the fluxes for different reflection coefficients: again, the water is transported downwards by osmosis, while the pressure gradient creates an upward flow. Here, it becomes clear that the osmotic flux increases strongly with higher reflection coefficient. The osmotic flux is $4*10^{-12}$ m/s at most for the upper value of the reflection coefficient, while the hydraulic upward flux is half of that. The effects of chemical osmosis should be considered in this scenario.

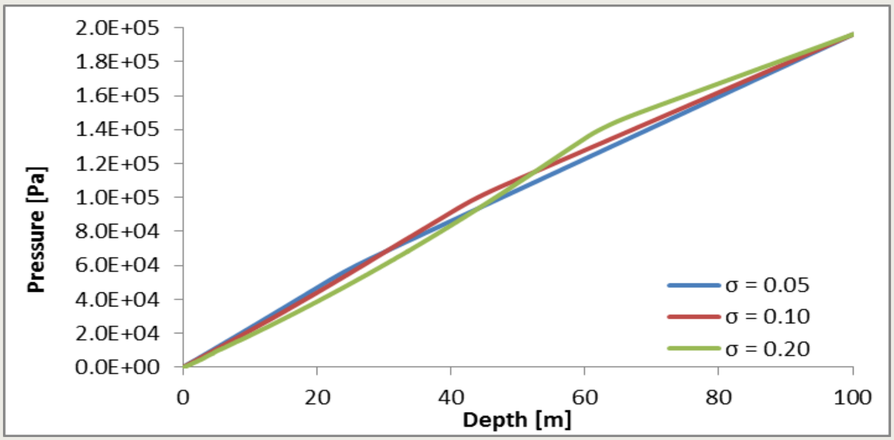

Figure 9.11. Pressure profile for varying degrees of semi-permeability at t = 100,000 years.

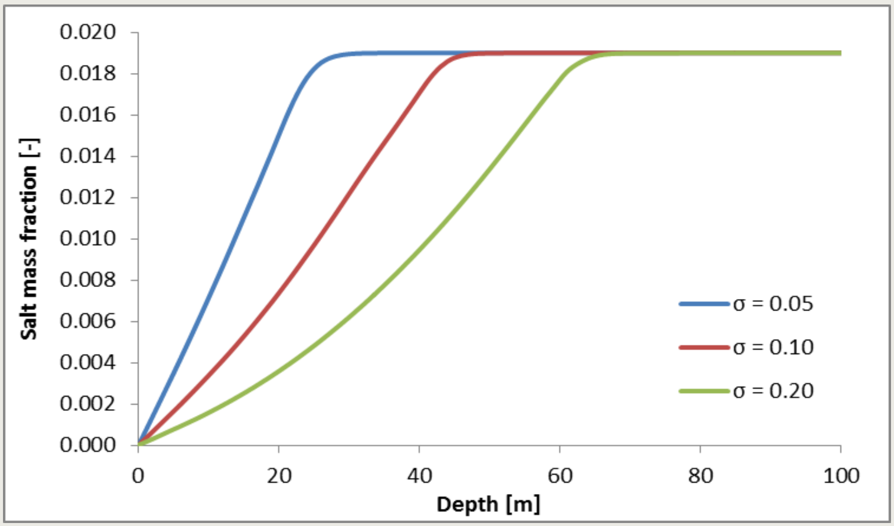

Figure 9.12. Concentration profile for varying values of the reflection coefficient at t = 100,000 years.

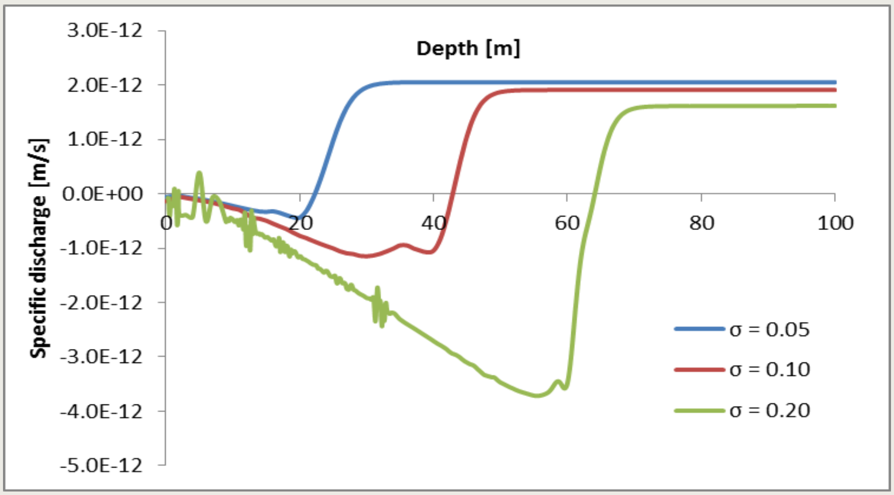

Figure 9.13. Specific discharge for different values for the reflection coefficient at t = 100,000 years.

9.3.3. Scenario 2A

In this scenario, the osmotic flux between seawater and brine is investigated. The concentration difference is larger than in the previous scenario and thus the osmotic flux will also be larger. It is believed that this causes numerical instability in the model. The model has trouble converging, and the salt mass fraction can become negative or larger than unity, which are both not physically possible. In order to refrain this from happening, the osmotic flux has been decreased by lowering the semi-permeability and the intrinsic permeability of the clay layer. Lower semi-permeability can also be expected for more saline groundwater environments. The intrinsic permeability is reduced to $1*10^{-19}$ m^2, which still falls within the range reported in Verweij et al. (2016) and suggests a deeper burial depth. In the following figures, a reflection coefficient of 0.02 is used.

The pressure profile is shown in Figure 9.14. In this case, the pressure is higher at the top of the clay layer. In this case, the clay layer is initially saturated with the less saline water. This changes the location of the concentration gradient and alters the pressure evolution. Also, the pressure gradient is larger in this scenario.

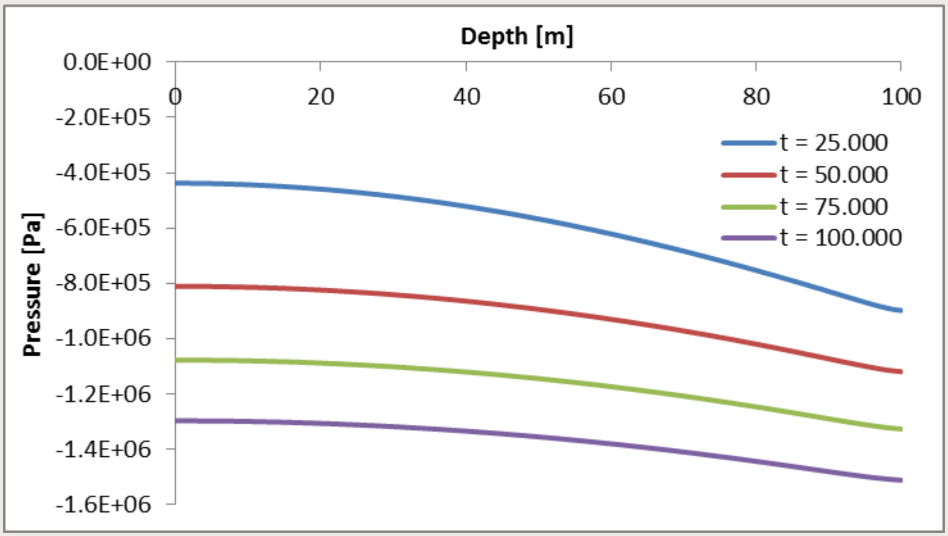

Figure 9.14. Pressure profile evolution (in years) for σ = 0.02.

The specific discharge is shown in Figure 9.16. In most areas, the flux is smaller than $1*10^{-12}$ m/s, except at the bottom of the clay layer, near the sharp concentration gradient, where it reaches values similar to the first scenario. However, the reflection coefficient and the intrinsic permeability have been lowered in this scenario by a factor of 10. For higher values of permeability and semi-permeability, the specific discharge is estimated to be $1*10^{-10}$ m/s. However, the model does not converge when using these values and thus this has not been tested.

The concentration profile is shown in Figure 9.15. The transport of salt is slower than in the first scenario, which is explained by the smaller fluid flux and thus less chloride being transported by advection. The intrusion of brine in the clay layer is limited to 10-15 m for a period up to 100,000 years. For a larger reflection coefficient and permeability, more solute will be transported because of the larger advective flux.

The osmotic Peclet number equals 4.8 using a reflection coefficient of 0.02 and an intrinsic permeability of 10^{-19} m^2. A larger reflection coefficient would probably lead to larger pressure differences. Additionally, the intrinsic permeability is also lowered in this scenario. The osmotic Peclet number would be larger if the same parameter values were used as in the previous scenario. Since the osmotic Peclet number is larger than unity, advection by the osmotic water flux is the dominant transport mechanism.

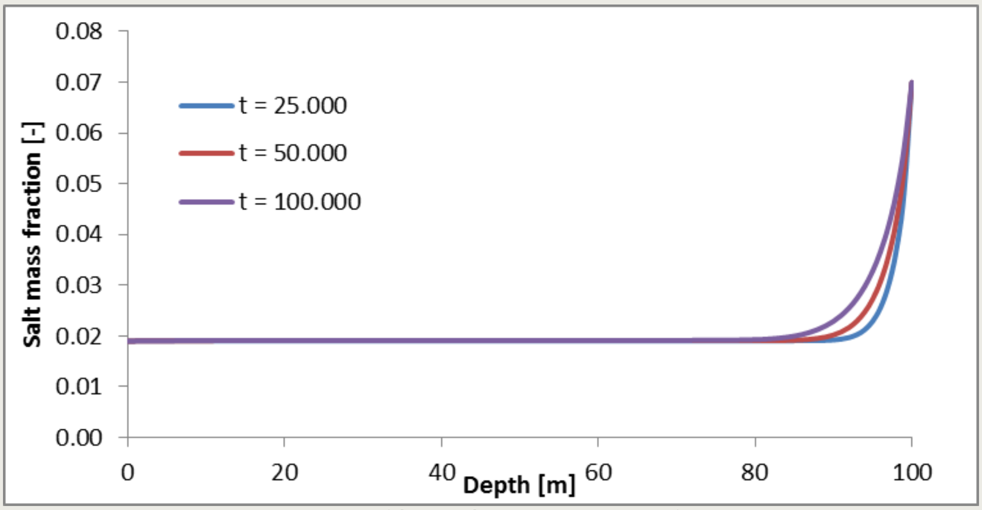

Figure 9.15. Concentration profile evolution (in years) for σ = 0.02.

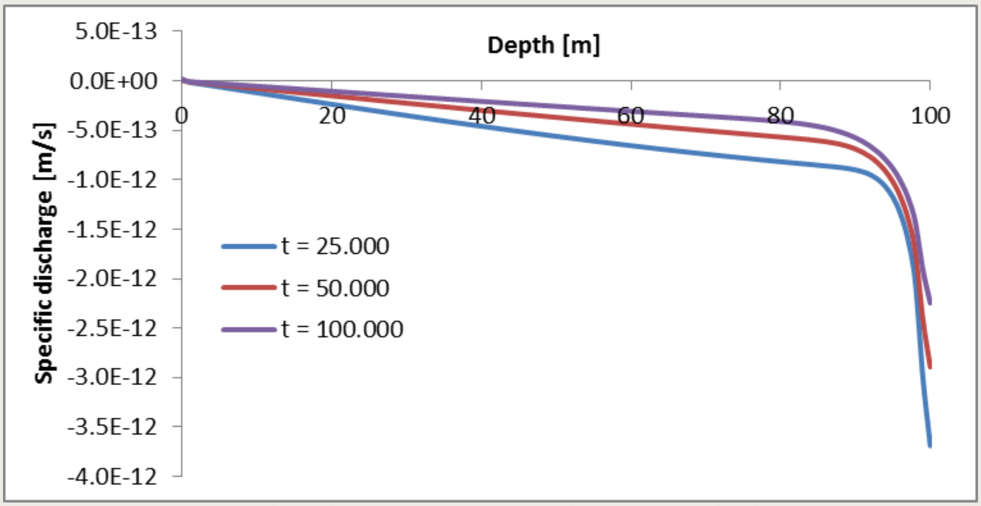

Figure 9.16. Temporal evolution (in years) of the specific discharge in time for σ = 0.02.

9.3.4. Scenario 2B

In this scenario, the pressure profile barely changes over time, as can be seen in Figure 9.17. Thus, the pressure profile remains almost linear, which causes a hydraulic flux in upward direction. There is a slight alteration of the pressure profile near the bottom of the clay layer, where the concentration gradient is present. Brine is transported upwards (Figure 9.18). Since osmosis induced a downward flow, this must be caused by the hydraulic upward flux. The intrusion of brine is also limited to the first 20 m for a period up to 100,000 years, thus it is still a slow process.

At the bottom of the clay layer, the water flux is directed downward due to the concentration gradient (Figure 9.19). In the rest of the clay layer, the fluid flux is directed upwards because of the pressure gradient. The osmotic flux is 3 to 8 times larger than the hydraulic flux. For a larger reflection coefficient, this difference could be even larger. However, the osmotic flux does decrease over time as the concentration gradient becomes smaller. The effects of chemical osmosis should be considered when such large concentration gradients are present, e.g. brine and seawater. The flux would be even larger for brine and freshwater.

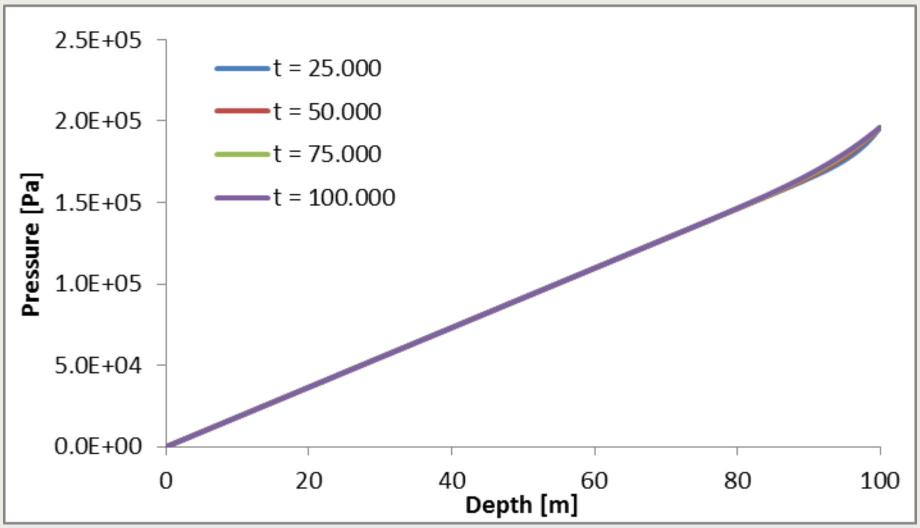

Figure 9.17. Pressure profile evolution (in years) for σ = 0.02.

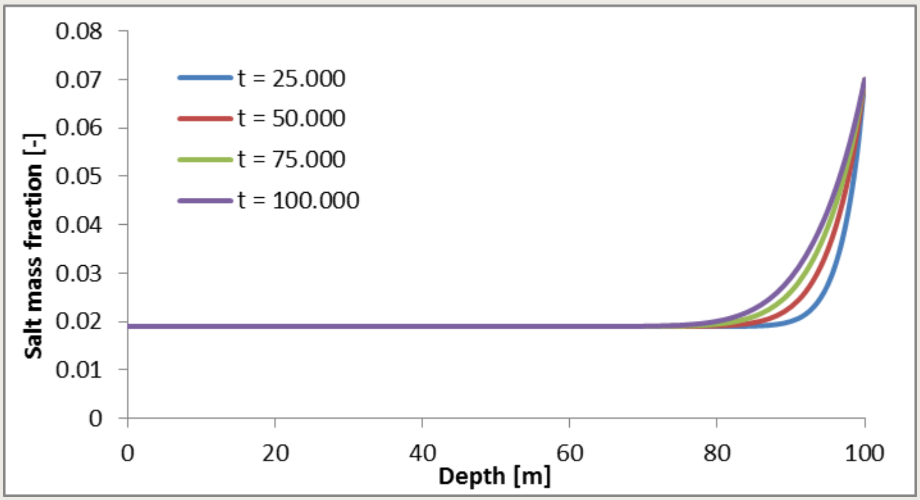

Figure 9.18. Evolution of the concentration profile in time (in years) for σ = 0.02.

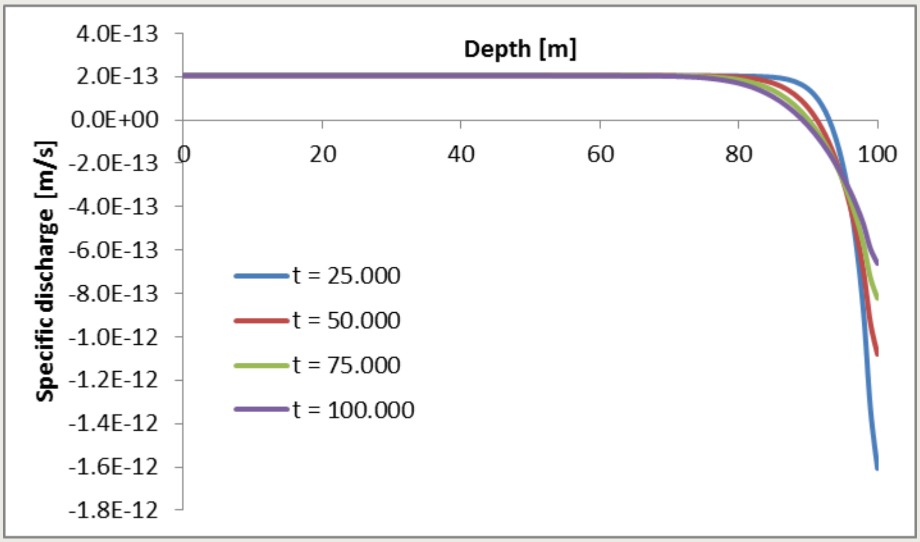

Figure 9.19. Temporal evolution (in years) of the specific discharge for σ = 0.02.

9.4. Conclusions

Clay is investigated as a potential geo-material for disposal of radioactive waste due its low permeability. Often, only pressure-driven groundwater flow is considered. Secondary effects which cause flow are assumed negligible. However, secondary effects might be significant in some scenarios. In this study, the fluid flux by chemical osmosis is investigated. This flux is caused by salt concentration gradients across the clay layer. The clay layer acts as a semi-permeable membrane, as water is able to flow through, but anions are repelled due to the negatively charged clay minerals. The magnitude of the flux depends on the degree of semi-permeability of the clay.

Darcy’s law has been extended to include the effects of chemical osmosis. This equation is solved together with the fluid mass balance and salt mass balance equations. The equations have been solved in COMSOL using the finite element method. Two different scenarios have been investigated. In the first scenario, the clay layer separates freshwater from seawater. In the second scenario, the clay layer separates seawater and brine. Both cases may be relevant at the geological time scale for the Rupel clay layer in the Netherlands. Additionally, the osmotic flux was investigated when a pressure head difference of 20 m was present between the top and bottom of the clay layer. This mimics a situation where aquifers under the clay layer are over-pressurised as probably holds for the Rupel clay layer in the Netherlands (cf. Chapter 8).

The osmotic flux has been proven to be relevant for both scenarios. Here, it must be remembered that porosity changes due to osmotic flow were enabled in the modelling exercise; whether this is geomechanically realistic at several hunderds meters depth has not been verified. In the freshwater-seawater scenario, the magnitude of the osmotic flux is up to twice as large as the hydraulic flux. In the seawater-brine scenario, the osmotic flux is 3 to 8 times larger than the hydraulic flux. It has the potential to be even larger, as only a small value of the reflection coefficient was used in this scenario. It is recommended to investigate the brine-seawater scenario further with slightly higher and probably more realistic values for the reflection coefficient.

10. General Discussion

This study characterises the geochemical development of the Rupel Clay in a generic way using geochemical and hydrological modelling. The development of the Rupel Clay is considered for different scenarios:

- The long-term autonomous geochemical evolution of the Rupel Clay
- The geochemical evolution under the conditions of a gallery
- The geochemical evolution at the interface between an engineered barrier system (EBS) and the Rupel Clay
- The likelihood or not of advective flow or chemical osmosis in addition to molecular diffusion as reactive transport controls

This development is relevant within the framework of the environmental safety function that the Rupel Clay would play as an impermeable barrier. The Rupel Clay fulfills the long term safety function '**transport and retention**' (Verhoef & Schröder, 2011). This means that the Rupel Clay layer should provide hydrological isolation and attenuate the transport of released radionuclides. The environmental safety function of the Rupel Clay is determined by hydrogeological and geochemical factors. Both factors have been studied here: 1. the geochemical results suggest that reaction zones by disturbances are limited to a few meters and 2. the hydrogeological results ask attention for the likelihood of other transport processes than diffusion.

10.1. *Hydrological uncertainties and limitations*

The main uncertainty seems to be associated with the hydrogeology: what is the permeability of the Rupel Clay, what are the hydraulic gradients across this unit and what is its osmotic efficiency. The calculations performed bring forward that advective and osmotic transport may be relevant processes under Dutch conditions at a comparable size as diffusive transport. Depending on the boundary conditions, flow may be into or out of the Boom Clay which may enhance or diminish the environmental safety function. The direction of flow is also highly important: upward flow may shorten travel times compared to single diffusion.

The act of advective and osmotic flow has immediate repercussions for reactive transport: an additional transport mechanism may enhance the reactive zones. Oxidation of the Rupel Clay is, for example, determined by the inflow of oxidant (such as dissolved oxygen) when oxidizing conditions become present at the edge of the clay. The latter is not self-evident but depends on the impacts of glaciations. As long as the groundwater velocity stays below 0.1 mm/y no major differences are present when compared to diffusion alone. As soon as it rises to 1 mm/y, the additional transport processes become more dominant even more in the long run as advective transport increases linearly with time whereas diffusive transport increases with the square root of time.

Little hydrological monitoring has been performed on the Rupel Clay and the adjoining geological units are neither well studied in particular the one below. Few monitoring wells exist that contain observation screens underneath the Rupel Clay (even for the regions where it lies at shallow depth as Zeeland and eastern Netherlands). Field verification on the importance of advection or chemical osmosis is therefore practically hard if not impossible at present.

10.2. *Geochemical uncertainties and limitations*

No large geochemical changes of the Rupel Clay are expected at a time scale of 1 million years without natural or man-induced perturbations. Potentially relevant factors that were assessed are: oxidation, clay weathering, organic matter degradation, microbially mediated conversion, cation exchange and clay swelling. A large unknown is whether H_2 production is substantial near the Engineered Barrier System (majorly due to corrosion) and will disturb the geochemical condition of the Rupel Clay by initiating biogeochemical redox processes. This was not addressed in any of the modelling scenarios.

The major external factor potentially causing changes of the Rupel Clay is formed by glacial events, and most specifically postglacial erosion. This might lead to exposure to oxygenated surface water and, due to pressure differences, advective flow, which will cause geochemical reactions. The geochemical data available for the Rupel Clay indicates that the carbonate buffering on pyrite oxidation will usually be sufficient as Ca-carbonate is stoichiometrically more present than pyrite.

We assumed that the Rupel Clay remains saturated under these scenarios. This results into a major limitation on reactive transport: diffusion is the major transport mechanism, possibly with chemical osmosis and limited advection. In case of unsaturated conditions, cracks may establish in the clay causing enlarged exposure of deeper clay to air with all associated geochemical processes of oxidation.

The importance of saturated versus unsaturated conditions also plays a role for the mine galleries and related engineered barrier system. It has become clear that oxidation of clay as host rock happens by aeration via the mine galleries. The size and extent of fissures and fractures is uncertain for the Rupel Clay buried at several hunderds meters below surface. The related unsaturated zone through which transport of gases is much easier than as dissolved gas in groundwater is also uncertain. The ductile behaviour of the Rupel Clay is likely different from the Boom Clay in Belgium and other well studied argillaceous rocks.

We made a gross simplication in modelling proton-buffering of the clay following changes in pH. The modelling scenarios indicate that considerable shifts in pH may occur. Here, it is unknown what the proton-buffering characteristics of the Rupel Clay are in two different ways: buffering due to protonation/deprotonation of sorption sites and due to CO_2 production related with slow mineralisation of sedimentary organic matter or not. Observational studies are needed in addition to a more sophisticated modelling approach.

A general uncertainty of the Dutch Rupel Clay is its pore water composition. Very limited insight exists on this (Behrends et al., 2016) and rather limited insight exists for the groundwater composition under the Rupel Clay as well (Griffioen et al., 2015; 2016). The Boom Clay in Mol contains fresh pore water while groundwater above the Rupel Clay seems to be generally saline in the Netherlands. This implies that there must be a saline – fresh water interface *within* the Rupel Clay in - presumably - the southern Netherlands. Related uncertainties are the redox reactivity of sedimentary organic matter and presence or not of redox-sensitive species as pore water SO_4 and solid Fe(III) minerals. It is not self-evident that the conditions for the Boom Clay in Mol are representative for parts of the Netherlands.

11. Conclusions: Relevance for the Safety Case

The objective of this study is to determine what geochemical development of the Rupel Clay is expected over a prolonged time scale. This is relevant for the safety function **’transport and retention’**, that is associated with the Rupel Clay within the OPERA disposal concept for the disposal of High Level Waste in the Rupel Clay (Verhoef & Schröder, 2011). The safety functions that are attributed to the Rupel Clay layer are therefore:

- to prevent water flow and in that way provide *‘isolation’*
- to effectuate *‘delay and attenuation of the radionuclide releases’*.

More specifically, this study should provide insight in the environmental boundary conditions that the Rupel Clay provides for the fate of radionuclides. It should:

- give an analysis of processes that may impair retrievability over a time span of <100 years.
- give an analysis of processes that may impair long term safety function “transport and retention”
- include a discussion on distribution of parameter values.

The first two topics are discussed below. The last is discussed in the previous chapter where attention is also paid to process uncertainty and modelling limitations.

11.1. Processes that may impair retrievability over time span of <100 years

The retrievability of radioactive waste from a concrete based geological repository in the Rupel Clay could be compromised in case of chemical interactions that affect the structural integrity of either the concrete or clay material. From the analysis on the long term stability and weathering behavior of the Rupel Clay in chapters 6 and 7 follows that Rupel Clay and adjacent concrete/ cementitious materials will interact because of their different chemical compositions, and the possibility for exchange of reaction products via water filled pores. However, the rate of this reactant exchange is determined by diffusion and reactive transport processes and according to the calculations presented here the reactant exchange will be so slow that this will not lead to significant structural changes of either the Rupel Clay or in the concrete material with which it is in contact over the time span of interest. With regards to the safety case/ safety assessment calculations this implies that for the period up to 100 years the studied interaction processes between cementitious materials and the Rupel Clay will not lead to significant changes in either the Rupel Clay or the cementitious material and thus also are unlikely to cause an impaired retrievability. Here, we assume that H_2 generation is also sufficiently slow within the first 100 years of disposal not to cause geochemical disturbances.

11.2. Processes that may impair the long term safety function “transport and retention”

The long term safety function of Rupel Clay “transport and retention” (or, in other words, limit water transport and provide a medium for chemical retention), would be compromised if geological scenarios would have significant impact on the physical and chemical properties of the clay that determine its transport and retention characteristics. Potential future scenarios and their risk of compromising transport and retention properties are described qualitatively in Chapter 4. The numerical simulations reported in Chapter 6 show that oxidation of the Rupel Clay as a result of glaciation and erosion causes oxidation of pyrite with a corresponding decrease in pH, followed by dissolution of calcite and precipitation of hematite. As a result the mineral reactions remain limited to the first meter after 10,000 years, whereas the cation exchange effects reach down to a few meters. The partial exchange of adsorbed sodium by calcium, due to calcite dissolution, might affect the swelling potential of the smectite. Ca-smectite has a lower swelling potential, and this could cause clay shrinkage and corresponding porosity and permeability increase.

In addition to the impact of geological scenarios, the safety function would be compromised in case of significant physical and/or chemical changes of the clay matrix as a result of the interaction with cementitious materials. As concluded above, the contrasting chemical nature of cementitious materials and Rupel Clay, combined with their porosity will lead to exchange of chemicals via pore water. In the model calculations in chapter 6 this type of interaction via reactive transport is simulated. In the presented results the pH is used as an indicative chemical parameter for identification of the zone over which chemical changes take place. From this result follows that the pH changes in the Rupel Clay zone extend to a much larger distance from the boundary than those in the cementitious material. This is caused by the much higher reactivity of cementitious material (per m^3) in comparison to that of Rupel Clay.

Furthermore, the results show that for conditions at zero, or very low flow (<0.1 mm/year), the extent of the impacted zone is limited to several meters at maximum over a period of 10,000 years. This is in line with Belgian research on this topic. This implies that for a total thickness of the Rupel Clay layer of 50 m, more than 80% of the retention capability would remain unaltered and intact. This limited spatial range of affected area means that the safety functions hydraulic isolation and attenuation for a 50 m thick layer will not be significantly affected.

Because available data on hydraulic pressure gradients in the Rupel Clay zone in the Netherlands is scarce, the simulations were also performed with the condition of 1 mm/year as pore water velocity. This condition can be reached in a combination of permeability and pressure gradient that is not at all improbable. Under this condition, the pH affected zone in the Rupel Clay extended to ca. 20 m within a time span of 10,000 years. Under such conditions advection can no longer be ignored as transport process. A water flow rate of 1 mm/year may be high for Rupel Clay conditions, but currently no field data are available that support this.

The study into possible effects of osmosis on groundwater fluxes indicates that osmosis may result in water fluxes of the same order of magnitude as pure hydraulic flow rates. This further adds to the uncertainty of the flow conditions in the Rupel Clay.

12. References

Anderson, R.L., Ratcliffe, I., Greenwell, H.C., Williams, P.A., Cliffe, S. & Coveney, P.V. (2010). Clay swelling — A challenge in the oilfield. Earth-Science Reviews, 98, 201–216.

Appelo, C.A.J. & Willemsen, A. (1987). Geochemical calculations and observations on salt water intrusions. I. A combined geochemical / mixing cell model. Journal of Hydrology, 94, 313-330.

Appelo C.A.J. & Postma D. (2005). Geochemistry, Groundwater and Pollution . A.A. Balkema Publ., 2nd ed., Leiden, The Netherlands, 649 p.

Arcos, D., Grandia, F., Domenech, C., Fernandez, A.M., Villar, M.V., Muurinen, A., Carlsson, T., Sellin, P. & Hernan, P. (2008). Long-term geochemical evolution of the near field repository: insights from reactive transport modelling and experimental evidences. Journal of Contaminant Hydrology, 102, 196-2009.

Bader, S. (2005). Osmosis in groundwater: chemical and electrical extensions to Darcy's Law. PhD Thesis, TU Delft, Delft, The Netherlands.

Bader, S. & Kooi, H. (2005). Modelling of solute and water transport in semi-permeable clay membranes: comparison with experiments. Advances in Water Resources 28, 203-214.

Bagnoud, A., Chourey, K., Hettich, R.L., De Bruijn, I., Andersson, A.F., Leupin, O.X., Schwyn, B. & Bernier-Latmani, R. (2016). Reconstructing a hydrogen-driven microbial metabolic network in Opalinus Clay rock. Nature Communications, 7, art. no. 12770

Beets, C.J. & Beets, D.J. (2003), A high resolution stable isotope record of the penultimate deglaciation in lake sediments below the city of Amsterdam, The Netherlands. Quaternary Science Reviews, 22, 195-207.

Behrends, T., van der Veen, I., Hoving, A. & Griffioen, J. (2015). Geochemical characterization of Rupel (Boom) Clay material: pore water composition, reactive minerals and cation exchange capacity. OPERA deliverable OPERA-PU-UTR512

Behrends, T., van der Veen, I., Hoving, A. & Griffoen, J. (2016). First assessment of the pore water composition of Rupel Clay in the Netherlands and the characteristics of its reactive solids. Netherlands Journal of Geoscience, 95, 315-336.

Berger G., Lacharpagne J-C., Velde B., Beaufort D. & Lanson B. (1997). Kinetic constraints on illitization reactions and the effects of organic diagenesis in sandstone/shale sequences. Applied Geochemistry, 12, 23-35.

Boivin-Jahns, V., Ruimy, R., Bianchi, A., Daumas, S & Christen, R. (1996). Bacterial Diversity in a Deep-Subsurface Clay Environment. Applied and Environmental Microbiology, 62, 3405–3412.

Bonté D., van Weed J.-D. & Verweij J.M. (2012). Subsurface temperature of the onshore Netherlands: new temperature dataset and modelling. Netherlands Journal of Geosciences, 91(4), 491-515.

Bresler, E. (1973). Anion exclusion and coupling effects in nonsteady transport through unsaturated soils: I. Theory. Soil Science Society of America Journal, 37, 663-669.

Bruggeman, C. & De Craen, M. (2012). Rupel Clay natural organic matter. SCK•CEN Contract: CO-90-08-2214-0, NIRAS/ONDRAF contract: CCHO 2009-0940000.

Bruggenwert, M.G.M. & Kamphorst, A. (1982). Survey of experimental information on cation exchange in soil systems. In 'Soil Chemistry B. Physico-chemical models' ed. by Bolt, G.H. Elsevier, Amsterdam, p. 141-204.

Chamley, H. (1994). Clay Mineral Diagenesis. In ‘’Quantitative Diagenesis: Recent Developments and Applications to Reservoir Geology’’, eds. A. Parker & B.W. Sellwood. NATO ASI Series Volume 453, pp 161-188.

Chruchaudet, M., Croisé, J. & Lavanchy, J. M. (2008). In situ osmotic experiment in the Callovo-Oxfordian argillaceous formation at the Meuse/Haute-Marne URL (France): Data and analysis. Physics and Chemistry of the Earth, 33, 114-124.

Claret, F., Marty, N.C.M., Tournassat, C., Gaboreau, S., Burnol, A., Chiaberge, C., Munier, I, Cochepin, B., Michau, N. & Gaucher, E.C. (2007). Phreeqc modelling of concrete/clay interactions in a 2D geometry with explicit effect of porosity evolution on transport properites due to mineralogical changes. Clays in natural & engineered barriers for radioactive waste confinement 4th international meeting – March 2010 – Nantes, France.

De Craen, M., Van Geet, M., Wang, L. & Put, M. (2004a). High sulphate concentrations in squeezed Rupel Clay pore water: evidence of oxidation of clay cores. Physics and Chemistry of the Earth, 29, 91-103.

De Craen, M., Wang, L., Van Geet, M. & Moors, H. (2004b). Geochemistry of Rupel Clay pore water at the Mol site. Scientific Report SCK·CEN-BLG-990, 04/MDC/P-48.

De Craen M., Wemaere I., Labat S. & Van Geet, M. (2006). Geochemical analyses of Rupel Clay pore water and underlying aquifers in the Essen-1 borehole. External Report SCK·CEN-ER-19, 06/MDC/P-47.

De Craen, M., Honty, M., Van Geet, M., Weetjens, E., Sillen, X., Wang, L., Jacques, D. & Martens, E. (2011). Overview of oxidation around galleries in Boom Clay (Mol, Belgium) – Status 2008. SCK·CEN-ER-189, 11/MCD/P-65.

De Craen, M., Van Geet, M., Honty, M., Wang, L. & Weetjens, E. (2007). Extent of oxidation in Rupel Clay as a result of excavation and ventilation of the HADES URF: experimental and modelling assessments. International meeting Clays in natural and engineered barriers for radioactive waste confinement. September 17-18, 2007, Lille, France.

De Craen, M., Van Geet, M., Honty, M., Weetjens, E. & Sillen, X. (2008). Extent of oxidation in Rupel Clay as a result of excavation and ventilation of the HADES URF: experimental and modelling assessments. Physics and Chemistry of the Earth, 33, S350-S362.

Deniau, I., Derenne, S., Beaucaire, C., Pitsch, H. & Largeau, C. (2001). Morphological and chemical features of a kerogen from the underground Mol laboratory (Boom Clay Formation, Oligocene, Belgium): Structure, source organisms and formation pathways. Organic Geochemistry, 32, 1343–1356.

Deniau, I., Derenne, S., Beaucaire, C., Pitsch, H. & Largeau, C. (2004). Occurrence and nature of thermolabile compounds in the Boom Clay kerogen (Oligocene, underground Mol laboratory, Belgium). Organic Geochemistry, 35, 91–107.

Deniau, I., Behar, F., Largeau, C., De Canniere, P., Beaucaire, C. & Pitsch, H. (2005). Determination of kinetic parameters and simulation of early CO_2 production from the Boom Clay kerogen under low thermal stress. Applied Geochemistry, 20, 2097–2107.

Eberl, D.D., Velde, B. & McCormick, T. (1993). Synthesis of illite-smectite from smectite at earth surface temperatures and high pH. Clay Minerals, 28, 49-60.

Esnault, L, Libert, M. & Bildstein, O. (2013). Assessment of microbiological development in nuclear waste geological disposal: a geochemical modeling approach. Procedia Earth and Planetary Science, 7, 244-247.

Fritz, S. J. & Marine, I. W. (1983). Experimental support for a predictive osmotic model of clay membranes. Geochimica et Cosmochimica Acta, 47, 1515-1522.

Galán E. & Ferrell R.E. (2013). Genesis of Clay Minerals. In: Handbook of Clay Science Part A: Fundamentals – second edition. Edited by F. Bergaya and G. Lagaly. ISBN 978-0-08-098259-5, 83 – 126.

Garavito, A.M. (2007). Chemical osmosis in clayey sediments. Field experiments and numerical modelling. PhD thesis, Vrije Universiteit, Amsterdam, the Netherlands, 140 pp.

Garavito, A.M., De Cannière, P. & Kooi, H. (2007). In situ chemical osmosis experiment in the Boom Clay at the Mol underground research laboratory. Physics and Chemistry of the Earth, 32, 421-433.

Gaucher, E.C. & Blanc, P. (2006). Cement/clay interactions – a review: experiments, natural analogues, and modeling. Waste Management, 26, 776-788.

Gaucher, E.C., Blanc, P., Bardot, F., Braibant, G., Buschaert, S., Crouzet, C., Gautier, A., Girard, J-P., Jacquot, E., Lassin, A., Negrel, G., Tournassat, C., Vinsot, A. & Altmann, S. (2007). Modelling the porewater chemistry of the Callovian-Oxfordian formation at a regional scale. C.R. Geoscience, 338, 917-930.

Gautschi, A. & Mazurek, M. (2004) The geological evolution of Opalinus clay in the Zürcher Weinland area (NE Switzerland): learning from the past to predict future evolution and stability. In: Stability and Buffering Capacity of the Geosphere for Long-term Isolation of Radioactive Waste. Application to Argillaceous Media. OECD 2004 NEA No. 5303.

Gelhar, L.W., Welty, C. & Rehfeldt, K.R. (1992). A critical review of data on field-scale dispersion in aquifers. Water Resources Research, 28, 1955-1974.

Griffioen J., Klein J. & Van Gaans P.F.M. (2012). Reaction capacity characterization of shallow sedimentary deposits in geologically different regions of the Netherlands. Journal of Contaminant Hydrology, 127, 30-46.

Griffioen J. (2015). The composition of deep groundwater in the Netherlands in relation to disposal of radioactive waste. OPERA deliverable OPERA-PU-TNO521-2.

Griffioen, J., Verweij, H. & Stuurman, R.J. (2016). The composition of groundwater in Palaeogene and older formations in the Netherlands. A synthesis. Netherlands Journal of Geoscience, 95, 349-372.

GRS (Gesellschaft fur Anlagen und Reaktorsicherheid), 2012, Szenarienentwicklung: Methodik und Anwendung. Bericht zum Arbeitspaket B. Vorlaufige Sicherheitsanalyse fur den Standort Gorleben.

Grupa, J., Hart, J. & Wildenborg, T. (2017). Description of relevant scenarios for the OPERA disposal concept. OPERA deliverable OPERA-PU-NRG71111.

Helling, C.S., Chesters, G. & Corey, R.B. (1963). Contribution of organic matter and clay to soil cation-exchange capacity as affected by the pH of the saturating solution. Soil Sci. Soc. Am. J., 28, 517-520.

Hemes, S., Desbois, G, Urai, J. L., De Craen, M. & Honty, M. (2013). Variations in the morphology of porosity in the Rupel Clay Formation: insights from 2D high resolution BIB-SEM imaging and Mercury injection Porosimetry. Netherlands Journal of Geosciences, 92, 275-300.

Honty, M. (2010). CEC of the Boom Clay – a review. SCK-CEN report ER-134.

Huang, W-L., Bassett, W.A. & Wu, T-C. (1994). Dehydration and hydration of montmorillonite at elevated temperatures and pressures monitored using synchrotron radiation. American Mineralogist 79, 683 – 691.

Jacops, E., Maes, T., Maes, N., Volckaert, G., Weetjens, E. & Sillen, X. (2015). Gas-driven radionuclide transport in undisturbed and disturbed Boom Clay. In Gas generation and Migration in Deep Geological Radioactive Waste Repositories. Geological Society, London, Special Publications 415, 9-17.

Jacques, D. & Wang, L. (2012). Modelling the interaction of the alkaline plume with Rupel Clay at different scales. NEA/RWM/R(2012)3.

Janszen, A. (2012). Tunnel valleys: genetic models, sedimentary infill and 3D architecture. PhD thesis TUDelft.

Jowett, E.C., Cathles III, L.M. & Davis, B.W. (1993). Predicting depths of gypsum dehydration in evaporitic sedimentary basins. American Association of Petroleum Geologists Bulletin, 77(3), 402-413.

Keijzer, T.J.S., Kleingeld, P.J. & Loch, J.P.G. (1999). Chemical osmosis in compacted clayey material and the prediction of water transport. Engineering Geology, 53, 151-159.

Koenen, M. & Griffioen, J. (2014). Mineralogical and geochemical characterization of the Rupel Clay in the Netherlands. OPERA-deliverable: OPERA-PU-TNO521-1, 77 p.

Koenen, M.L. & Griffioen, J. (2016). Characterisation of the geochemical heterogeneity of the Boom Clay in the Netherlands. Netherlands Journal of Geoscience, 95, 269-282.

Kosakowski, G. & Berner, U. (2013). The evolution of clay rock/cement interfaces in a cementitious repository for low- and intermediate level radioactive waste. Physics and Chemistry of the Earth, 64, 65–86.

Kuhlmann, G., De Boer, P.L., Pedersen, R.B. & Wong, Th.E. (2004). Provenance of Pliocene sediments and paleoenvironmental changes in the southern North Sea region using Samarium-Neodymium (Sm/Nd) provenance ages and clay mineralogy. Sedimentary Geology, 171, 205–226.

Laird, D.A. (2006). Influence of layer charge on swelling of smectites. Applied Clay Science, 34, 74-87.

Lanson B., Beaufort D., Berger G., Bauer A., Cassagnabère A. & Meunier, A. (2002). Authigenic kaolin and illitic minerals during burial diagenesis of sandstones: a review. Clay Minerals, 37, 1-22.

Leijnse, A. (1992). Three-dimensional modelling of coupled flow and transport in porous media. PhD Thesis, University of Notre Dame, Notre Dame Indiana, United States.

Leroy P., Revil A., Altmann S. & Tournassat, C. (2007). Modeling the composition of the pore water in a clay-rock geological formation (Callovo-Oxfordian, France). Geochimica et Cosmochimica Acta, 71, 1087-1097.

Libert, M., Kerber Schutz, M., Esnault, L., Feron, D. & Bildstein, O. (2014). Impact of microbial activity on radioactive waste disposal: long term prediction of biocorrosion processes. Bioelectrochemistry, 97, 162-168.

MacDonald, G.J.G. (1953). Anhydrite-gypsum equilibrium relations. American Journal of Science, 251, 884-898.

Matschei, T., Lothenbach, B. & Glasser, F.P. (2007). Thermodynamic properties of Portland cement hydrates in the system CaO-Al2O3-SiO2-CaSO4-CaCO3-H2O. Cement and Concrete Research, 37,1379-1410.

Marty, N.C.M., Bildstein, O., Blanc, P., Claret, F., Cochepin, B., Gaucher, E.C., Jacques, D., Lartigue, J.-E., Li, S., Mayer, K.U., Meeussen, J.C.L., Munier, I., Pointeau, I., Su, D. & Steefel, C.I. (2015). Benchmarks for multicomponent reactive transport across a cement/clay interface. Computational Geosciences, 19(3), 635-653.

Mazurek, M., Alt-Epping, P., Bath, A., Gimmi, T., Niklaus Waber, H., Buschaert, S., Cannière, P.D., Craen, M.D., Gautschi, A., Savoye, S., Vinsot, A., Wemaere, I. & Wouters, L. (2011). Natural tracer profiles across argillaceous formations. Applied Geochemistry, 26, 1035-1064.

Meeussen, J.C.L. & Rosca-Bocancea, E. (2014) OPERA-PU-NRG1112B Determination of the inventory: part B matrix composition. http://www.covra.nl/downloads/opera/

Michels, R., Elie, M., Faure, P., Huault, V., Martinez, L., Bartier, D., Fleck, S. & Hautevelle, Y. (2003). Nature and reactivity of organic matter in Argillaceous formations: formations: example of the Callovo-Oxfordian of Bure (France). In: Stability and buffering capacity of the geosphere for long-term isolation of radioactive waste. OECD NEA No. 5303, p 165-168.

Molt, E.L. (1961). Verontreiniging van het Rijnwater. Water, 45, 143-148 en 160-164.

Norris, S. (2015). EC FORGE project: updated dconsideration of gas generation and migration in the safety case. In Gas Generation and Migration in Deep Geological Radioactive Waste Repositories. Geological Society, London, Special Publications 415, 241-258

Oldenburg, C.M., Moridis, G.J., Spycher, N. & Pruess, K. (2004). EOS7C Version 1.0: TOUGH2 Module for Carbon Dioxide or Nitrogen in Natural Gas (Methane) Reservoirs.

ONDRAF/NIRAS (2001). Technical overview of the SAFIR 2 report; Safety Assessment and Feasibility Interim Report 2. NIROND 2001-05 E.

ONDRAF/NIRAS (2009). NIROND-TR REPORT 2009-12 E, Geological Disposal Programme, www.nirond.be. Brussels, Belgium, 52 p.

Parkhurst, D. & Appelo, C.A.J. (2013). Description of input and examples for PHREEQC Version 3 – A computer program for speciation, batch-reaction, one-dimensional transport, and inverse geochemical calculations. U.S. Geological Survey Techniques and Methods, book 6, chap. A43, 497 p.

Pellegrini, R., Horseman, S., Kemp, S., Rochelle, C., Boisson, J.-Y., Lombardi, S., Bouchet, A. & Parneix, J.-C. (1999). Natural analogues of the thermo-hydro-chemical and thermo-hydro-mechanical response. Final report, EUR 19114 EN.

Perko, J., Mayer, K.U., Kosakowski, G., De Windt, L., Govaerts, J., Jacques, D., Su, D. & Meeussen, J.C.L. (2015). Decalcification of cracked cement structures. Computational Geosciences, 19(3), 673-693 2015.

Pruess, K., C. Oldenburg, G. Moridis (2012) TOUGH2 USER'S GUIDE, VERSION 2. LBNL-43134

Rousseau-Gueutin, P., Gonçalvès, J. & Violette, S. (2008). Osmotic efficiency in Callovo-Oxfordian argillites: Experimental vs. theoretical models. Physics and Chemistry of the Earth, 33, 106-113.

Sammartino, S., Bouchet, A., Parneix, J.C., Prêt D. & Meunier, A. (2004). Chemical buffering/mineralogical aspects: mineralogical stability. OECD - Nuclear Energy Agency, 75 - Paris (France); 241 p; ISBN 92-64-00908-6; p. 159-164; Application to argillaceous media, Clay Club, workshop; Braunschweig (Germany); 9-11 Dec 2003.

Seetharam, S. & Jacques, D. (2015) OPERA-PU-SCK514 Potential Degradation Processes of the Cementitious EBS Components, their Potential Implications on Safety Functions and Conceptual Models for Quantitative Assessment http://www.covra.nl/downloads/opera/

Smidsrød, O. & Painter, T.J. (1984). Contribution of carbohydrates to the cation-exchange selectivity of aquatic humus from peat-bog water. Carbohydrate Research, 127, 267-281.

Society for Sedimentary Geology (SEPM)(1988). Clay minerals for Petroleum Geologists and Engineers. Special Publications of SEPM, ISBN: 0-918985-73-0.

Spivey, J.P., McCain, W.D. & North, R. (2004). Estimation Density, Formation Volume Factor, Compressibility, Methane Solubility and Viscosity for Oilfield Brines at Temperatures From 0 to 275 °C, Pressures to 200 Mpa and salinities to 5.7 mole/kg. Journal of Canadian Petroleum Technology, 43(7), 52–61.

Srodon, J. (1999). Nature of mixed-layer clays and mechanisms of their formation and alteration. Annual Reviews in Earth and Planetary Science, 27, 19-53.

Srodon, J. (1999) Use of clay minerals in reconstructing geological processes: recent advances and some perspectives. Clay Minerals, 34, 27-37.

Steefel, C.I., Appelo, C.A.J., Arora, B., Jacques, D., Kalbacher, T., Kolditz, O., Lagneau, V., Lichtner, P.C., Mayer, K.U., Meeussen, J.C.L., Molins, S., Moulton, D., Shao, H., Simunek, J., Spycher, N., Yabusaki, S.B. & Yeh, G.T (2015). Reactive transport codes for subsurface environmental simulation. Computational Geosciences, 19(3), 445-478.

Sucha, V., Srodon, J., Clauer, N., Elsass, F, Eberl, D.D., Kraus, I. & Madejova, J. (2001). Weathering of smectite and illite-smectite under temperate climatic conditions. Clay Minerals, 36, 403-419.

Talbot, C.J. (1999). Ice ages and nuclear waste isolation. Engineering Geology, 52, 177-192.

Ten Veen, J., Govaerts, J., Beerten, K., Ventra, D. & Vis, G.-J. (2015). Future evolution of the geological and geohydrological properties of the geosphere. OPERA deliverable OPERA PU-TNO412.

Valstar J.R. & Goorden, N. (2016). Far-field transport modelling for a repository in the Rupel Clay in the Netherlands. Netherlands Journal of Geoscience, 95, 337-347.

Van Geet, M., Deniau, I., Largeau, C., Bruggeman, C., Maes, A. & Dierckx, A. (2003). Presence and evolution of Natural Organic Matter in the Rupel Clay. In Stability and buffering capacity of the geosphere for long-term isolation of radioactive waste. OECD NEA No. 5303.

Verhoef, E. & Schröder, T. (2011). Research Plan. OPERA-PG-COV004, 52 pp.

Verhoef, E.V., de Bruin, A.M.G., Wiegers, R.B., Neeft, E.A.C. & Deissmann, G. (2014). Cementitious materials in OPERA disposal concept in Boom Clay. OPERA-PG-COV020.

Verweij, J.M. & Nelskamp, S. (2015). Definition of the present boundary conditions for the near-field model_1. OPERQA deliverable OPERA-PU-TNO421.

Verweij, J.M., Vis, G.-J. & Imberechts, E. (2016). Spatial variation in porosity and permeability of the Rupel Clay Member in the Netherlands. Netherlands Journal of Geoscience, 95, 253-268.

Vinsot A., Leveau F., Bouchet A. & Arnould A. (2014). Oxidation front and oxygen transfer in the fractured zone surrounding the Meuse/Haute-Marne URL drifts in the Callovian-Oxfordian argillaceous rock. In: Clays in Natural and Engineered Barriers for Radioactive Waste Confinement. Geological Society, London, Special Publications 400, 207-220.

Vis G-J. & Verweij J.M. (2014). Geological and geohydrological characterization of the Rupel Clay and its overburden. OPERA deliverable OPERA-PU-TNO411.

Vis G.-J., Verweij, J.M. & Koenen, M. (2016). The Rupel Clay Member in the Netherlands: towards a comprehensive understanding of its geometry and depositional environment. Netherlands Journal of Geoscience, 95, 221-252.

Wang, L., Jacques, D. & De Canniere, P. (2010). Effects of an alkaline plume on the Rupel Clay as a potential host formation for geological disposal of radioactive waste. External report of the Belgian Nuclear Research Centre, SCK•CEN-ER-28, 09/LWa/P-42final.

Weibel, R. (1999). Effects of burial on the clay assemblages in the Triassic Skagerrak Formation, Denmark. Clay Minerals, 34, 619-635.

Wemaere , I., Marivoet, S. & Labat, S. (2008). Hydraulic conductivity variability of the Rupel Clay in north-east Belgium based on four core drilled boreholes. Physics and Chemistry of the Earth, 33, S24–S36.

Whitney, G. & Northrop, H.R. (1988). Experimental investigation of the smectite to illite reaction: Dual reaction mechanisms and oxygen-isotope systematics. American Mineralogist, 73, 77-90.

Wildenborg, A.F.B., Orlic, B., Thimus, J.F., De Lange, G., De Cock, S., De Leeuw, C.S. & Veling, E.J.M. (2003). Radionuclide transport in clay during climate change. Netherlands Journal of Geosciences, 82(1), 19-30.

Wildenborg, A.F.B., Orlic, B., De Lange, G., De Leeuw, C.S., Zijl, W., Van Weert, F., Veling, E.J.M., De Cock, S., Thimus, J.F., Lehnen-de Rooij, C. & Den Haan, E.J. (2000). Transport of Radionuclides disposed of in Clay of Tertiary Origin (TRACTOR). TNO report NITG 00-223-B, 223 p.

Wouters, K., Moors, H., Boven, P. & Leys, N. (2013). Evidence and characteristics of a diverse and metabolically active microbial community in deep subsurface clay borehole water. FEMS Microbial Ecology, 86(3), 458–473.

Yang, C., Samper, J., Molinero, J., & Bonilla, M. (2007). Modelling geochemical and microbial consumption of dissolved oxygen after backfilling a high level radioactive waste repository. Journal of Contaminant Hydrology, 93, 130-148.

Zeelmaekers, E. (2011). Computerized qualitative and quantitative clay mineralogy. Introduction and application to known geological cases. Ph.D. thesis, Katholieke Universiteit (Leuven), 397 pp.

Zhou, Z. J., Cameron, S., Kadatz, B. & Gunter, W. D. (1997). Clay Swelling Diagrams: Their Applications in Formation Damage Control. Society of Petroleum Engineers Journal (2), 99-106.

Appendix 1. Chemical reactions taken into account in the EBS/clay interaction model

Name	Reaction	log K
AlOH+2	1.0 Al+3 + -1.0 H+ + 1.0 H2O	-4.99
AlSO4+	1.0 Al+3 + 1.0 SO4-2	3.02
Al[OH]2+	1.0 Al+3 + -2.0 H+ + 2.0 H2O	-10.1
Al[OH]3	1.0 Al+3 + -3.0 H+ + 3.0 H2O	-16
Al[OH]4-	1.0 Al+3 + -4.0 H+ + 4.0 H2O	-23
Al[SO4]2-	1.0 Al+3 + 2.0 SO4-2	4.92
CO3-2	1.0 CO2[g] + -2.0 H+ + 1.0 H2O	-18.16
CaCO3	1.0 CO2[g] + 1.0 Ca+2 + -2.0 H+ + 1.0 H2O	-15.01
CaHCO3+	1.0 CO2[g] + 1.0 Ca+2 + -1.0 H+ + 1.0 H2O	-6.83
CaOH+	1.0 Ca+2 + -1.0 H+ + 1.0 H2O	-12.598
CaSO4	1.0 Ca+2 + 1.0 SO4-2	2.309
Fe+2	1.0 Fe+3 + -1.0 H+ + 5.000000000000e-1 H2O + -2.500000000000e-1 O2[g]	-7.748
Fe2[OH]2+4	2.0 Fe+3 + -2.0 H+ + 2.0 H2O	-2.95
Fe3[OH]4+5	3.0 Fe+3 + -4.0 H+ + 4.0 H2O	-6.3
FeCl+2	1.0 Cl- + 1.0 Fe+3	1.48
FeCl2+	2.0 Cl- + 1.0 Fe+3	2.13
FeCl3	3.0 Cl- + 1.0 Fe+3	1.13
FeOH+	1.0 Fe+3 + -2.0 H+ + 1.5 H2O + -2.500000000000e-1 O2[g]	-17.248
FeOH+2	1.0 Fe+3 + -1.0 H+ + 1.0 H2O	-2.19
FeSO4	1.0 Fe+3 + -1.0 H+ + 5.000000000000e-1 H2O + -2.500000000000e-1 O2[g] + 1.0 SO4-2	-5.498
FeSO4+	1.0 Fe+3 + 1.0 SO4-2	3.92
Fe[HS]2	1.0 Fe+3 + 1.0 H+ + 5.000000000000e-1 H2O + -4.25 O2[g] + 2.0 SO4-2	-263.958
Fe[HS]3-	1.0 Fe+3 + 2.0 H+ + 5.000000000000e-1 H2O + -6.25 O2[g] + 3.0 SO4-2	-394.501
Fe[OH]2	1.0 Fe+3 + -3.0 H+ + 2.5 H2O + -2.500000000000e-1 O2[g]	-28.318
Fe[OH]2+	1.0 Fe+3 + -2.0 H+ + 2.0 H2O	-5.67
Fe[OH]3	1.0 Fe+3 + -3.0 H+ + 3.0 H2O	-13.6
Fe[OH]3-	1.0 Fe+3 + -4.0 H+ + 3.5 H2O + -2.500000000000e-1 O2[g]	-38.748
Fe[OH]4-	1.0 Fe+3 + -4.0 H+ + 4.0 H2O	-21.6
Fe[SO4]2-	1.0 Fe+3 + 2.0 SO4-2	5.42
H2	1.0 H2O + -5.000000000000e-1 O2[g]	-44.71
H2CO3	1.0 CO2[g] + 1.0 H2O	-1.479
H2S	2.0 H+ + -2.0 O2[g] + 1.0 SO4-2	-125.586
H2SiO4-2	-2.0 H+ + 1.0 H4SiO4	-21.619
H3SiO4-	-1.0 H+ + 1.0 H4SiO4	-9.93
HCO3-	1.0 CO2[g] + -1.0 H+ + 1.0 H2O	-7.83
HS-	1.0 H+ + -2.0 O2[g] + 1.0 SO4-2	-132.58
HSO4-	1.0 H+ + 1.0 SO4-2	1.987
KSO4-	1.0 K+ + 1.0 SO4-2	0.85
MgCO3	1.0 CO2[g] + -2.0 H+ + 1.0 H2O + 1.0 Mg+2	-15.18
MgHCO3+	1.0 CO2[g] + -1.0 H+ + 1.0 H2O + 1.0 Mg+2	-6.76
MgOH+	-1.0 H+ + 1.0 H2O + 1.0 Mg+2	-11.79

MgSO4	1.0 Mg+2 + 1.0 SO4-2	2.25
NO2-	1.0 NO3- + -5.000000000000e-1 O2[g]	-12.9747
NaCO3-	1.0 CO2[g] + -2.0 H+ + 1.0 H2O + 1.0 Na+	-16.892
NaHCO3	1.0 CO2[g] + -1.0 H+ + 1.0 H2O + 1.0 Na+	-8.08
NaSO4-	1.0 Na+ + 1.0 SO4-2	0.7
O2	1.0 O2[g]	-2.96
OH-	-1.0 H+ + 1.0 H2O	-13.998
S-2	-2.0 O2[g] + 1.0 SO4-2	-145.498
e-	-1.0 H+ + 5.000000000000e-1 H2O + -2.500000000000e-1 O2[g]	-20.78
Cem07_AA_Fe[OH]3[am]	1.0 Fe+3 + -3.0 H+ + 3.0 H2O	-5
Cem07_Al[OH]3[am]	1.0 Al+3 + -3.0 H+ + 3.0 H2O	-9.2413
Cem07_Anhydrite	1.0 Ca+2 + 1.0 SO4-2	4.3596
Cem07_Brucite	-2.0 H+ + 2.0 H2O + 1.0 Mg+2	-16.8291
Cem07_C2AH8	2.0 Al+3 + 2.0 Ca+2 + -10.0 H+ + 13.0 H2O	-60.4283
Cem07_C2ASH8	2.0 Al+3 + 2.0 Ca+2 + -10.0 H+ + 11.0 H2O + 1.0 H4SiO4	-50.2143
Cem07_C2FH8	2.0 Ca+2 + 2.0 Fe+3 + -10.0 H+ + 13.0 H2O	-53.5858
Cem07_C3AH6	2.0 Al+3 + 3.0 Ca+2 + -12.0 H+ + 12.0 H2O	-81.1412
Cem07_C3FH6	3.0 Ca+2 + 2.0 Fe+3 + -12.0 H+ + 12.0 H2O	-74.0217
Cem07_C4AH13	2.0 Al+3 + 4.0 Ca+2 + -14.0 H+ + 20.0 H2O	-104.572
Cem07_C4FH13	4.0 Ca+2 + 2.0 Fe+3 + -14.0 H+ + 20.0 H2O	-97.7718
Cem07_CAH10	2.0 Al+3 + 1.0 Ca+2 + -8.0 H+ + 14.0 H2O	-38.4955
Cem07_Calcite	1.0 CO2[g] + 1.0 Ca+2 + -2.0 H+ + 1.0 H2O	-9.6745
Cem07_Gypsum	1.0 Ca+2 + 2.0 H2O + 1.0 SO4-2	4.583
Cem07_Portlandite	1.0 Ca+2 + -2.0 H+ + 2.0 H2O	-22.7934
Cem07_Syngenite	1.0 Ca+2 + 1.0 H2O + 2.0 K+ + 2.0 SO4-2	-7.2
Pyrite	1.0 Fe+3 + 1.0 H+ + -5.000000000000e-1 H2O + -3.75 O2[g] + 2.0 SO4-2	-212.869
Siderite	1.0 CO2[g] + 1.0 Fe+3 + -3.0 H+ + 1.5 H2O + -2.500000000000e-1 O2[g]	-15.358
Cem07_C4AsH12_ss	1.0 AFm_ss + 2.0 Al+3 + 4.0 Ca+2 + -12.0 H+ + 18.0 H2O + 1.0 SO4-2	-72.7162
Cem07_C4FsH12_ss	1.0 AFm_ss + 4.0 Ca+2 + 2.0 Fe+3 + -12.0 H+ + 18.0 H2O + 1.0 SO4-2	-65.9736
Cem07_C6As3H32_ss	1.0 AFt_ss + 2.0 Al+3 + 6.0 Ca+2 + -12.0 H+ + 38.0 H2O + 3.0 SO4-2	-57.066
Cem07_C6Fs3H32_ss	1.0 AFt_ss + 6.0 Ca+2 + 2.0 Fe+3 + -12.0 H+ + 38.0 H2O + 3.0 SO4-2	-55.1666
Cem07_Jenn_ss	1.0 CSHii_ss + 1.6666667 Ca+2 + -3.3333333 H+ + 1.7666666 H2O + 1.0 H4SiO4	-29.4185
Cem07_SiO2[am]_ss	1.0 CSHi_ss + -2.0 H2O + 1.0 H4SiO4	2.5907
Cem07_Tob_II_ss	1.0 CSHii_ss + 8.333333000000e-1 Ca+2 + -1.6666667 H+ + 1.666667000000e-1 H2O + 1.0 H4SiO4	-11.2573
Ettringite_ss	2.0 Al+3 + 6.0 Ca+2 + -12.0 H+ + 3.0 SO4-2 + 1.0 ettr_ss	-56.992

Appendix 2. Literature review on chemical osmosis

Semi-permeability

Clay acts as a semi-permeable membrane because the clay platelets are negatively charged. Anions will be repelled by the platelets because they have the same charge. This is explained by the double-layer theory. The repulsive force between a dissolved anion and the clay mineral surface decreases as the distance between them increases (Figure 1a).

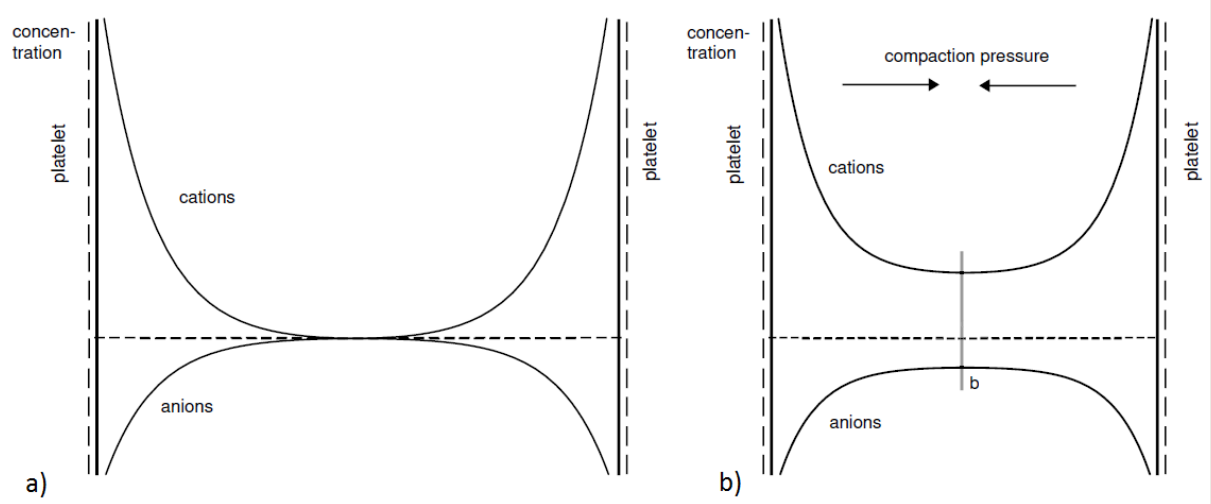

Figure 1 - a) Diffuse double layer. The clay platelets are located far enough from each other in order for solutes to pass through. **b)** The clay platelets are too close together, the diffuse double layers overlap and anions are repelled and cannot move through the pore between the platelets (Bader, 2005).

However, the double layers can overlap in small pores (Figure 1b). When this occurs, anions are repelled in the whole pore and are thus not able to move through the clay. In bulk concentrations, however, the double layers degenerate and anions are able to pass through the clay. Thus, the semi-permeability of the clay is a function of both the porosity and concentration.

In mathematical models, the semi-permeability of the clay membrane is described by the reflection coefficient σ. The value of the reflection coefficient lies between 0 and 1. A fully permeable membrane (all solute passes through the membrane) has a reflection coefficient of 0 and a fully semi-permeable membrane (no solute passes through) has a reflection coefficient of 1.

The osmotic efficiency should be higher for a low porosity and moderate salt concentrations. Several expressions for the reflection coefficient are given in the literature. Most expressions depend on pore-scale properties of the clay layer. Several expressions are suggested in the literature, which depend on microscale properties of the clay (e.g. Fritz and Marine (1983), Bresler (1973)). A simpler expression for the reflection coefficient is given by Bader (2005), which gives a linear relation between the reflection coefficient and solute concentration.

In this study, however, a constant reflection coefficient is assumed. Concentration-dependent reflection coefficients have been investigated, but this would lead to numerically unstable model, because these expressions make the model highly non-linear.

In order to capture the effects of chemical osmosis on the flow of groundwater, Darcy's law is extended with an extra term. The extended Darcy's Law is given by:

$$\bar{q} = -\frac{\kappa}{\mu}(grad\, P - \sigma\, \mathrm{grad}\, \pi) \qquad \text{Eq. 1}$$

where σ is the reflection coefficient, π is the osmotic pressure, κ is the intrinsic permeability of the porous medium, μ is the dynamic viscosity of the fluid, P is the fluid pressure and q is the Darcy velocity.

The gradient of the osmotic pressure is defined as:

$$grad\, \pi = \nu RT\, grad\, C = \nu RT \rho\, grad\, \omega \qquad \text{Eq. 2}$$

Here, v is the dissociation coefficient of the solute, which equals the amount of ions a solute dissociates into, R is the ideal gas constant, T is the absolute temperature and C is the solute concentration, ρ is the fluid density and ω is the solute mass fraction.

The extended Darcy's Law can then be written as:

$$\bar{q} = -\frac{\kappa}{\mu}(grad\, P - \sigma \nu RT \rho\, grad\, \omega) \qquad \text{Eq. 3}$$

Fluid mass balance

The continuity equation for the fluid is given by:

$$\frac{\partial}{\partial t}(n\rho) + div(\rho \bar{q}) = 0 \qquad \text{Eq. 4}$$

The fluid density is assumed to depend only on the fluid pressure. The effect of temperature and salinity are assumed to be negligible in this study. The equation of state for the fluid density is then given by:

$$\rho = \rho_0 e^{\beta(P-P_0)} \qquad \text{Eq. 5}$$

Here, ß is the fluid compressibility, *P* is the fluid pressure and ρ_0 and P_0 are reference values for density and pressure, respectively.

The porosity is also assumed to be a function of fluid pressure. The following relation between porosity and pressure is used (Leijnse, 1992):

$$n = 1 - (1 - n_0)e^{-\alpha P} \quad \text{Eq. 6}$$

Using these expressions for the porosity and fluid density, the first term of the fluid mass balance can be rewritten:

$$\frac{\partial}{\partial t}(n\rho) = \rho(n\beta + (1-n)\alpha)\frac{\partial P}{\partial t} = \rho S\frac{\partial P}{\partial t} \quad \text{Eq. 7}$$

Here, the term $n\beta + (1-n)\alpha$ is defined as a storage parameter *S* and is assumed to be constant. Under this assumption, the fluid mass balance can be reduced to:

$$S\frac{\partial P}{\partial t} + div\,\bar{q} + \beta\bar{q}\,grad\,P = 0 \quad \text{Eq. 8}$$

Salt mass balance

The salt mass balance is given by:

$$\frac{\partial}{\partial t}(n\rho\omega) + div\,J \quad \text{Eq. 9}$$

where *J* is the salt mass flux, for which the following expression is used:

$$J = \rho\omega\bar{q} - \sigma\rho\omega\bar{q} - D\rho\,grad\,\omega \quad \text{Eq. 10}$$

The first term represents transport due to advection, the second term ultrafiltration and the third term represents molecular diffusion. Using this expression for the salt mass flux in Equation 9, the following salt mass balance is obtained:

$$\frac{\partial}{\partial t}(n\rho\omega) + div\,(\rho\omega\bar{q}) + div\,(-\sigma\rho\omega\bar{q} - D\rho\,grad\,\omega) \quad \text{Eq. 11}$$

which can be simplified to:

$$\frac{\partial}{\partial t}(n\rho\omega) + div\,(1-\sigma)\rho\omega\bar{q} - div(D\rho\,\mathrm{grad}\,\omega) \quad \text{Eq. 12}$$

For a fully impermeable membrane, σ equals 1 and the advection term will disappear from the equation. No solute should be able to pass through an ideal membrane. Therefore, the diffusive flux term must also disappear from the equation when σ equals 1. However, the diffusion coefficient should approach its normal value when the membrane shows no semi-permeable characteristics. A simple expression for the diffusion coefficient which holds for both requirements is given in Bader and Kooi (2005):

$$D^* = (1-\sigma)D_{eff} \qquad \text{Eq. 13}$$

Where *D* is the diffusion coefficient corrected for porosity and semi-permeability. Here, D_{eff} is the effective diffusion coefficient, which is already corrected for porosity and tortuosity. From here on, *D** is simply written as *D* for convenience.

Using the expressions for porosity and fluid density from Equations 5 and 6, the salt mass balance can be written as:

$$n\frac{\partial \omega}{\partial t} + S\omega\frac{\partial P}{\partial t} + (1-\sigma) * \mathrm{div}\,(\rho\bar{q}) + (1-\sigma) * \beta\omega\bar{q} * grad\,P - div(D\,grad\,\omega) - D\beta\,grad\,\omega\,grad = 0 \qquad \text{Eq. 14}$$

Changes in porosity due to variations in the fluid pressure are assumed to be small, and therefore *n* is approximated by n_0.

Dimensionless equations

The derivation of dimensionless equations is the same as in Bader (2005). Readers are referred there for a full derivation of the dimensionless equations. For simplicity, we will consider a one-dimensional problem.

The following dimensionless variables are introduced:

$$P^* = \frac{P-P_{min}}{P_{max}-P_{min}} \qquad x' = \frac{x}{L} \qquad q' = q\frac{L\mu}{\kappa(P_{max}-P_{min})} \qquad t' = t\frac{\kappa}{\mu S L^2} \qquad c' = \frac{c-c_{min}}{c_{max}-c_{min}}$$

Instead of using the mass fraction for the concentration, the molar concentration is used for convenience. Using the aforementioned expressions for the dimensionless variables, the dimensionless fluid mass balance can then be written as:

$$\frac{\partial P'}{\partial t'} + \frac{\partial q'}{\partial x'} + \beta(P_{max}-P_{min})q'\frac{\partial P'}{\partial x'} = 0 \qquad \text{Eq. 15}$$

The dimensionless Darcy’s Law:

$$q' = -\frac{\partial P'}{\partial x'} + \frac{\partial c'}{\partial x'} \qquad \text{Eq. 16}$$

The dimensionless salt mass balance becomes:

$$n\frac{\partial c'}{\partial t'} + S(P_{max}-P_{min})c'\frac{\partial P}{\partial t} + (1-\sigma)S(P_{max}-P_{min})\frac{\partial c'q'}{\partial x'} - \frac{SD\mu}{\kappa}\frac{\partial^2 c'}{\partial x'^2} = 0 \qquad \text{Eq. 17}$$

The third term, which describes advection, can be neglected when $(1-\sigma)S(P_{max}-P_{min}) \ll \frac{SD\mu}{\kappa}$. In this case, diffusion is the dominant transport process.

Thus, we define the following dimensionless number:

$$Pe = \frac{(1-\sigma)\kappa(P_{max} - P_{min})}{\mu D} \qquad \text{Eq. 18}$$

This is the osmotic Peclet number. When the osmotic Peclet number is smaller than 1, advection is the dominant transport process. Otherwise, diffusion is dominant. Normally, transport in clay layers is dominated by diffusion. This number can be used to determine if this is also the case for chemical osmosis.

OPERA
Meer informatie:

Postadres
Postbus 202
4380 AE Vlissingen

T 0113-616 666
F 0113-616 650
E info@covra.nl

www.covra.nl